VYSOKÉ UČENÍ TECHNICKÉ V BRNĚ

Fakulta stavební

DIZERTAČNÍ PRÁCE

Brno, 2018 Ing. Jana Kaděrová

BRNO UNIVERSITY OF TECHNOLOGY
VYSOKÉ UČENÍ TECHNICKÉ V BRNĚ

FACULTY OF CIVIL ENGINEERING
FAKULTA STAVEBNÍ

INSTITUTE OF STRUCTURAL MECHANICS
ÚSTAV STAVEBNÍ MECHANIKY

PROBABILISTIC DISCRETE MODEL OF CONCRETE FRACTURING
PRAVDĚPODOBNOSTNÍ DISKRÉTNÍ MODEL PORUŠOVÁNÍ BETONU

DOCTORAL THESIS
DIZERTAČNÍ PRÁCE

AUTHOR Ing. JANA KADĚROVÁ
AUTOR PRÁCE

SUPERVISOR doc. Ing. JAN ELIÁŠ, Ph.D.
VEDOUCÍ PRÁCE

BRNO 2018

ABSTRACT

The thesis presents results of a numerical study on the performance of 3D discrete meso-scale lattice-particle model of concrete. The existing model was extended by introducing the spatial variability of chosen material parameter in form of random field. An experimental data from bending tests on notched and unnotched beams was exploited for the identification of model parameters as well as for the subsequent validation of its performance. With the basic and the extended randomized version of the model, numerical simulations were calculated so that the influence of the rate of fluctuation of the random field (governed by the correlation length) could be observed. The final part of the thesis describes the region in the beam active during the test in which the most of the fracture energy is released in terms of its size and shape. This region defines the strength of the whole member and as shown in the thesis, it does not have a constant size but it is influenced by the geometrical setup and the correlation length of the random field.

KEYWORDS

Concrete, discrete model, meso-scale, lattice-particle model, probability, random field, experiments, crack, active zone, fracture energy

ABSTRAKT

Dizertační práce představuje výsledky numerické studie provedené s pomocí 3D diskrétního mezo-úrovňového mřížkově-částicového (lattice-particle) modelu betonu. Již existující model byl rozšířen o prostorovou variabilitu některých materiálových parametrů pomocí náhodného pole. Laboratorní experimenty z literatury posloužily jednak k identifikaci parametrů, zároveň také umožnily ověřit správné chování modelu s určenými parametry. Se základním i rozšířeným modelem byla provedena série numerických simulací zaměřená na popis vlivu míry proměnlivosti náhodného pole definované korelační délkou na celkovou únosnost prvku. Závěr práce je věnován popisu oblasti, ve které je během zatěžování uvolněna většina lomové energie, a to z hlediska její velikosti i tvaru. Tato zóna rozhoduje o celkové pevnosti prvku a jak je ukázáno, její tvar i velikost nejsou konstantní, ale závisí na typu zatěžování (přítomnost zářezu) a také na korelační délce náhodného pole.

KLÍČOVÁ SLOVA

Beton, diskrétní model, mezo-úroveň, mřížkově-částicový model, pravděpodobnost, náhodné pole, experiment, trhlina, aktivní zóna, lomová energie

KADĚROVÁ, Jana. *Probabilistic Discrete Model of Concrete Fracturing*. Brno, 2018, 98 p. Doctoral thesis. Brno University of Technology, Faculty of Civil Engineering, Institute of Structural Mechanics. Advised by doc. Ing. Jan Eliáš, Ph.D.

Declaration

I declare that I have written the Doctoral Thesis titled "Probabilistic Discrete Model of Concrete Fracturing" independently, under the guidance of the advisor and using exclusively the technical references and other sources of information cited in the thesis and listed in the comprehensive bibliography at the end of the thesis.

As the author I furthermore declare that, with respect to the creation of this Doctoral Thesis, I have not infringed any copyright or violated anyone's personal and/or ownership rights. In this context, I am fully aware of the consequences of breaking Regulation § 11 of the Copyright Act No. 121/2000 Coll. of the Czech Republic, as amended, and of any breach of rights related to intellectual property or introduced within amendments to relevant Acts such as the Intellectual Property Act or the Criminal Code, Act No. 40/2009 Coll., Section 2, Head VI, Part 4.

Brno ....

author's signature

Acknowledgement

Ráda bych poděkovala svému školiteli doc. Ing. Janu Eliášovi, Ph.D. za jeho pedagogické i vědecké vedení, odborné rady, čas strávený konzultacemi a zejména trpělivost a lidský přístup prokázaný v mnoha situacích. Děkuji prof. Ing. M. Vořechovskému, Ph.D. za inspiraci a cenné zkušenosti. Za neutuchající podporu a zájem jsem vděčná své rodině a svým blízkým přátelům.

Dílčí výsledky práce vznikly za podpory projektu 15-19865Y: „Discrete fracture models: adaptive remeshing, energy release rate, and stress along boundaries“.

Děkuji nadaci „Nadání Josefa, Marie a Zdeňky Hlávkových“, která finančně podpořila prezentaci výsledků mého výzkumu na mezinárodní konferenci ICNAAM (Řecko, 2013).

CONTENTS

1 Introduction and Objectives **17**

2 State-of-the-Art **21**

3 Discrete model **25**

3.1 Lattice-particle model 25

3.2 Probabilistic discrete model 31

3.3 Summary 34

4 Identification of the Model Parameters **35**

4.1 Experimental data 35

4.2 Parameters identification 40

4.2.1 Parameters of deterministic model 40

4.2.2 Parameters of probabilistic extension 41

4.3 Model validation 42

4.3.1 Deterministic simulations of the experiment 43

4.3.2 Probabilistic simulations of the experiment 45

4.4 Summary and size effect 45

5 Influence of the Correlation Length **49**

5.1 Determining the correlation length on experimental data 49

5.2 Relationship between the tensile strength and fracture energy 51

5.3 New series of simulations 54

5.3.1 New geometry 54

5.3.2 The correlation length study 55

5.4 Summary 61

6 Spatial Distribution of Energy Dissipation **63**

6.1 Data Processing 63

6.1.1 Mesh Grid Procedure 64

6.1.2 Approximation of Active Zone by Geometrical Shapes 67

6.1.3 Novelty Detection Tool 68

6.2 Evaluation of the Active Zone 70

6.2.1 Mesh Grid Evaluation 70

6.2.2 Evaluation of the Geometrical Shapes Approximation 75

6.2.3 Novelty Detection Evaluation 78

6.3 Summary 80

7 Conclusion **83**

Bibliography **86**

List of symbols, physical constants and abbreviations **95**

LIST OF FIGURES

1.1 Simulation of the bending experiment with the discrete model: final stage with developed macrocrack. Red color marks the contacts with high value of damage parameter. 20

3.1 a) Random placement of the grains – simulated meso-structure. b) Rigid cells created by tessellation. c) Contact between adjacent cells. Figure adopted from [21]. 25

3.2 a) Contact area (potential crack surface) between two adjacent particles; b) projected contact area; c) geometry and degrees of freedom of a connection strut; d) stress acting on the contact area. Figure adopted from [14]. 28

3.3 Constitutive law according to [14]: the elastic envelope (right) and the exponential softening (left). Figure adopted from [21]. 29

3.4 Weibull-Gauss grafted probability distribution. Figure adopted from [21]. 31

3.5 One realization of a random field generated on a regular grid (left) and projected to the model elements (right). Figure adopted from [21]. 34

4.1 Schematic overview of beam geometries tested in [27]. 35

4.2 Sand, aggregates and mix gradings. Figure adopted from [27]. 36

4.3 Scheme of the concrete beam models: notched (left) and unnotched (right) beam. 38

4.4 Maximum, average and minimum response of each specimen group, data taken from [27]. The values in top right corners correspond to the mean peak load and the area under the mean curve. 39

4.5 Estimation of the correlation length: ten probabilistic simulations of Ac beam. 43

4.6 Ten deterministic simulations (red) and the experimental data [27] (green). Errorbars show the average peak load (value in top right corner) and the standard deviation. 44

4.7 Size effect diagrams: nominal strength vs. beam size. Experiments (green), deterministic (red) and probabilistic (blue) simulations. . . . 46

4.8 Twenty four probabilistic simulations (blue) and the experimental data [27] (green). Errorbars show the average peak load (value in top right corner) and the standard deviation for experiments, deterministic and probabilistic model. 47

4.9 Examples of two probabilistic simulations. Left: deeply-notched beam Aa. Right: unnotched beam Ac. First row: realization of the random field H used in the simulation; second row: damage parameter at the peak load; third row: damage parameter at the end of the simulation. 48
5.1 Experimental (green), deterministic (red) and probabilistic (blue) peak load [kN] vs. correlation length [m] of the random field from simulations of all sizes of unnotched beams (groups Ac, Bc, Cc, Dc). . 50
5.2 Experimental (green), deterministic (red) and probabilistic (blue) peak load [kN] vs. correlation length [m] of the random field from simulations of the second largest size of deeply-notched beams (group Ba). 51
5.3 Comparison of two alternatives for scaling of fracture energy G_{t}. Left: stress-strain relation of contact strained purely in normal direction when considering linear (alternative I) or quadratic (alternative II) dependency of G_{t} on random parameter h. Right: peak loads calculated with the probabilistic models of $l_{\mathrm{c}} = \infty$ using five different grain arrangements. 53
5.4 Scheme of the new geometry: three types of beams: deeply-notched (top), shallowly-notched (middle) and unnotched (bottom). Thickness of all beam types was 40 mm. 54
5.5 Dependency of the maximum load on the correlation length l_{c} of the random field for unnotched beams (type c). 55
5.6 Dependency of the maximum load on the correlation length l_{c} of the random field for deeply-notched beams (type a). 56
5.7 Dependency of the maximum load on the correlation length l_{c} of the random field for fifth-notched beams (type b). 57
5.8 Notched beams. Left: Schematic representation of spatial variability of $H(\boldsymbol{x})$. Middle: load – gauge opening curves for selected values of l_{c}. Right: Damage pattern at the peak load and at the end of one simulation. 60
5.9 Unnotched beams. Left: Schematic representation of spatial variability of $H(\boldsymbol{x})$. Middle: load – gauge opening curves for selected values of l_{c}. Right: Damage pattern at the peak load and at the end of one simulation. 62
6.1 Energy released in the solution step when the peak load is reached. . 65
6.2 Maximum of the dissipated relative energy on a mesh grid bin over the set of simulations. 66
6.3 Different geometrical shapes used for the approximation: scheme for unnotched beams. 67

6.4 Different geometrical shapes used for the approximation: scheme for notched beams. 67
6.5 Examples of scaling of the selected geometrical shapes. 67
6.6 Mesh grid evaluation of the active zone: contour plot of $\bar{R}_b$ (normalized relative dissipated energy) in bins for three different models. . . . 71
6.7 Mesh grid evaluation of the active zone: Three selected contours and their dependence on width, depth, area and shape on the correlation length. 72
6.8 An evolution of the active zone for notched and unnotched beams during the loading (results from 100 simulations, $l_c = \infty$). 74
6.9 Portion of relative the energy included in a rectangle region (shape a) vs. its area (unnotched beams). 75
6.10 Portion of the relative energy included in different geometrical shapes vs. their area (unnotched beams). 76
6.11 Portion of included relative energy in different geometrical shapes vs. their area (notched beams). 77
6.12 Notched beams: Relative energy dissipated at individual contacts and border contours specifying the amount of the dissipated energy (outlier and novelty detection tool). 78
6.13 Unnotched beams: Relative energy dissipated at individual contacts and border contours specifying the amount of the dissipated energy (outlier and novelty detection tool). 79

LIST OF TABLES

4.1 Concrete mixture composition [27]. 36
4.2 Number of specimens tested in [27]. 37
4.3 Results of three-point bending experiments from [27]: statistics of the maximum loading force $F_{\max}$. 37
4.4 Parameters of the numerical model by Cusatis [14], simplified as in [21]. 41
4.5 Parameters of the probability distribution (Eq. 3.18). 42
5.1 Results of a hundred of deterministic and probabilistic simulations for $l_c = \infty$ (mean, standard deviation and coefficient of variation) plus predicted CoV. 58
5.2 Results of a hundred of probabilistic simulations for $l_c = 0$ and 0.025 m (mean, standard deviation and coefficient of variation). 58
5.3 Ratio between the probabilistic and the deterministic peak load for each correlation length l_c. 59
6.1 Different geometrical shapes used for the approximation. 68

1 INTRODUCTION AND OBJECTIVES

Motivation

The general focus of researchers in civil engineering is to understand, model and predict behavior of civil engineering structures. Such ability requires to have strong foundations in understanding the behavior of materials used to build these structures. One of the most common material in civil engineering practice is concrete and similar silicate composites.

A significant aspect of the behavior of concrete structures is their nonlinear response to loading which is, moreover, random due to its heterogeneous nature. An accurate model of concrete that would be able to capture the generation and development of microcracks and their subsequent interconnection into macrocracks has therefore to take into the consideration the natural disorder of the inner structure and associated inherent (natural) variability of the local material parameters that lead into the random response of the structural members. The numerical model has to be able also to describe the post-critical behavior of the material with the development of the zones of intensive energy release. Such zones are referred to as the fracture process zones and it is generally agreed that the phenomena defining the member overall strength take place. Therefore, precise description and understanding of these zones are essential for the modern civil engineering.

Numerical modeling combined with laboratory testing is the most common and most efficient way of detailed investigating of the behavior of materials and members in engineering today. Correct numerical model can provide a strong tool for intensive virtual testing with wide range of possible test setups (sometimes hardly feasible in laboratory) while physical experiments ensure the model validity and correctness. Both methods need to be combined together so that their correctness and applicability can be proven.

The discrete modeling of materials provides several advantages compared to the classical continuum models. They offer a convenient tool for modeling the members made of composites due to their ability to describe the heterogeneous inner structure. At the same time, by implementation of relatively simple formulation of the constitutive relation, they can simulate the phenomenon such as softening of the material in the direction orthogonal to the cracks, etc. Such capability is, on the other hand, the reason for higher computational demand of such models. Despite this fact, discrete material modeling became a well-known method in the modern engineering.

Introduction

The dissertation thesis deals with the behavior of concrete as a representant of heterogeneous material with a quasi-brittle response to the mechanical loading. It investigates possibilities of application of a modern computational model of concrete which is capable of capturing the mechanical behavior on the scale of its grains (meso-scale modeling). The model chosen for such study is the *lattice-particle* model which had been developed by G. Cusatis and collaborators [12, 13, 14] under the name LDPM (lattice discrete particle model). It describes the material as an assembly of discrete units. This well-known model has been extended by incorrporation of the spatial variability of selected model parameters [21]. The parameters that have been considered as random are the local tensile strength of the contact between two aggregates and the fracture energy of this bond. These parameters have been defined by means of the mutually correlated random fields. Such an additional source of disorder of the response could help the model to correspond better to the experimental results. The enhanced model could also be able to address the natural localization of damage that appears in the structural models without any strong stress concentrators.

The thesis aims to deliver the robust numerical model combining the probabilistic models with the advanced mechanical model of concrete on its meso-level scale. Such model is employed in an intensive virtual testing of the concrete members with different input conditions. Correct behavior of such numerical model is guaranteed by the validation based on comparison with the real measurement. For that reason, the results of the computational model are compared to some published experiments.

Objectives

The main objectives of the thesis are:

- Application of the discrete model enhanced by the spatial variability considered in form of random field
- Identification of the model parameters based on the experimental data from wide series of bent concrete specimens of different sizes and notch depths
- Model validation based on the experimental data
- Study on performance of the basic and enhanced numerical models; evaluation of the response variability and the study on the influence of the autocorrelation length of the random field on the overall member response
- Description and evaluation of the nonlinear zone active during the model loading with the main focus on size and shape of such zone at the peak load

Content of the thesis

The presented thesis is divided into several chapters according to gradual development of the study.

Chapter 2 opens the thesis with the description of the current state of the art on a field of the modeling of materials by the discrete models. Different continuum approaches to modeling in mechanics and the historical development of these models are also briefly presented. The discrete model has been enriched by different additional features that are shortly mentioned. One of them is the introduction of the random fields as a way how to define the spatial variability. Such combination of models was used in various studies before, some of them are listed.

The discrete model itself is described in Chap. 3. In the first part of the chapter, the basic numerical model (referred to as deterministic model) is introduced. The process of the definition of the random inner structure is elucidated and the corresponding mechanical relations and model parameters are stated. The constitutive relation controlling stress at the bond between two particles (including the post-critical behavior of the bond with the exponential softening) is presented as well. The second part of the chapter deals with the probabilistic extension of the model (referred as probabilistic model). The random field generation is explained including the problem of generation of non-Gaussian correlated variables. Then, a procedure enabling faster computational process of assigning of the random value to each individual contact (Expansion Optimal Linear Estimation method) is also introduced.

The practical part of the thesis begins in Chap. 4. The description of the laboratory experiment (taken from literature) as well as the process of parameter identification and model validation can be found here. The results of the experiments on three different configurations of the concrete beams (deeply-notched, shallowly-notched and unnotched) in four different sizes loaded in three-point bending are described. The results adopted from literature [27] have been separated into two parts: the first data set has been utilized for the identification of model parameters and the other one for the subsequent model validation. The parameters for the deterministic model and for the probabilistic extension has been found separately. The process of the identification is described in detail. The model response is compared to the data measured in the experiment and the difference in the peak load and the variability of the response is discussed.

The following Chaps. 5 and 6 deliver the main results of the numerical analysis by the enhanced discrete model. Chapter 5 already deals with the probabilistic model and above all with the influence of the correlation length, parameter defining the rate of change of the random field. The computational study is performed to obtain data

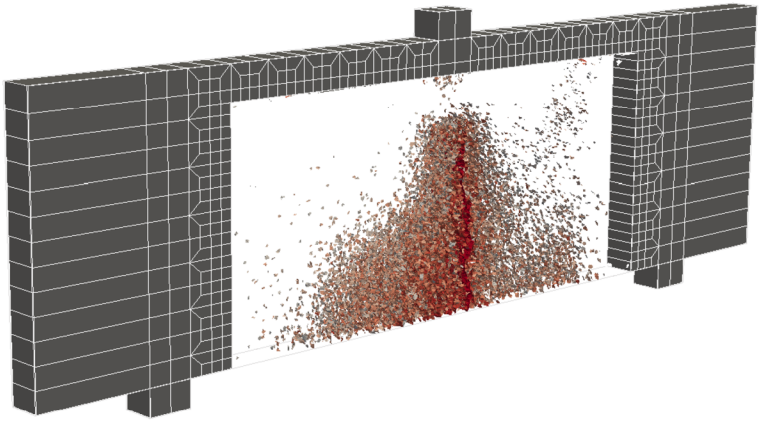

Fig. 1.1: Simulation of the bending experiment with the discrete model: final stage with developed macrocrack. Red color marks the contacts with high value of damage parameter.

showing the dependence between the mean strength of the bent beam and correlation length of the random field (defining the tensile and shear strength and the fracture energy in tension and in shear). With the validated model, a new series of concrete beams has been designed and used for another (more detailed) computational study. Description and derivation of variability of the model combining two sources of disorder (the random inner arrangement of particles and the random field controlling some parameters) is presented. All the results are shown for three configurations of the beam (two with a notch of a different depth and one unnotched). The difference in their behavior is clearly demonstrated and discussed.

The final Chap. 6 concentrates on the zone in which the most intensive energy release takes place. Such zone, active during the whole loading period, is tracked with a special focus on the peak step when the specimen reaches its maximum load. Again, a wide set of specimens is statistically processed. Several options of postprocessing of the data are suggested and their results are compared. A general shape and size of the active zone is found and described.

The main findings and results of the described study are listed and summarized in the Conclusion (Chap. 7). Further suggestions for the future research are stated.

2 STATE-OF-THE-ART

Mechanics of fracture and damage of quasibrittle materials such as concrete focuses on the investigation of the crack propagation occurring in a particular zone around the crack tip. This zone (fracture process zone, FPZ) of such materials is characterized by an inelastic phenomena and its size is usually not negligible compared to the structural size. The classical linear elastic fracture mechanics (LEFM) presumes that the FPZ is a very small region (almost a point) but that does not correspond to the FPZ of concrete, unless the structure is extremely large. To study this region, it is necessary to simulate the FPZ of concrete structures directly. During the last decades, several mathematical and numerical models have been developed for this purpose.

A brief overview of these models according to their classification will be now introduced.

The first category of such numerical models are the **continuum models**. Common way of solving the continuum models is, e.g. the finite element method (FEM) which divide (discretize) the material into elements of small volume whereon the approximation of displacement is prescribed.

- One of the oldest models is the *cohesive* (or *fictitious*) *crack model* developed for concrete by Hillerborg et al. [30]. The model assumes that adjacent surfaces of already formed crack may still transfer stress (the crack has a pre-defined path). FPZ is described as a line and its width H_{FPZ} does not influence the model as it is not included in the formulation. This model is not a classical continuum model as it describes the inelastic strain in a discrete form.
- *Crack band model* solves the problem with discontinuity by introducing the FPZ width, H_{FPZ}, directly into the formulation of the constitutive relation. This width is assumed to be the material property. The model is also referenced as "*smeared crack*" model as the inelastic strain is considered distributed into the whole volume of discretization unit and the discontinuity of strain appears at the FPZ boundary. The crack band model can be simply introduced into the standard finite element codes as it can be generalized for the triaxial loading, in the contrary to the cohesive crack model. Nevertheless, these two models (cohesive crack and crack band model) are equivalent for the mode I fracture. The model was introduced by Bažant and Oh [8].
- *Nonlocal models* (for the overview see [7]) deal with the material meso-level heterogeneity by incorporating the characteristic internal length of the material. These models can handle the boundary value problem, non-physical strain localization or the mesh sensitivity in numerical computations. The continuum and smooth distribution of the strain within FPZ leads to an ap-

propriate representation of its behavior. Nevertheless, the nonlocal models are much more demanding on the computational power compared to the previous two model types.

All the above mentioned models can be used in connection with the *damage based models* as they handle the inelastic part of the strain by introduction of some material degradation in a form of the modification of the elastic constants. The damage can be in the simpler form just a single value or it can be a tensor describing the damage of the anisotropic materials.

Another approach is to model the material directly as an assembly of discrete units (bars, rigid cells, particles). On a meso-level scale, these **discrete models** can embrace the heterogeneity of the material (concrete) directly by their nature. The displacement field of a discrete model is discontinuous (not smooth). This enables to successfully describe such phenomena occurring in FPZ as microcracking or aggregate bridging. The meso-level approach describes the material and its inner structure on a meso-scale: for concrete, the individual grains of aggregates are distinguished on such scale level (approximately $10^{-4} - 10^{-1}$ m [55]).

In the past, many different discrete models have been developed. The first published application of the classical *lattice model* was by Herrmann in 1989 [29]. The lattice was made of the elasto-brittle 1D elements. Its geometry of lattice was independent of the inner heterogeneous structure of the modeled material (only lattice structure without any grains). The layout of aggregates was projected onto the lattice and the elements were divided into three types: aggregate, matrix or interface (depending on the position of both of their nodes). Such meso-level lattice models are convenient to model very small test specimens only (i.e. few times larger than its grain size), as they need a high resolution and thus they are computationally expensive.

Typically, the lattice models are used in connection with meso-structure of the material. To reduce the computational demand, less dense lattice with each node corresponding to one dominant aggregate can be exploited. Such simpler models may be designed to have only transitional degrees of freedom and axial connections (truss principle). One of the first simulations with such model was the network model by Burt and Dougill [11], some later numerical studies are described in [4, 36, 37].

To employ the lattice model in a larger scale modeling (for the structural level), the homogeneous lattice network is more convenient [10]. Some examples of the modeling by the classical lattice model can be found in literature [52, 33, 48, 38, 56, 49].

The extension of the model in 2D (aggregate interface model [62]) and subsequently in 3D by incorporating also the particles rotations and interparticle shear interactions made the model more realistic and utilizable. Recently, the model is

being further developed in work of Cusatis [12, 14, 15]. The *lattice particle model* described in his papers takes into account the three-dimensional rotations of model particles causing the shear and bending actions in the interparticle contacts. The constitutive law in terms of interface stress and strain vectors will be described in the following chapter. Its main advantage is the possibility to include not only the crack opening but also frictional and dilatant slip on the plane of distinct orientations.

The model was recently extended by other phenomena such as deterioration effect, chloride diffusion [61, 1] or fibre reinforcement [42, 43]. In some studies, the cracking events during the model simulation were compared with the data measured by acoustic emission method in laboratory experiments [35, 28]. Nevertheless the complexity of the meso-level lattice models leads to enormous computational power which limits the applicability of such models to smaller (unstructural) bodies so far.

Another tendency to improve the model aims to incorporate the random fluctuation of the mechanical material parameters [25, 21]. The source of this fluctuation can be different: from the random properties of the concrete components (e.g., different geometrical and mechanical properties of aggregates) through the irregularities originated in the mixing and casting process (different spatial distribution of grains, water and other components, the influence of the boundaries) to the effect of uneven drying of casted concrete elements.

It is a challenging task to define the spatial randomness of the material: first, we have to identify somehow the parameters of the certain random entity which is very difficult to measure. Another problem is to identify the parameters of the deterministic model themselves. The presence of the random material fluctuations complicate their measurement, as it is not possible to measure only the deterministic parameters without the influence of the material randomness.

The particle model itself in its basic (deterministic) form is able to cover the material randomness in some measure due to its random meso-level structure. However looking at the experimental data, another source of disorder needs to be employed to simulate results similar to the experimental ones. Widely used form of modeling of the fluctuation of some random parameters is the stationary random field [60, 25, 26, 54]. For this probabilistic extension of the model, the probability distribution type, the correlation function and all their parameters have to be found for each random parameter plus the mutual dependence among all the random variables.

The following chapter will introduce the model used in this thesis and explain its mechanical behavior.

3 DISCRETE MODEL

Discrete modeling of materials offers a couple of advantages compared to the classical continuum models. They are particulary convenient for modeling of composite materials due to their capability to represent the heterogeneous inner structure. At the same time, thanks to relatively simple formulation of the constitutive law, it is possible to represent complex phenomena such as material softening in direction perpendicular to the cracks, etc. Their high demand on the computational power shall be mentioned. Despite this, the modeling of materials by the discrete models is not rare in the scientific practice these days.

3.1 Lattice-particle model

The model employed in the thesis is a 3D lattice-particle model developed by Cusatis, Bažant and Cedolin [13, 12, 14]. This model describes the inner structure of the concrete on a meso-scale level: each particle of the model corresponds to one coarse mineral aggregate. The particles are interconnected and the constitutive law prescribed on these connections define the interaction of the aggregates through the matrix and also takes into account the influence of the lower-scale structure (finer aggregate grains, cement paste, cement-aggregate interaction).

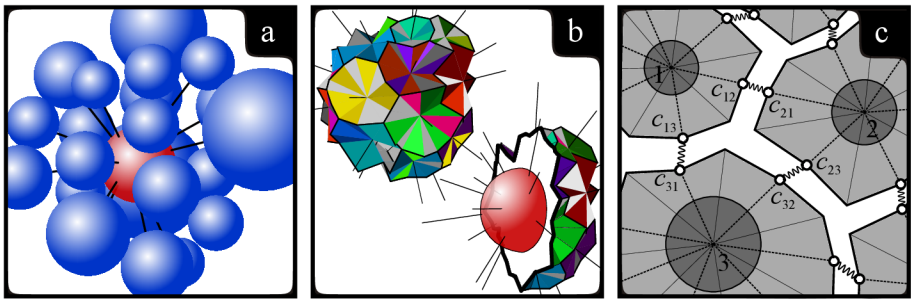

Fig. 3.1: a) Random placement of the grains – simulated meso-structure. b) Rigid cells created by tessellation. c) Contact between adjacent cells. Figure adopted from [21].

Random geometry

The inner structure of the model is created in an automatic procedure: at first, the domain of the modeled concrete member is gradually filled with a randomly located spheres of a random diameter, Fig. 3.1a. The predefined sieve curve has to be respected while determining a new diameter and none of the generated spheres are allowed to intersect. The procedure allocates the spheres randomly into the domain in a sequence from the largest to the smallest size. This random procedure should

eliminate the directional bias. After a large number of rejected trials to allocate a new sphere into the domain, the volume is considered to be fully saturated.

In a following step, the spherical centers are connected by Delauny triangulation [16] and the lattice is created. The whole volume is then divided by tessellation and each sphere together with its surroundings creates a rigid cell, Fig. 3.1b. The contact facet of two neighboring cells is always perpendicular to the connection line of two centers and intersects it in the middle of the free part of the line between the spheres (the part devoted to the matrix), Fig. 3.1c. The facet is created by a projection of the contact area between two particles into the plane perpendicular to their connection line and it is also the area through which the interaction forces are transmitted from one aggregate to the adjacent ones and on which the constitutive law governing the mechanical behavior of the model is defined. The centroid of the facet is denoted $\boldsymbol{c}$ and usually does not lie on the connecting line. This is the point of application of the interaction forces between two particles (different from original Cusatis' model that applies the forces on each of the subplane of the facet).

In the following section, the kinematics and statics of the used model will be described. The notation is followed according to paper by Eliáš [18].

Rigid body kinematics and statics

Each center of the generated sphere will serve as one node of the model with three translational, $\boldsymbol{u}$, and three rotational, $\boldsymbol{\theta}$, degrees of freedom (DOF). Based on the kinematics of the ideally rigid bodies, the displacement field and the displacement jump at the contact point between two cells can be described as follows: the coordinates of two adjacent cells i and j (their nuclei) are $\boldsymbol{x}_i = [x_{1i}, x_{2i}, x_{3i}]^{\mathrm{T}}$ and $\boldsymbol{x}_j$ – see Fig. 3.2. The translation of point i is denoted $\boldsymbol{u}_i = [u_{1i}, u_{2i}, u_{3i}]^{\mathrm{T}}$, the rotation $\boldsymbol{\theta}_i = [\theta_{1i}, \theta_{2i}, \theta_{3i}]^{\mathrm{T}}$. Assuming small rotations, according to rigid body motion, the displacement of any point $\boldsymbol{x}$ inside the cell with the nucleus i can be expressed

$$\boldsymbol{u}(\boldsymbol{x}) = \boldsymbol{u}_i + \boldsymbol{\theta}_i \times (\boldsymbol{x} - \boldsymbol{x}_i) = \boldsymbol{A}_i(\boldsymbol{x}) \begin{bmatrix} \boldsymbol{u}_i \\ \boldsymbol{\theta}_i \end{bmatrix} \tag{3.1}$$

where the matrix $\boldsymbol{A}_i(\boldsymbol{x})$ can be written as

$$\boldsymbol{A}_i(\boldsymbol{x}) = \begin{bmatrix} 1 & 0 & 0 & 0 & x_3 - x_{3i} & x_{2i} - x_2 \\ 0 & 1 & 0 & x_{3i} - x_3 & 0 & x_1 - x_{1i} \\ 0 & 0 & 1 & x_2 - x_{2i} & x_{1i} - x_1 & 0 \end{bmatrix} \tag{3.2}$$

The discontinuity of displacement $\boldsymbol{\Delta}_{ij}$ at the facet between two adjacent cells i

and j is then

$$\boldsymbol{\Delta}_{ij} = \begin{bmatrix} \Delta_{1ij} \\ \Delta_{2ij} \\ \Delta_{3ij} \end{bmatrix} = \boldsymbol{A}_j(\boldsymbol{c}) \begin{bmatrix} \boldsymbol{u}_j \\ \boldsymbol{\theta}_j \end{bmatrix} - \boldsymbol{A}_i(\boldsymbol{c}) \begin{bmatrix} \boldsymbol{u}_i \\ \boldsymbol{\theta}_i \end{bmatrix} \tag{3.3}$$

where $\boldsymbol{c}$ denotes the coordinates of the centroid c (contact point) of the facet between cells. The components of the strain vector $\boldsymbol{\varepsilon}$ (the normal and the shear strains in local coordinates) are calculated from the displacement discontinuity vector $\boldsymbol{\Delta}_{ij}$ as

$$\boldsymbol{\varepsilon} = \begin{bmatrix} \varepsilon_N & \varepsilon_M & \varepsilon_L \end{bmatrix}^{\mathrm{T}} = \begin{bmatrix} \boldsymbol{n} & \boldsymbol{m} & \boldsymbol{l} \end{bmatrix}^{\mathrm{T}} \boldsymbol{\Delta}_{ij}/L \tag{3.4}$$

where L is the distance (length) between nuclei of the appropriate cells. The unit vectors define the direction (normal vector $\boldsymbol{n}$ is perpendicular to the contact facet and two tangential vectors $\boldsymbol{m}$ and $\boldsymbol{l}$ are mutually orthogonal and lie in the contact plane).

Having the strain $\boldsymbol{\varepsilon}$, the stress vector $\boldsymbol{\sigma}$ (normal and shear components) can be calculated from the damage constitutive relation

$$\boldsymbol{\sigma} = \begin{bmatrix} \sigma_N \\ \sigma_M \\ \sigma_L \end{bmatrix} = (1-D)\,E \begin{bmatrix} \varepsilon_N \\ \alpha\varepsilon_M \\ \alpha\varepsilon_L \end{bmatrix} \tag{3.5}$$

Based on the discontinuity of displacement, the contact forces can be evaluated as

$$\boldsymbol{F} = \begin{bmatrix} F_N \\ F_M \\ F_L \end{bmatrix} = \boldsymbol{\sigma} A = (1-D)\,\frac{EA}{L} \begin{bmatrix} \boldsymbol{n}^{\mathrm{T}}\boldsymbol{\Delta}_{ij} \\ \alpha\boldsymbol{m}^{\mathrm{T}}\boldsymbol{\Delta}_{ij} \\ \alpha\boldsymbol{l}^{\mathrm{T}}\boldsymbol{\Delta}_{ij} \end{bmatrix} = (1-D)\,EA\boldsymbol{\varepsilon} \begin{bmatrix} 1 & 0 & 0 \\ 0 & \alpha & 0 \\ 0 & 0 & \alpha \end{bmatrix} \tag{3.6}$$

with D as the damage parameter, A as the area of the contact facet and E and α are two elastic material parameters providing the normal stiffness EA/L and tangential stiffness $\alpha EA/L$. The elastic constant E of the model is calculated from the link model, where the assumption of the aggregates and matrix representing segments of the in-series connected system is exploited.

$$E = \frac{L}{L_{\mathrm{a}}/E_{\mathrm{a}} + L_{\mathrm{c}}/E_{\mathrm{c}}} = \frac{L}{L_{\mathrm{a}}/3E_{\mathrm{c}} + L_{\mathrm{c}}/E_{\mathrm{c}}} \qquad L_{\mathrm{a}} = R_1 + R_2 \qquad L = L_{\mathrm{a}} + L_{\mathrm{c}} \tag{3.7}$$

The moduli E_{c} and $E_{\mathrm{a}} = 3E_{\mathrm{c}}$ [14] characterize the elastic behavior of the matrix and the aggregates and R_i, R_j are the radii of each of the two spherical particles (aggregates). The distance between two particles, L, is divided into the part L_{a} belonging to the aggregates (i and j) and L_{c} belonging to the matrix – see Fig. 3.2.

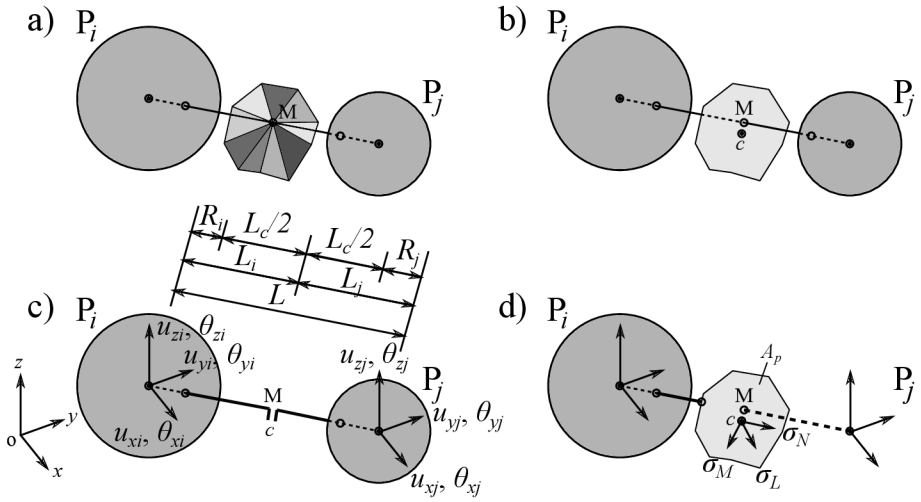

Fig. 3.2: a) Contact area (potential crack surface) between two adjacent particles; b) projected contact area; c) geometry and degrees of freedom of a connection strut; d) stress acting on the contact area. Figure adopted from [14].

Nonlinear model with damage parameter

The material model was adopted according to G. Cusatis [12, 14, 15] and some simplifications by J. Eliáš [18] were implemented.

The nonlinearity of the model is dictated by the damage parameter D. The deterioration of the contact corresponds to the cracking in the cement paste and the interfacial transition zone between the aggregate and the matrix. The damage parameter describes the loss of material integrity in both, the normal and the shear directions and depends on the contact strain and the previous loading history. The value ranges between 0 (for healthy material) to 1 (for fully damaged material with zero strength) and is calculated in terms of the equivalent stress and the equivalent strain

$$D = 1 - \frac{\sigma_{\text{eq}}}{E\varepsilon_{\text{eq}}} \tag{3.8}$$

The equivalent strain, ε_{eq}, is calculated from the normal and tangential components of the strain vector

$$\varepsilon_{\text{eq}} = \sqrt{\varepsilon_N^2 + \alpha\left(\varepsilon_M^2 + \varepsilon_L^2\right)} \tag{3.9}$$

The equivalent stress, σ_{eq}, is defined as

$$\sigma_{\text{eq}} = \min \left\{ \begin{array}{c} \left(1 - D_{\text{prev}}\right) E\varepsilon_{\text{eq}} \\ f_{\text{eq}} \exp\left(\dfrac{K}{f_{\text{eq}}} \left\langle \chi - \dfrac{f_{\text{eq}}}{E} \right\rangle\right) \end{array} \right\} \tag{3.10}$$

The upper term in the minimum corresponds to case when there is no damage increase in the current step (the value of damage from previous step D_{prev} is exploited).

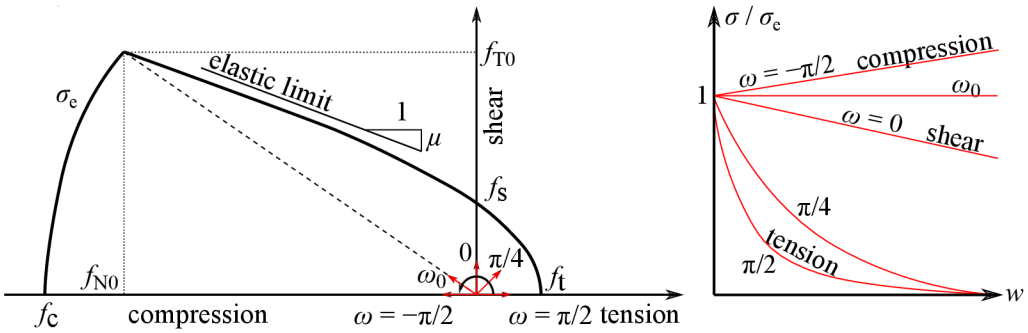

Fig. 3.3: Constitutive law according to [14]: the elastic envelope (right) and the exponential softening (left). Figure adopted from [21].

The bottom term takes into account the development of damage in the current calculation step. The angle brackets returns the positive value only: $\langle \bullet \rangle = \max\{\bullet, 0\}$. The relation also includes the equivalent strength, f_{eq}, the initial slope in nonlinear regime, K, and a variable χ representing the loading history.

The equivalent strength, f_{eq}, is a function of the straining direction, ω, which is calculated as

$$\tan\omega = \frac{\sigma_N\sqrt{\alpha}}{(\sigma_M^2 + \sigma_L^2)} \tag{3.11}$$

For the pure shear, the angle equals $\omega = 0$ while for the pure compression or tension $\omega = \pm\pi/2$. The equivalent strength encloses the elastic domain of the loading and is defined as

$$f_{\mathrm{eq}} = \begin{cases} \dfrac{16 f_{\mathrm{t}}}{\sqrt{\sin^2\omega + \alpha\cos^2\omega/\beta}} = \dfrac{16 f_{\mathrm{t}}}{\sqrt{\sin^2\omega + \alpha\cos^2\omega}} & \omega < \omega_0 \\ f_{\mathrm{t}}\dfrac{4.52\sin\omega - \sqrt{20.0704\sin^2\omega + 9\alpha\cos^2\omega}}{0.04\sin^2\omega - \alpha\cos^2\omega} & \omega \geq \omega_0 \end{cases} \tag{3.12}$$

where β is a parameter of compressive elastic envelope and ω_0 corresponds to the straining direction in which the two functions of f_{eq} equal (intersect) – see Fig. 3.3 left. The formula was taken from [14] and simplified by the introduction of relations and values of model parameters recommended in [14] (shear strength, $f_{\mathrm{s}} = 3f_{\mathrm{t}}$, fracture energy in shear, $G_{\mathrm{s}} = 16G_{\mathrm{t}}$, and compressive strength, $f_{\mathrm{c}} = 16f_{\mathrm{t}}$). The values adopted directly from the literature [14] are: parameter of compressive elastic envelope, $\beta = 1$, and slope of elastic envelope hyperbola asymptote, $\mu = 0.2$. The values of listed parameters can be found in Tab. 4.4.

The model is simplified so that it has only two parameters in the elastic regime (elastic modulus of matrix, E_{c}, and parameter determining the macroscopic Poisson ratio, α) and two parameters in the inelastic (nonlinear) regime (tensile strength, f_{t}, and fracture energy in tension, G_{t}). The value of the other parameters is more difficult to find from the experiments, as their physical substance is not so straightforward. They are related either to the different failure mode or they need to be

determined from the larger data set.

For more about the identification of the model parameters, see Chap. 4.2.1.

The variable χ, representing the loading history of the facet, models the irreversibility of damage due to fracture at meso-level. It is a function of equivalent strain $\varepsilon_{\mathrm{eq}}$ and the straining direction ω

$$\chi = \begin{cases} \varepsilon_{\mathrm{eq}} & \omega < \omega_0 \\ \varepsilon_{\mathrm{eq}} \dfrac{\omega}{\omega_0} + \varepsilon_{\max} \left(1 - \dfrac{\omega}{\omega_0}\right) & \omega_0 \leq \omega < 0 \\ \varepsilon_{\max} & \omega \geq 0 \end{cases} \tag{3.13}$$

where $\varepsilon_{\max} = \sqrt{\max\left(\varepsilon_N^2\right) + \alpha \max\left(\varepsilon_M^2 + \varepsilon_L^2\right)}$.

The parameter of the initial slope of nonlinear regime, K, governs the evolution of the boundary. It is defined as

$$K(\omega) = \begin{cases} K_{\mathrm{c}} \left[1 - \left(\dfrac{\omega + \pi/2}{\omega_0 + \pi/2}\right)^{n_{\mathrm{c}}}\right] = 0.26E \left[1 - \left(\dfrac{\omega + \pi/2}{\omega_0 + \pi/2}\right)^{2}\right] & \omega < \omega_0 \\ -K_{\mathrm{t}} \left[1 - \left(\dfrac{\omega - \pi/2}{\omega_0 - \pi/2}\right)^{n_{\mathrm{t}}}\right] = -K_t \left[1 - \left(\dfrac{\omega - \pi/2}{\omega_0 - \pi/2}\right)^{n_{\mathrm{t}}}\right] & \omega \geq \omega_0 \end{cases} \tag{3.14}$$

The parameters K_{c} (initial slope of compressive hardening, $K_{\mathrm{c}} = 0.26E_{\mathrm{c}}$) and n_{c} (parameter of compressive hardening, $n_{\mathrm{c}} = 2$, both from [14]) control the nonlinear compressive and shear-compressive behavior (for straining direction $\omega \leq \omega_0$) at the meso-level and are considered as material constants. The parameter K is calculated from two values: K_{t} is the initial slope in softening in pure tension and K_{s} the same slope in pure shear.

$$K_{\mathrm{t}} = -K(\pi/2) = \frac{2Ef_{\mathrm{t}}^2 L}{2EG_{\mathrm{t}} - f_{\mathrm{t}}^2 L} \qquad K_{\mathrm{s}} = -K(0) = \frac{18\alpha Ef_{\mathrm{t}}^2 L}{32\alpha EG_{\mathrm{t}} - 9f_{\mathrm{t}}^2 L} \tag{3.15}$$

with the parameter n_{t} in power reading

$$n_{\mathrm{t}} = \frac{\ln\left(K_{\mathrm{t}}/(K_{\mathrm{t}} - K_{\mathrm{s}})\right)}{\ln\left(1 - 2\omega_0/\pi\right)} \tag{3.16}$$

The introduced version of the model (in its basic form) will be referred as a *deterministic model* in the following text. However, the response of the model is random due to the random inner structure.

3.2 Probabilistic discrete model

If the data measured on laboratory experiments are compared to the response of the deterministic model, the numerical experiments usually lack of some portion of variability. Due to this fact, the deterministic model has been extended by another source or disorder: the material parameters have been modeled as randomly varying in space. This spatial variability can be considered as naturally appearing due to, e.g., the production process (mixing, compaction, drying, etc.) or service life.

The common practice is to define the parameter variability in terms of a random field. For the sake of simplicity, only a single random field affiliating different possible sources of spatial variability has been used for the simulation. The correlation length, l_{c}, is the basic parameter defining the rate of fluctuation and can be considered as a characteristic length of the random field [57, 9]. The incorporation of the random fields into the used discrete model has already been performed in some studies [21], from which most of the theory of this section was taken. Such an extended model with an additional source of variability in a form of a random field will be referred to as a *probabilistic model* hereinafter.

A stationary random field assigns a random value of chosen material parameter to each inter-particle connection. Let us denote the value of cth realization of such discretized random field at an $\boldsymbol{x}$ coordinate $\boldsymbol{H}^c(\boldsymbol{x})$. The value of $\boldsymbol{H}^c(\boldsymbol{x})$ for a given coordinate $\boldsymbol{x}$ is a random variable H defined by the cumulative density function (CDF) $F_H(h)$. This CDF $F_H(h)$ is identical for any $\boldsymbol{x}$ as the random field is stationary.

To get a value of a variable X (in case of the model it stands for random mechanical parameters f_{t} and G_{t} and the scaling will be further discussed in Chap. 5.2) in any point $\boldsymbol{x}$, we evaluate

$$X(\boldsymbol{x}) = \bar{X}\,\boldsymbol{H}(\boldsymbol{x}) \tag{3.17}$$

where $\bar{X}$ is the mean value of the particular variable (some material parameter in

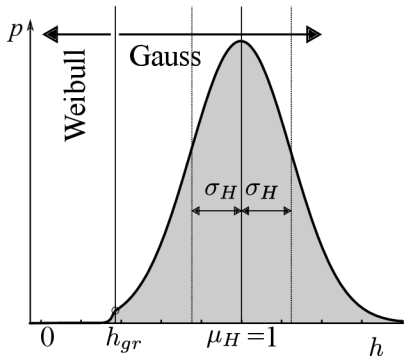

Fig. 3.4: Weibull-Gauss grafted probability distribution. Figure adopted from [21].

the deterministic model). The mean value of the random field equals one ($\bar{H} = 1$).

The random field F_H is adopted according to papers by Bažant and co-workers [5, 45, 44], see Fig. 3.4. They use a Gaussian CDF with a Weibullian tail grafted from the left side to approximate the strength of quasibrittle materials

$$F_H(h) = \begin{cases} r_f \left(1 - \exp\left(-\langle h/s_1 \rangle^m\right)\right) & h \leq h_{\mathrm{gr}} \\ p_{\mathrm{gr}} + \dfrac{r_f \int_{h_{\mathrm{gr}}}^{h} \exp\left(-\dfrac{(h-\mu_G)^2}{2\sigma_G^2}\right) \mathrm{d}h}{\sigma_G \sqrt{2\pi}} & h > h_{\mathrm{gr}} \end{cases} \tag{3.18}$$

where m is the parameter of shape (Weibull modulus), $\langle \bullet \rangle = \max(\bullet, 0)$, $s_1 = s_0 r_f^{1/m}$, s_0 is the scale parameter of the Weibull tail and μ_G and σ_G are the mean value and the standard deviation of the Gaussian distribution. The grafting probability p_{gr} (point of junction of Weibullian and Gaussian probability density function, PDF) can be calculated as

$$p_{\mathrm{gr}} = F_H(h_{\mathrm{gr}}) \tag{3.19}$$

with h_{gr} representing the grafting point. At this point, the equality between Weibullian and Gaussian PDF has to be fulfilled: $(\mathrm{d}F_H/\mathrm{d}h)|_{h_{\mathrm{gr}}^+} = (\mathrm{d}F_H/\mathrm{d}h)|_{h_{\mathrm{gr}}^-}$. To satisfy the condition of CDF $F_H(\infty) = 1$, the distribution is normalized by parameter r_f. The total number of distribution independent parameters is equal to four.

In this study, the fluctuations of the random field is controlled by the squared exponential autocorrelation function defining the dependence between any two points of the field. This dependence in form of the correlation coefficient ρ_{ij} is calculated as

$$\rho_{ij} = \exp\left[-\left(\frac{\|\boldsymbol{x}_i - \boldsymbol{x}_j\|}{l_{\mathrm{c}}}\right)^2\right] \tag{3.20}$$

based on the location vectors $\boldsymbol{x}$ of points i and j and one additional parameter – the correlation length, l_{c}. The random field $\boldsymbol{H}$ of a non-Gaussian variable H is generated by a transformation of a Gaussian random field $\hat{\boldsymbol{H}}$ by the isoprobabilistic transformation

$$\boldsymbol{H}(\boldsymbol{x}) = F_H^{-1}\left(\Phi\left(\hat{\boldsymbol{H}}(\boldsymbol{x})\right)\right) \tag{3.21}$$

where Φ is the CDF of the standard Gaussian distribution. Due to such transformation, the correlation structure of the random field $\boldsymbol{H}$ is distorted. Therefore, correlation coefficients have to be modified; it is done here by the approximation to the Nataf model [47] to fulfill the goal pairwise correlations of the non-Gaussian filed $\boldsymbol{H}$.

The method used for the generation of the random field in this study was the Karhunen-Loeve expansion where the covariance matrix $\boldsymbol{C}$ is spectrally decomposed.

The correlated Gaussian variables $\hat{\boldsymbol{H}}(\boldsymbol{x}_i)$ are transformed into standard Gaussian variables ξ_k which are independent and can be easily generated. For example, the cth realization of the correlated random field $\hat{\boldsymbol{H}}^c$ is evaluated using cth realization of K standard random variables $\boldsymbol{\xi}^c$ as

$$\hat{\boldsymbol{H}}^c(\boldsymbol{x}_i) = \sum_{k=1}^{K} \sqrt{\lambda_k} \xi_k^c \boldsymbol{\psi}_k(\boldsymbol{x}) \tag{3.22}$$

where λ and $\boldsymbol{\psi}$ are the eigenvalues and eigenvectors of the covariance matrix $\boldsymbol{C}$ and K is the number of eigenmodes summed up. The number of the largest eigenmodes, K, that are taken into account, is determined based on the requirement that the sum $\sum_{k=1}^{K} \lambda_k$ shall be at least 99 % of the trace of the covariance matrix $\boldsymbol{C}$ [58]. The method used for the sampling of the independent standard Gaussian variables $\boldsymbol{\xi}$ was the Latin Hypercube Sampling (LHS) with the use of the mean value of every subinterval. To reach the target unit correlation matrix, simulated annealing has been introduced in the sampling process [59].

The value of the sampled entity (i.e. the realization of the random field) has to be calculated for each interparticle facet of the discrete model. The number of facets in models used in this study can reach several hundred thousands which means that the evaluation of a random field would be extremely computationally expensive (due to the large covariance matrix $\boldsymbol{C}$). Therefore, the Expansion Optimal Linear Estimation method (EOLE) has been adopted [46]. In this method, the random field is initially evaluated on a regular orthogonal grid of nodes instead of the dense lattice-particle system. The spacing of the grid is about $l_c/3$ and an example is visualized in Fig. 3.5 left. The value at some facet is derived from the values on the grid as

$$\hat{\boldsymbol{H}}^c(\boldsymbol{x}) = \sum_{k=1}^{K} \frac{\xi_k^c}{\sqrt{\lambda_k}} \boldsymbol{\psi}_k^T \boldsymbol{C}_{xg} \tag{3.23}$$

with λ and $\boldsymbol{\psi}$ being the eigenvalues and eigenvectors of the covariance matrix of the grid nodes and $\boldsymbol{C}_{xg}$ is the covariance matrix between the center of the facet located at $\boldsymbol{x}$ and the grid nodes. An example of the random field projected from the grid onto the full system of facets is in Fig. 3.5 right. Once the values of the Gaussian random field has been assigned to each facet by EOLE, the values are transformed into the non-Gaussian space (Eq. 3.21).

Another advantage of the EOLE method that should be mentioned is its independence of the facet system and its geometry. Therefore, an sufficiently large realization of the random field on the grid is suitable for EOLE projection to use on any inner structure of the lattice-particle model. In the presented study, each random field realization generated on a large grid has been used for all the beams geometries which saved a lot of the computational time.

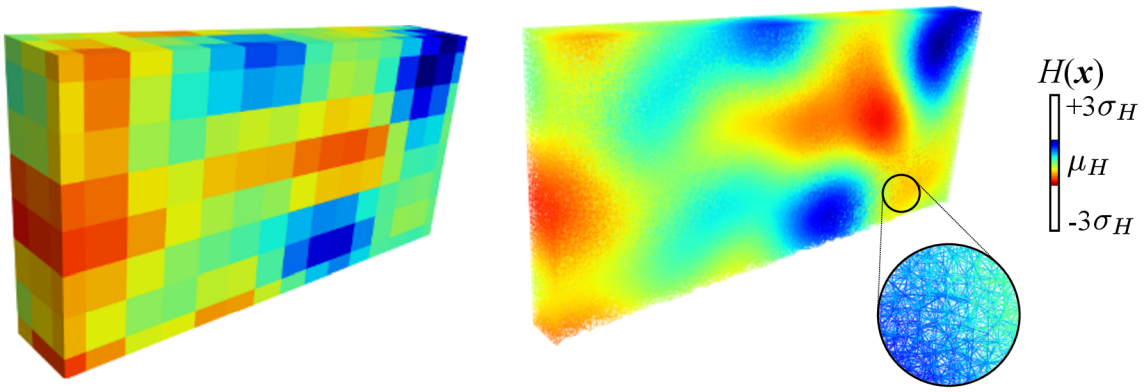

Fig. 3.5: One realization of a random field generated on a regular grid (left) and projected to the model elements (right). Figure adopted from [21].

3.3 Summary

The discrete lattice-particle model was briefly introduced and described. Its basic form (deterministic) has been adopted from the literature and extended by the spatial fluctuation of selected parameters in form of the autocorrelated random field. The following chapter will present the process of parameter identification based on the experimental data and the recommendations from literature and the subsequent validation of the model.

4 IDENTIFICATION OF THE MODEL PARAMETERS

In this chapter, the process of the parameter identification of the lattice-particle model in its basic (deterministic) and extended (probabilistic) form is introduced. Based on a wide set of experimental data, the parameters are identified and the model is validated afterwards. Some simplifications used in the presented study are also mentioned and the computational process is described.

4.1 Experimental data

Model parameters were identified on a set of experimental data form the Universit'e de Pau et des Pays de l'Adour, France, published in [27]. In the experiment, three types of concrete beams with different depth of a notch were tested in three-point bending, each in four different geometrically similar sizes. Deeply-notched beams (notch-to-depth ratio of $\alpha_{\mathsf{a}} = 0.5$, referred as half-notched) are marked with lower case letter a, shallowly-notched beams (notch-to-depth ratio of $\alpha_{\mathsf{b}} = 0.2$, referred as fifth-notched) with a lower case b and unnotched beams with c. The depth of the beams D was 400, 200, 100 and 50 mm, these size groups are marked with capitals A, B, C and D. The length of all beams was $3.5D$, the supports of the loading machine were located $0.5D$ from edges (bending span equals to $S = 2.5D$). All the beams shared the same thickness of $b = 50$ mm, the width of the notch was also kept constant and equal to 3 mm. The scheme of the individual specimen geometry is depicted in Fig. 4.1 for each size and notch group. Detailed geometry of the notched and unnotched beams is in Fig. 4.3.

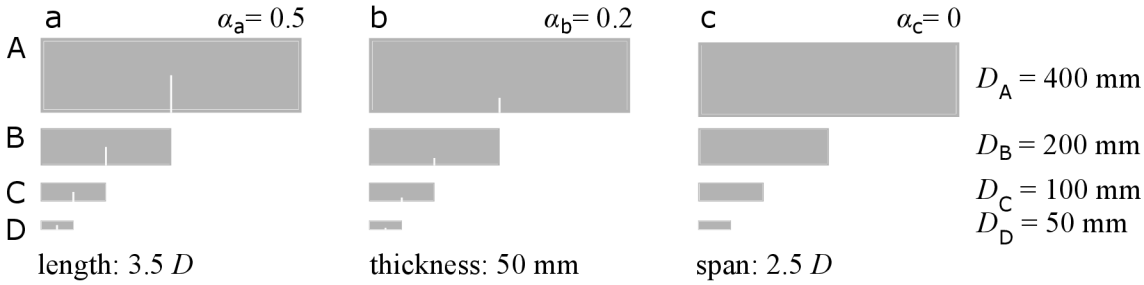

Fig. 4.1: Schematic overview of beam geometries tested in [27].

The material of the specimens was a ready-mix concrete mixture produced by Unibéton, France for paving slab applications. The mix composition is overviewed in Tab. 4.1, the grading curves for sand, coarser aggregates and the mix are in Fig. 4.2 (the figure was adopted from [27]). According to the paper, eight batches of concrete made with the same mix composition have been spent to cast the specimens. They

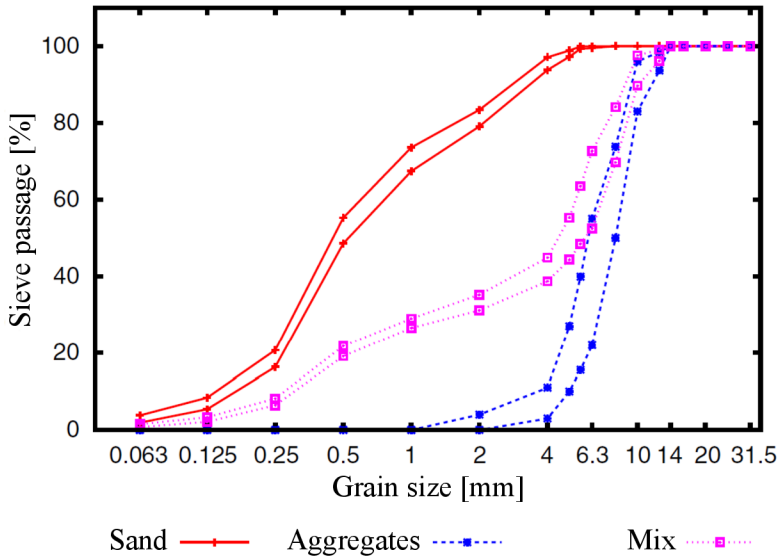

Fig. 4.2: Sand, aggregates and mix gradings. Figure adopted from [27].

were removed from their molds after 24 hours and stored in the water at room temperature. Specimens were removed from water 24 hours prior their testing. Additionally to the beams for bending tests, specimens for other supplemental tests have been produced to find the mechanical characteristics of each batch: 51 standard cylinders have been tested in the standard compressive test and splitting (Brazilian) test to measure the compressive strength, splitting tensile strength, Young's modulus and Poisson ratio. For three-point bending tests, two to five concrete beams have been manufactured for each size and notch configuration. Overall, 34 beams have been tested in three-point bending.

Tab. 4.1: Concrete mixture composition [27].

Product	**Designation**	**Mass** [kg]
sand	Cemex 0/4	740
aggregates	Durruty 4/10	1140
cement	Calcia CEM II/A	286
admixture	Axim Cimplast 115	1
water	clarified water	179
	Total	2346

The loading of the testing apparatus (servo-hydraulic testing machine Zwick-/Roell HB250) was controlled by the crack mouth opening displacement (CMOD) to avoid the post-peak unstable crack propagation. The CMOD was measured at the notch mouth for the notched specimens and between the two points at the distance of D (the beam depth) at the midspan on the bottom face of the beam for the

unnotched beams. In this case, the displacement is actually not a CMOD, however it is denoted so for the sake of simplicity. Overall, from 34 tested beams, 13 beams were deeply-notched, 11 shallowly-notched and 10 were unnotched (see Tab. 4.2 for an overview). The authors of [27] provided the results of the bending experiments in a form of a load−displacement (F − CMOD) curves and the values of the peak load $F_{\max}$. The $F_{\max}$ statistics for each specimen group can be seen in Tab. 4.3.

Tab. 4.2: Number of specimens tested in [27].

	a	b	c
A	3	3	2
B	5	3	3
C	2	3	3
D	3	2	2

Tab. 4.3: Results of three-point bending experiments from [27]: statistics of the maximum loading force $F_{\max}$.

	average			stdandard deviation			coefficient of variation		
	a	b	c	a	b	c	a	b	c
A	5.200	14.033	25.200	0.755	1.250	1.131	0.145	0.089	0.045
B	2.980	7.767	14.467	0.259	0.503	1.079	0.087	0.065	0.075
C	1.650	4.500	8.133	0.071	0.200	0.611	0.043	0.044	0.075
D	0.967	2.550	4.750	0.115	0.212	0.636	0.119	0.083	0.134

Figure 4.4 presents $F-$CMOD (load − gauge opening) curves of each specimen group. Three curves correspond to minimum, mean and maximum response measured during the bending tests [27]. The mean curve was used for the identification of material model parameters in Sec. 4.2. The two values presented below the group name correspond to the average peak load, $F_{\max}$ [kN], and to the average area under the curve, A [kN·mm]. These two values served for the identification of the tensile strength and the fracture energy.

Based on these experimental data, the parameters of the numerical model have been identified. In a previous work by J. Eliáš, et al. [21], the introduced model has been already used to simulate another experimental data [32, 31]. In this work, the methodology from [21] have been approximately followed to find the model parameters. Selected parameters have been identified based on the error minimalization method.

The error has been defined as an difference between the target value from the experiments and the simulated value from model response (Eq. 4.1). The information

about the concrete mix composition was not used in the parameter identification, the model grain size varied between 4 and 10 mm and followed the Fuller curve, which approximately corresponds to the sieve curve in Fig. 4.2.

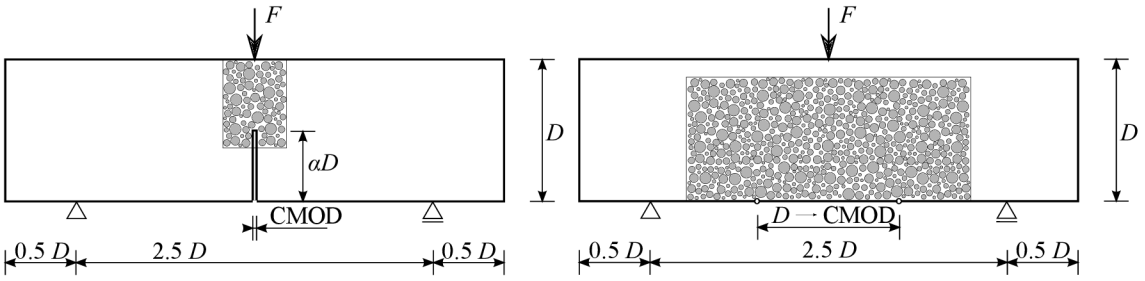

Fig. 4.3: Scheme of the concrete beam models: notched (left) and unnotched (right) beam.

Due to the high demand of the model on the computational power, the discrete model had been used only in regions where the cracks are most probable to appear to save the computational time: for the notched beams in the area around the notch and above it and for the unnotched beams in the region around the midspan. Figure 4.3 marks the discrete model region with the grey color. The rest of the beam has been modeled by the standard linear 8-node finite elements using a linear elastic material. The connection between the particles and the finite elements was made by auxiliary zero-diameter particles [20]. To find the elastic material constants of the finite elements, a uniaxial compression simulation was performed. The displacement field provided by particles was then fitted using least-square method by the equations of the linear elastic continuum.

The model used in the presented study was static: the static equilibrium needs to be found in an iterative way at the end of each solution step.

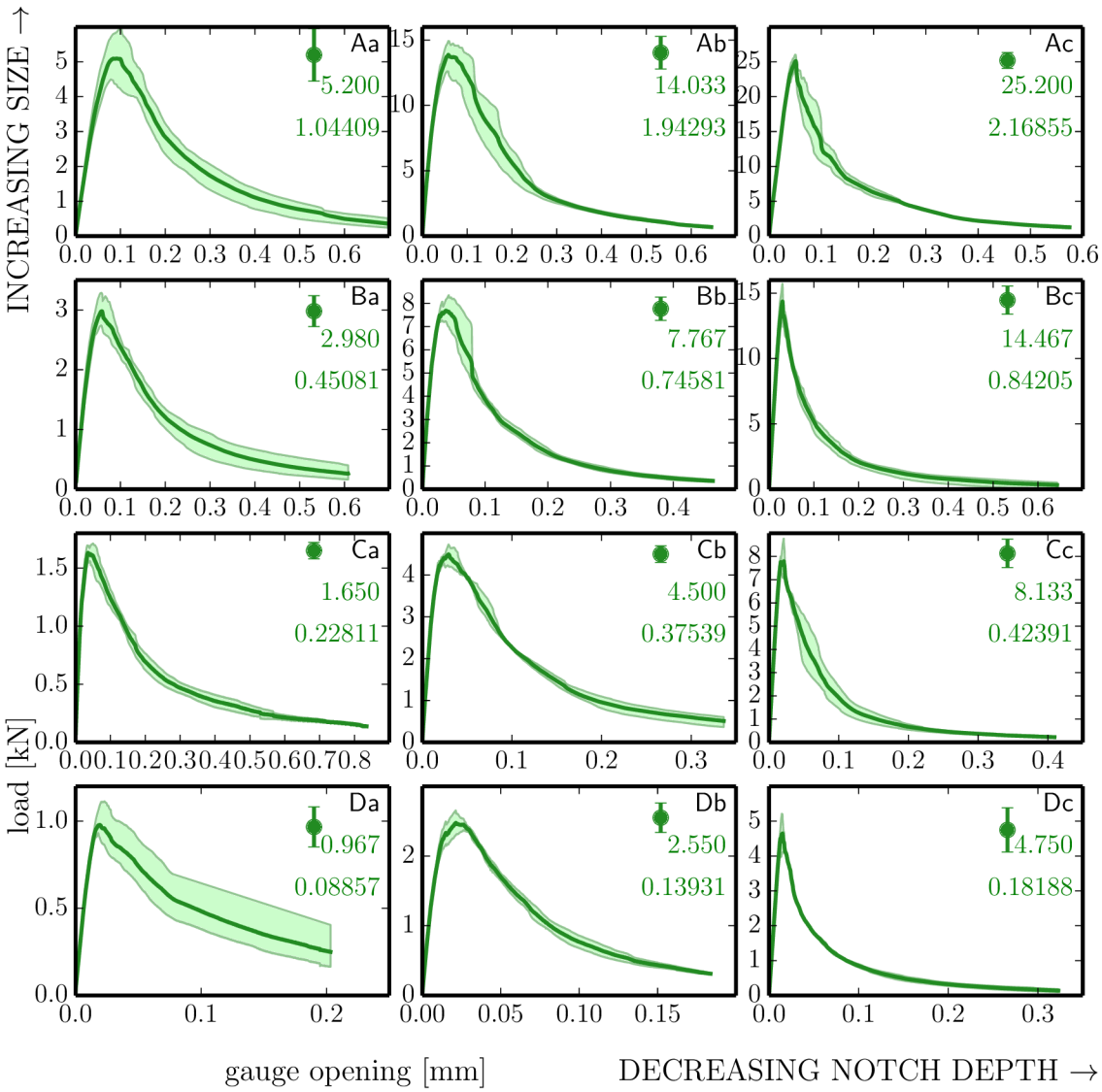

Fig. 4.4: Maximum, average and minimum response of each specimen group, data taken from [27]. The values in top right corners correspond to the mean peak load and the area under the mean curve.

4.2 Parameters identification

4.2.1 Parameters of deterministic model

The parameters of the deterministic model were found in the first step. The original model has 12 adjustable parameters, however, only four of them (some of those with a physical meaning) have been been identified: elastic modulus of matrix, E_c, tensile strength, f_t, fracture energy in tension, G_t, and the parameter α determining the macroscopic Poisson ratio. The value of the remaining parameters was either calculated using the relation to the other parameters or taken from [14].

The parameter α determining the macroscopic Poisson ratio was found to be 0.24, which corresponds to the Poisson ratio 0.21 (the value from experiments). The elastic modulus of matrix $E_c = 27$ GPa was fitted from the elastic part of the $F - \mathrm{CMOD}$ curve. It corresponds to macroscopic elastic modulus of 37 GPa which agrees with the experimental measurement [27].

The deterministic parameters (tensile strength, f_t, and fracture energy in tension, G_t) have been identified with help of only a part of the experimental data – the three largest sizes of beams with a deep and a shallow notch (groups Aa, Ba, Ca, Ab, Bb, Cb). The rest of the experimental data served for the validation of the model. The reason to use only notched beams for parameters fitting was the following: the spatial fluctuation of strength along the beam does not influence the average beam response due to the strong stress concentrator (a notch) which dictates the location of the crack. The tensile strength and the fracture energy have been evaluated from the maximum force, $F_{\max}$, measured during the loading and from the area A under the $F - \mathrm{CMOD}$ curve up to the specified opening value. The computational process of finding these two parameters consisted in minimalization of an error function, which was calculated as the square root of the sum of squares of two defined normalized errors (the difference between the target value from experiment and the actual value of the parameter from simulation). The error function, F_o, is then expressed as

$$F_o = \sqrt{\sum_j \left[\left(\frac{F^{\mathrm{exp}}_{\mathrm{max},j} - F^{\mathrm{sim}}_{\mathrm{max},j}}{F^{\mathrm{exp}}_{\mathrm{max},j}} \right)^2 + \left(\frac{A^{\mathrm{exp}}_j - A^{\mathrm{sim}}_j}{A^{\mathrm{exp}}_j} \right)^2 \right]} \quad \text{for} \quad j \in \left\{ \begin{array}{c} \mathsf{Aa}, \mathsf{Ba}, \mathsf{Ca}, \\ \mathsf{Ab}, \mathsf{Bb}, \mathsf{Cb} \end{array} \right\} \tag{4.1}$$

The overview of the values of all deterministic parameters is in Tab. 4.4. Three groups of parameters correspond to those identified based on the experiments, those calculated from their relation to the identified parameters and the constants adopted from literature.

Tab. 4.4: Parameters of the numerical model by Cusatis [14], simplified as in [21].

Parameter			value	
E_c	elastic modulus of matrix		$27 \cdot 10^9$	Pa
α	par. determ. the macroscop. Poisson ratio		0.24	–
f_t	tensile strength		$2.0 \cdot 10^6$	Pa
G_t	fracture energy in tension		25.1	N/m
E_a	elastic modulus of grains	$= 3 \cdot E_c =$	$81 \cdot 10^9$	Pa
f_s	shear strength	$= 3 \cdot f_t =$	$6.0 \cdot 10^6$	Pa
G_s	fracture energy in shear	$= 16 \cdot G_t =$	401.7	N/m
f_c	compressive strength	$= 16 \cdot f_t =$	$32.0 \cdot 10^6$	Pa
K_c	initial slope of compressive hardening	$= 0.26 \cdot E_c =$	$7.02 \cdot 10^9$	Pa
β	parameter of compressive elastic envelope		1.0	–
μ	slope of el. envelope hyperbola asymptote		0.2	–
n_c	parameter of compressive hardening		2.0	–

4.2.2 Parameters of probabilistic extension

Once the deterministic model parameters have been found, the parameters of the probabilistic extension could be identified. To simulate of the loading capacity of a quasi-brittle solid, the material strength and the fracture energy can be considered as the most important parameters. Therefore, the spatial variability of these two parameters is taken into account when simulating the fracture process by the probabilistic model. Here, the tensile strength of the material, f_t, and the tensile fracture energy, G_t, are considered to be linearly dependent on the random field value (Eq. 3.17), [25]. As an identical probability distribution and coefficient of variation have been used for all these parameters, a single random field could be used to generate values for both parameters.

The chosen distribution F_H (Gauss distribution with the Weibullian left-hand tail) is defined by four above-mentioned parameters of the distribution. To find one of them based on the experimental results – the coefficient of variation of the random field H (the other two parameters, m and p_{gr} were set according to literature and $\mu = 1$), the following assumption was exploited: if the strong stress concentrator is present, the influence of the spatial variability (correlation function) on the mean strength is negligible, as was shown in [22, 23]. The strength of the beams with a deep notch is dependent mostly on the material in the closest neighborhood of the notch tip, which is defined only by the probability distribution F_H. By introducing a strong stress concentrator, the influence of the correlation length becomes negligible and only the local properties of the random field (distribution F_H) matters

(Fig. 5.2). Therefore, the results from the tests on deeply-notched beams were used to determine CoV.

Coefficient of variation was identified from the results of the second largest beams with a deep notch (group Ba) as it had the highes population number of tested specimens. The minimum error (the difference in CoV between the experimental results and the simulated responses from the probabilistic model with the infinite correlation length) has been searched in an iterative procedure. Based on such optimization process, the CoV of F_H was estimated to be 0.14.

Parameters and their values used in the probabilistic simulations are in overview in Tab. 4.5. All parameters, except the correlation length, l_c, belong to the grafted Weibull-Gauss distribution (Eq. 3.18), but only four of them are independent.

Knowing the value of CoV, the correlation length, l_c, could be roughly estimated by matching the peak loads from experiments on unnotched beams, where the mean peak load strongly depends on the correlation length, as shown in [22, 23]. The value of correlation length of the random field of strength and fracture energy was estimated from the largest unnotched specimens (group Ac) to match the average peak load from experiments – see Fig. 4.5. The resulting estimate was $l_c = 0.1$ m.

Tab. 4.5: Parameters of the probability distribution (Eq. 3.18).

Parameter		value
μ	mean	1
σ_G	standard deviation of Gaussian core	0.14
m	Weibull shape parameter	24
s_1	Weibull scale parameter	0.7883
h_{gr}	grafting point	0.5909
$p_{\mathrm{gr}} = F_H(h_{\mathrm{gr}})$	probability at grafting point	0.001
CoV	coefficient of variation	0.14

With determined parameters of both, the deterministic and the probabilistic part of the model, numerical simulations have been performed. The simulated responses were compared to the experimental curves that have not been used for parameters identification and the performance of the model could be validated.

4.3 Model validation

Once the model parameters were identified, the performance of the model (deterministic and probabilistic) could be validated. While some of experimental data have been used to identify the model parameters, the rest could serve for the validation of the numerical model response.

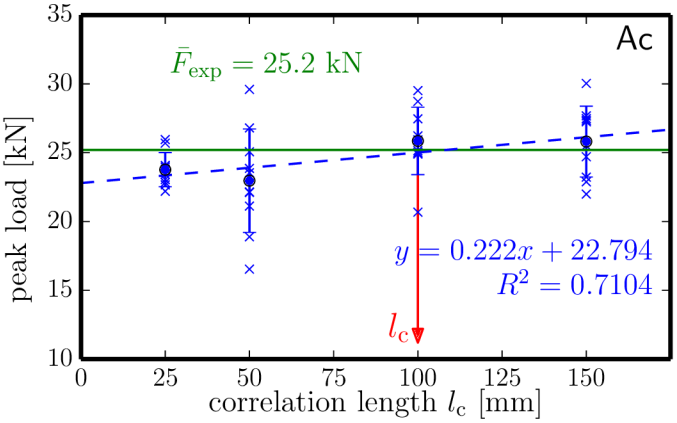

Fig. 4.5: Estimation of the correlation length: ten probabilistic simulations of Ac beam.

4.3.1 Deterministic simulations of the experiment

Ten simulations with the deterministic model were performed for each of the specimen type and size. The results of these simulations in the form of $F-\mathrm{CMOD}$ curves are plotted in Fig. 4.6 (red curves). The green region represents the experimental results which are limited by the minimum and maximum measured loading path.

The curves simulated by the deterministic model are in a good agreement with the experimental results. The model can predict the peak load as well as the post-critical part of loading. Nevertheless, the results for the smallest beams are not so accurate, even in the elastic regime: the reason can be in the discrete model with the given particle sieve curve and quite small specimen depth (the boundary problem has been already described by Eliáš [19]). The ligament is too short to accommodate enough grains and thus the accuracy of the model is limited. For the largest unnotched beams, the Newton iteration scheme does not converge in the post-peak phase.

Although the model is deterministic (with constant parameters for all ten simulations), its response is scattered. The reason is the random location and size of grains which is different for each simulation. Yet, the scatter of deterministic model is still not sufficient when compared to the experimental one. It is therefore believed that another source of disorder should be added to simulate more realistic response of concrete specimens. Such a source can be the random spatial fluctuation of parameters in form of a random field.

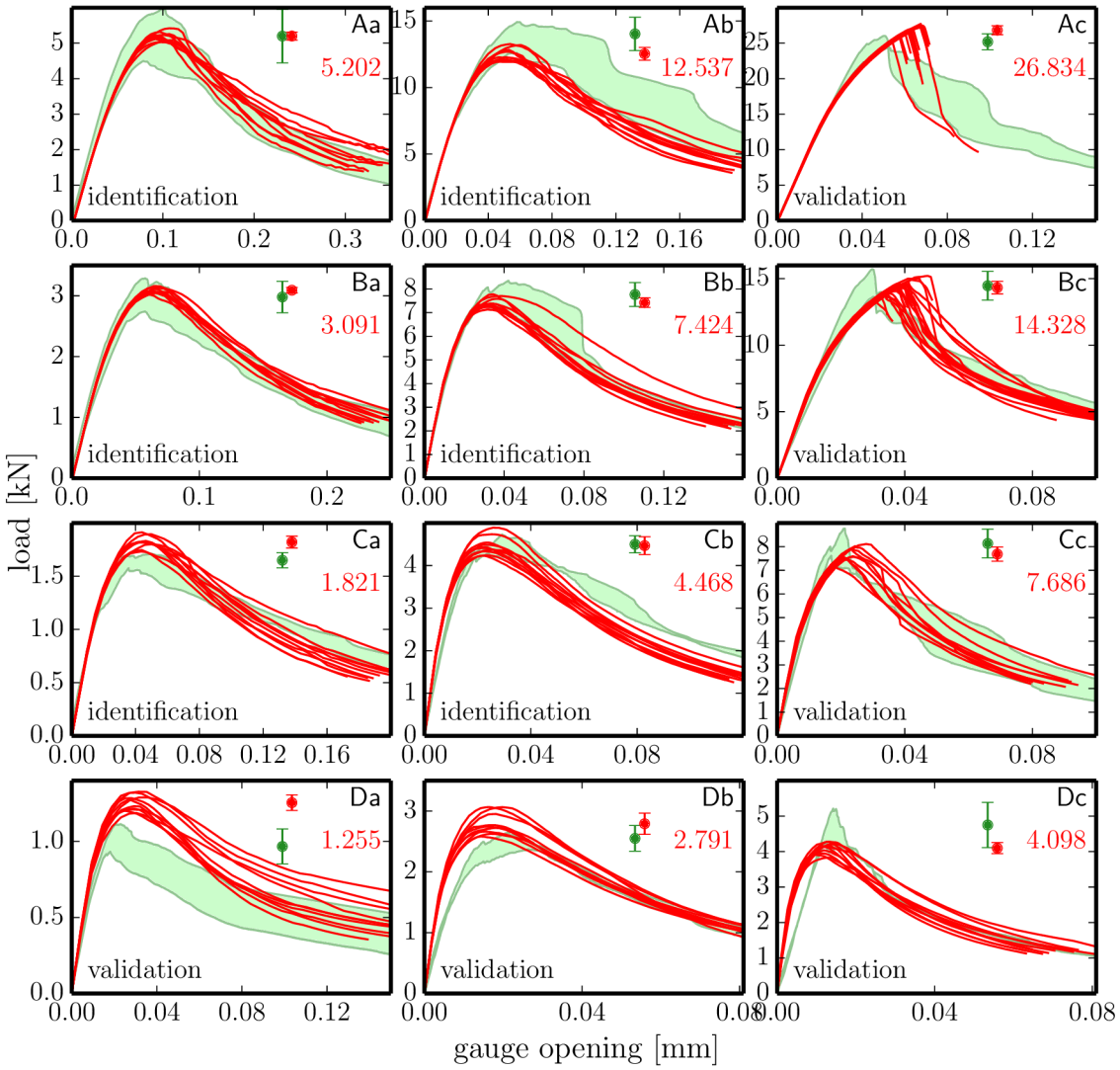

Fig. 4.6: Ten deterministic simulations (red) and the experimental data [27] (green). Errorbars show the average peak load (value in top right corner) and the standard deviation.

4.3.2 Probabilistic simulations of the experiment

With the probabilistic discrete model which contains both sources of material disorder (the heterogeneous random inner structure and the spatially fluctuating random material parameters), 24 simulations were performed. The obtained $F - \mathrm{CMOD}$ curves are plotted in Fig. 4.8. Again, the green region corresponds to the experimental data (minimum and maximum measured response borders the region), the blue lines belong to the probabilistic model. The deterministic and probabilistic parameters of the model used in these simulations are listed in Tabs. 4.4 and 4.5. The random field controlled the fluctuation of tensile strength and fracture energy in tension according to Eq. 3.17.

Again, the simulated responses are in good agreement with the experimental results. Comparing both types of simulations, it is obvious that after introducing the variability of the input parameters, the scatter in the maximum load as well as in the dissipated energy increased for the notched beams, while the mean value of the maximum force remained unchanged. For the unnotched beams, besides the increase of the response scatter, the decrease in the average maximum force is present. This can be explained by the higher probability of a presence of a weaker spot close to the bottom face of the beam where the crack initiates. The random field helps the inelastic strain to localize into macrocracks. Therefore, the problem with convergence of the iterative process in large unnotched beams is not so frequent (compared to deterministic model, Fig. 4.6).

Examples of two different beams simulated by the probabilistic model can be seen in Fig. 4.9: one deeply-notched beam (Aa) of the largest size and one unnotched beam of the largest size (Ac), both with their random field H used for the scaling of strength and fracture energy (the first row), the damage parameter at the peak load (the second row) and the damage parameter at the end of the simulation (third row). The figure nicely illustrates the localization of damage at the peak load and macrocrack formed at the end of the simulation.

4.4 Summary and size effect

The nominal strength $\bar{\sigma}_N$ has been evaluated based on the maximum load $F_{\max}$ reached during the test. The three-point bent beams of a rectangular cross section have the bending span $S = 2.5D$, the thickness $b = 0.05$ m and the varying depth D. The nominal strength, $\bar{\sigma}_N$, calculated as the theoretical maximum elastic stress

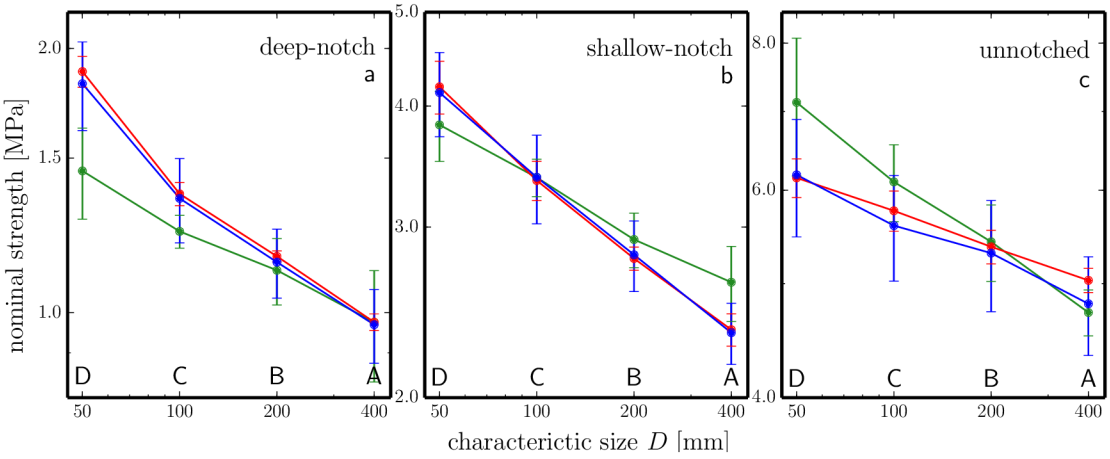

Fig. 4.7: Size effect diagrams: nominal strength vs. beam size. Experiments (green), deterministic (red) and probabilistic (blue) simulations.

using simple beam theory and neglecting the notch, equals

$$\bar{\sigma}_N = \frac{M}{W} = \frac{\frac{1}{4}F_{\max}S}{\frac{1}{6}bD^2} = \frac{3F_{\max}S}{2bD^2} = 75 \cdot 10^6 \frac{F_{\max}}{D} \tag{4.2}$$

The values of $\bar{\sigma}_N$ have been plotted against the size of the particular beams represented by its depth D in Fig. 4.7 for each of the test mode (a, b, c) to map the possible size effect [6].

It is obvious from the graphs that the mean nominal strength decreases with the increasing size of specimens. Such a size effect is present for all three test setups: deep, shallow and no notch beams. Regarding the standard deviation, the effect is the same for the notched beams: the larger the beam, the lower the standard deviation. For the unnotched beams, there is not any strong observable dependency of the standard deviation on the size.

With the validated model, a more advanced study of the influence of the correlation length on the overall response of the beam could be performed. Such a study will be introduced in the following chapter.

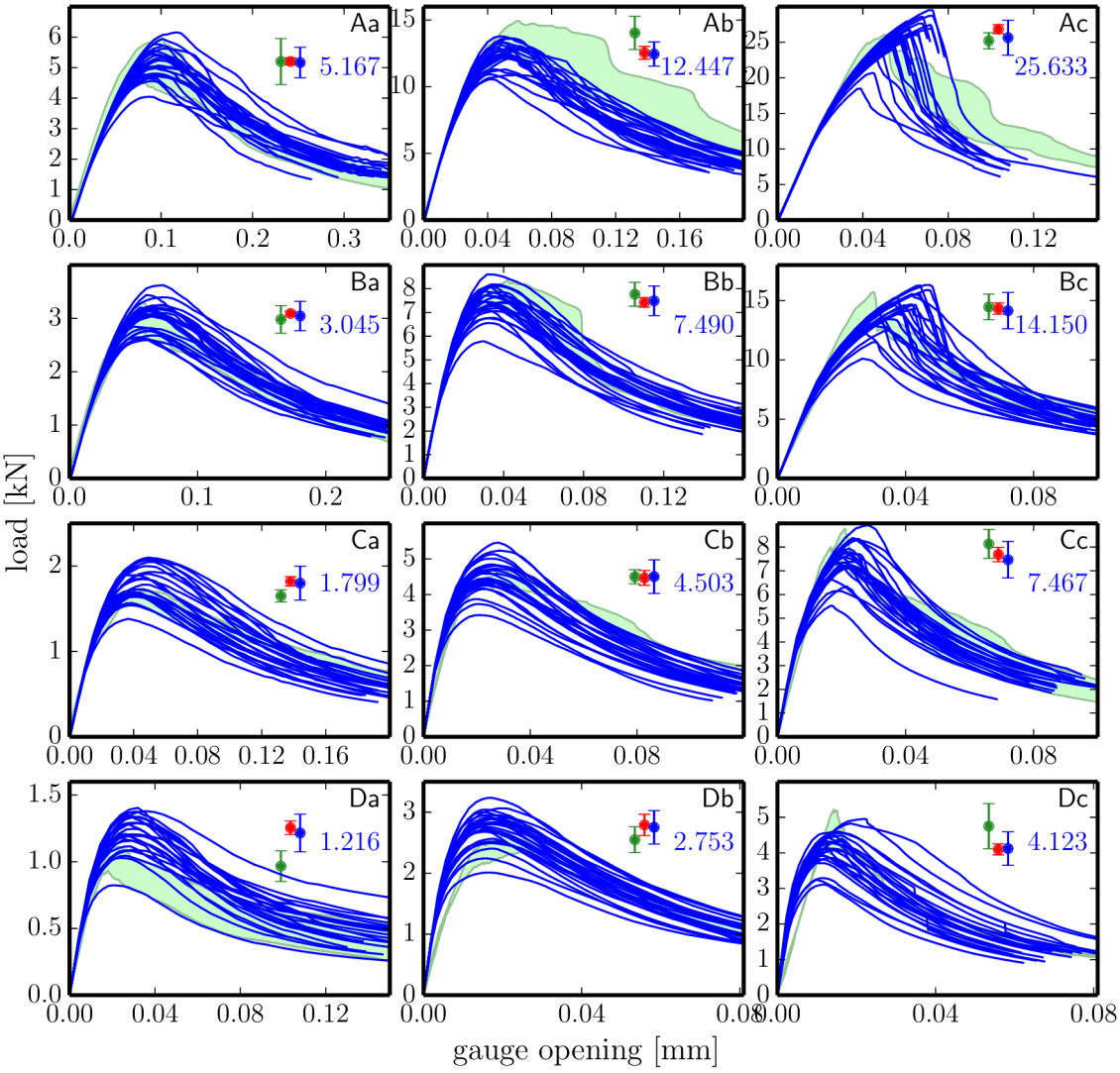

Fig. 4.8: Twenty four probabilistic simulations (blue) and the experimental data [27] (green). Errorbars show the average peak load (value in top right corner) and the standard deviation for experiments, deterministic and probabilistic model.

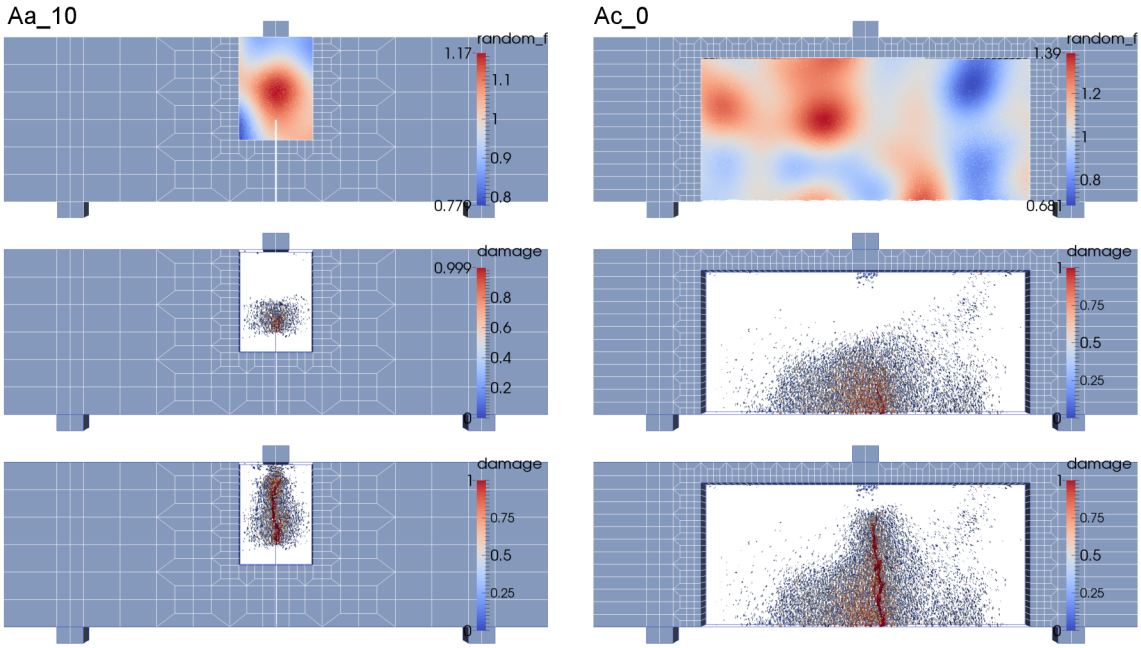

Fig. 4.9: Examples of two probabilistic simulations. Left: deeply-notched beam Aa. Right: unnotched beam Ac. First row: realization of the random field H used in the simulation; second row: damage parameter at the peak load; third row: damage parameter at the end of the simulation.

5 INFLUENCE OF THE CORRELATION LENGTH

In the previous chapter, the calibrated model demonstrated a good performance in simulations of bending experiments. Based on the experimental data, the parameters of the deterministic part of the model have been identified. The experimental data were used to identify also the parameters of the probabilistic part of the model, however, some further attention should be paid to the identification method of the correlation length. The correlation length, l_c, controlling the fluctuation of the random field was roughly estimated based on a single group of unnotched beams (group Ac with the largest beams). The influence of l_c on the model response will be discussed in this chapter.

5.1 Determining the correlation length on experimental data

The correlation length, l_c, has been roughly estimated in the previous chapter by matching the maximum load on the largest unnotched beams. The probabilistic simulations with the estimated $l_c = 0.1\,\mathrm{m}$ provided the results presented in Fig. 4.8. Nevertheless, it is interesting to investigate how the changing value of l_c influences the simulations. Therefore, an effect of changing l_c on the overall response has been investigated. First, the experiments [27] were used to describe the dependency.

A set of 24 probabilistic simulations was calculated for each size of deeply-notched (groups a) and unnotched (groups c) beams, repeatedly for different values of l_c. The correlation length varied between "zero" and infinity (overall 14 values of l_c have been considered). The zero correlation length refers to the probabilistic setup where each contact between particles has independent random value of h, yet all the values are sampled from the same probability distribution F_H. For the infinitely large correlation length, the random field $H(\boldsymbol{x})$ degenerates into a single constant (which is random for each simulation) value h in all its points – simulation with such a field is identical to the deterministic simulation with parameters multiplied by h. The mean peak load and its standard deviation have been estimated and the statistics were plotted versus the correlation length.

Figure 5.1 presents the dependency of the probabilistic mean peak load on the correlation length using 24 unnotched simulations in each size group. The results from the deterministic model and the experiment are also presented for comparison (red dashed line corresponds to the deterministic average peak load from 10 simulations, the green dotted line corresponds to the experimental mean peak load, shaded stripes show plus/minus standard deviation around the mean value). It can be ob-

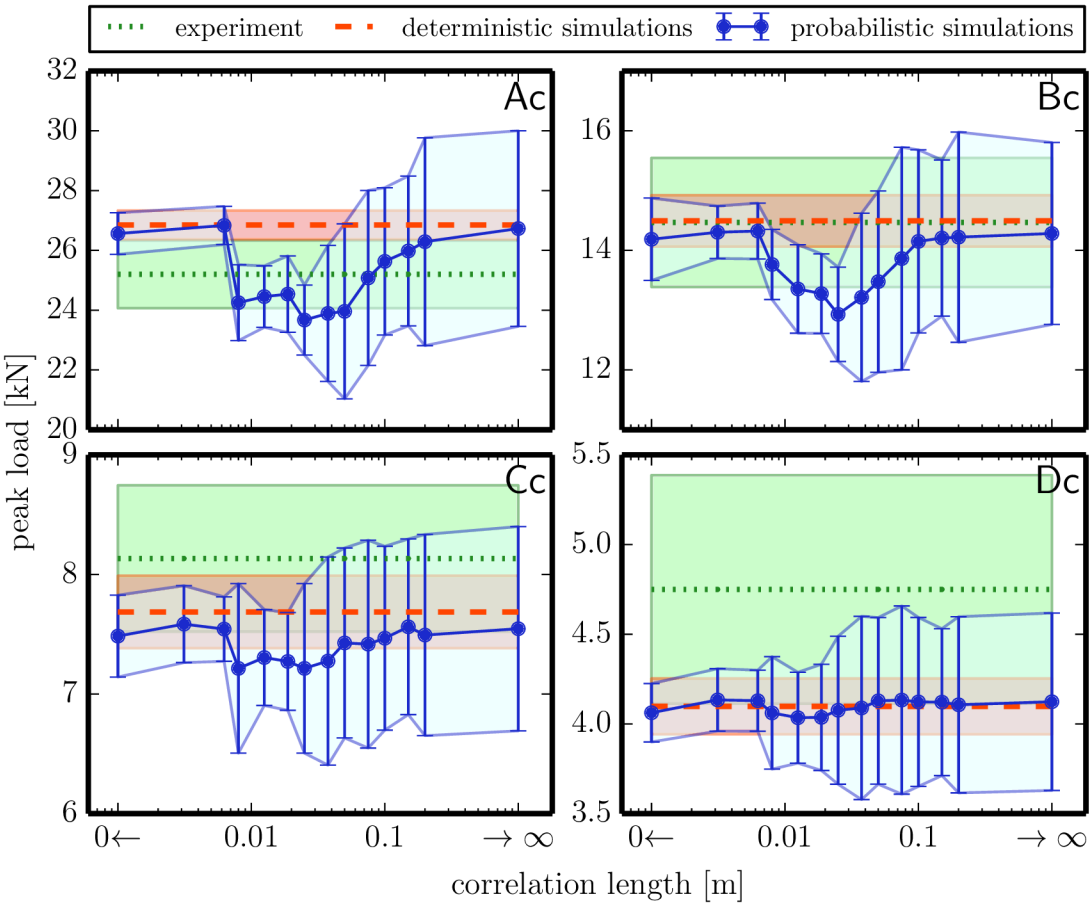

Fig. 5.1: Experimental (green), deterministic (red) and probabilistic (blue) peak load [kN] vs. correlation length [m] of the random field from simulations of all sizes of unnotched beams (groups Ac, Bc, Cc, Dc).

served that simulations with different values of l_c did not provide the same mean peak load. For the $l_c = 0$ and $l_c = \infty$, the mean of the probabilistic simulations and the mean of deterministic simulations are very close. The situation differs for $l_c \approx 0.025$ m where the decrease of the mean peak load can be observed, especially for the larger beams (Ac, Bc and Cc). The diagram for the smallest unnotched beams (group Dc) does not show such a dependency. This is caused by the fact that the damage zone is relatively large to the beam size so that the crack cannot choose the weaker spot along the beam. The behavior is similar to the beams with a notch where the crack location is dictated by a stress concentrator. Looking at the standard deviation of the peak load, we can observe an increasing trend with the increasing correlation length, whereas the values of the deterministic and probabilistic peak load for $l_c = 0$ are very close to each other.

The same probabilistic simulations were performed for deeply-notched beams of the second largest size (group Ba). The dependency of the mean peak load on the value of the correlation length is presented in Fig. 5.2. Contrary to the

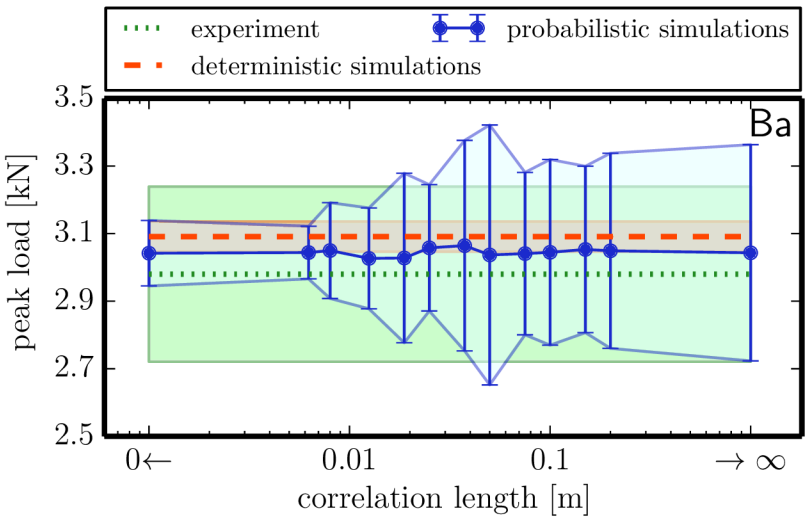

Fig. 5.2: Experimental (green), deterministic (red) and probabilistic (blue) peak load [kN] vs. correlation length [m] of the random field from simulations of the second largest size of deeply-notched beams (group Ba).

unnotched beams, the average peak load of the notched beams is not influenced by the correlation length l_c. The standard deviation of the peak load seems to be increasing with the value of l_c.

Surprisingly, the mean peak load from the probabilistic model did not reach the mean load of the deterministic model. This fact was caused by the scaling method used to sample the fracture energy. In these simulations, the linear scaling of fracture energy (referred in the following text as alternative I) was applied which results in nonlinear relation between strength of the probabilistic model with $l_c = \infty$ and the applied scaling factor h. More about the scaling methods is discussed in the following text.

5.2 Relationship between the tensile strength and fracture energy

Based on the lower average peak load of the probabilistic model compared to the deterministic one (see Fig. 5.2), the scaling method of the fracture energy was modified. Both types of scaling methods will be now compared and discussed. The probabilistic model has been studied in two alternatives. In the first alternative applied up to now, proportionality between the random field of local fracture energy, $G_t(\boldsymbol{x})$, and tensile strength, $f_t(\boldsymbol{x})$, was used while, in the second alternative, the relationship between $G_t(\boldsymbol{x})$ and $f_t(\boldsymbol{x})$ was nonlinear.

In both alternatives, the random field of local *tensile strength* is proportional to

$H(\boldsymbol{x})$ (Eq. 3.17)

$$f_{\mathrm{t}}(\boldsymbol{x}) = \overline{f_{\mathrm{t}}}\, H(\boldsymbol{x}) \tag{5.1}$$

In other words, the mean value of $f_{\mathrm{t}}(\boldsymbol{x})$ at any point is equal to $\overline{f_{\mathrm{t}}}$ (the value of tensile strength used in the deterministic model) which makes the probabilistic simulations somehow consistent with the deterministic simulations. The coefficient of variation of the tensile strength $f_{\mathrm{t}}(\boldsymbol{x})$ equals to CoV of the random field, 0.14. The two alternatives differ in a way the local fracture energy G_{t} is related to the random field $H(\boldsymbol{x})$.

In *alternative I*, the parameter of local fracture energy, G_{t}, is proportional to H and therefore also to f_{t} at any point

$$G_{\mathrm{t}}(\boldsymbol{x}) = \overline{G_{\mathrm{t}}}\, H(\boldsymbol{x}) \tag{5.2}$$

This linear scaling leads to a qualitative change in the constitutive law, see Fig. 5.3 top left. In particular, a facet associated with a higher value of random field tends to be more brittle (having shorter characteristic length) and vice-versa. As a consequence, the model becomes nonlinearly dependent on a random parameter h. Assume now a model of unnotched beams loaded in three-point bending (TPB beams) (see Chap. 4 and [39]) in which the strength parameter f_{t} of all facets is multiplied by a random variable h, i.e. infinite correlation length $l_{\mathrm{c}} = \infty$ of the random field. We calculated the peak loads on identical discrete mesostructures with a set of realization of h. The dashed curves in Fig. 5.3 right show that the peak loads are not linearly dependent on h. In particular, if $\overline{F}_{\max}$ is the mean value of peak load from the deterministic model, then using $h = \text{const.}$ does not result in peak load $h\overline{F}_{\max}$ (see Fig. 5.3 right).

In *alternative II*, the parameter of local fracture energy G_{t}, is scaled in order to preserve constant characteristic length l_{char} by Irwin [34] at all points/facets. The value of l_{char} is selected to match the value used in the deterministic simulations

$$l_{\mathrm{char}} = E\frac{G_{\mathrm{t}}(\boldsymbol{x})}{f_{\mathrm{t}}^2(\boldsymbol{x})} = E\frac{G_{\mathrm{t}}(\boldsymbol{x})}{\left[\overline{f_{\mathrm{t}}}H(\boldsymbol{x})\right]^2} \tag{5.3}$$

By solving this identity for $G_{\mathrm{t}}(\boldsymbol{x})$, the formulation of random spatial variability of the local fracture energy is obtained

$$G_{\mathrm{t}}(\boldsymbol{x}) = \overline{G_{\mathrm{t}}}\,[H(\boldsymbol{x})]^2 \tag{5.4}$$

In alternative II, the tensile strength remains a linear function of the random field H, but the fracture energy has quadratic dependence on H. Such a nonlinear relationship between f_{t} and G_{t} has the advantage of preserving the character of the material (ductility vs. brittleness, see Figure 5.3 left bottom). As a consequence,

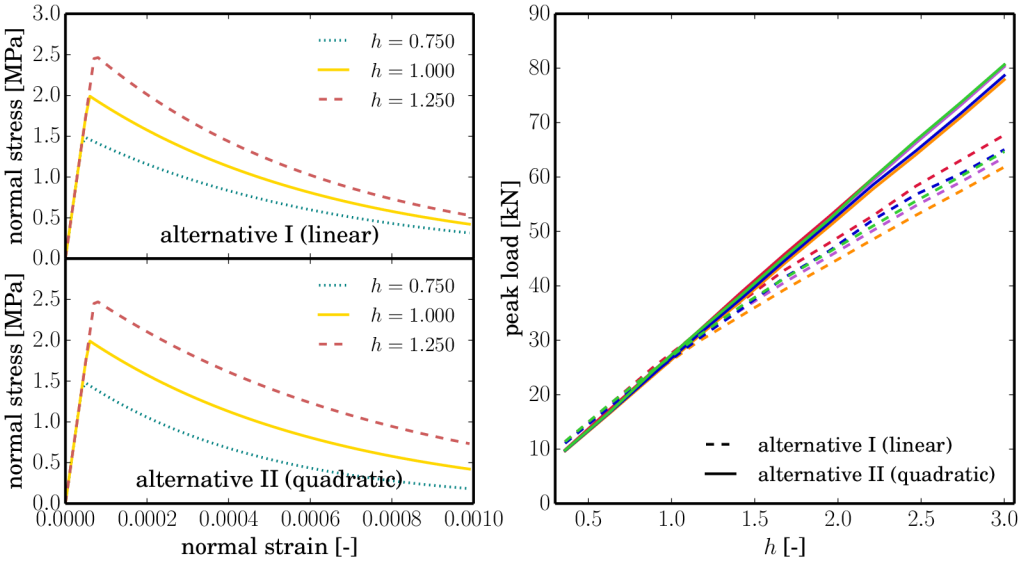

Fig. 5.3: Comparison of two alternatives for scaling of fracture energy G_t. Left: stress-strain relation of contact strained purely in normal direction when considering linear (alternative I) or quadratic (alternative II) dependency of G_t on random parameter h. Right: peak loads calculated with the probabilistic models of $l_\mathrm{c} = \infty$ using five different grain arrangements.

the peak loads of the whole structure are proportional to the value of h, see the solid lines in Fig. 5.3 right (individual curves are computed for various grain arrangements). Alternative II is preferable as it enables easier interpretation of the results. Therefore, in the further calculations, quadratic scaling of fracture energy (alternative II) is used. Except the proportionality, there is no other reason to select the alternative II (none of the alternatives is derived with help of experimental measurement).

It should be mentioned that the mean value of random fracture energy $G_\mathrm{t}(\boldsymbol{x})$ is not equal to $\overline{G_\mathrm{t}}$ in chosen alternative II. It is equal to $\overline{G_\mathrm{t}}$ times the mean value of h^2. The mean value of the squared Gaussian variable with the unit mean value and coefficient of variation of 14 % is equal to $1 + \mathrm{CoV}_h^2 = 1 + 0.14^2 = 1.0196$. Since the Weibull-Gauss distribution used is almost identical with Gaussian variable, the mean value of $G_\mathrm{t}(\boldsymbol{x})$ can be estimated as $1.0196 \cdot \overline{G_\mathrm{t}}$. The difference in the mean values of fracture energy of about 2 % from the deterministic simulations performed with $\overline{G_\mathrm{t}}$ is a price paid for the advantage of preserving the characteristic length.

The results presented in this chapter were presented at international conferences [40, 41].

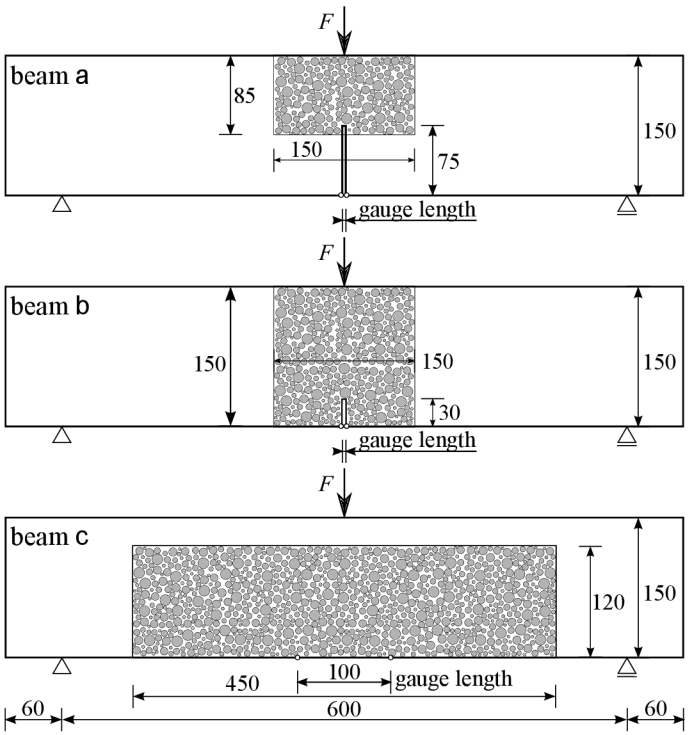

Fig. 5.4: Scheme of the new geometry: three types of beams: deeply-notched (top), shallowly-notched (middle) and unnotched (bottom). Thickness of all beam types was 40 mm.

5.3 New series of simulations

5.3.1 New geometry

To investigate the relation between the structural strength and the correlation length, a new (more convenient) geometry of the concrete beams is introduced. In this new simulation series, three types of beams are tested again: deeply-notched (half-notched, marked a), shallowly-notched (fifth-notched, marked b) and unnotched beams (marked c). The new geometry was more convenient for the bending simulations because of larger span-to-depth ratio. Less volume was simulated but span was sufficiently long to observe the effects of randomness: the beam length was 720 mm, the depth was 150 mm and the thickness 40 mm. The span between the supports (the bending span) was 600 mm, the notch in the midspan of the notched beams was 3 mm wide and 30 mm deep for shallowly-notched, resp. 75 mm deep for the deeply-notched beams. The region of the particle model was again reduced to the area where cracking is expected: the size of the region was 450 mm × 120 mm (length × depth) for the unnotched beams, 150 mm × 150 mm for the shallowly-notched beams and 150 mm × 75 mm for the deeply-notched beams. For the scheme of the geometry, see Fig. 5.4.

The model parameters have been adopted from the simulations of the bending experiments [27]. The procedure of parameter identification is closely described in Chap. 4. In these new simulations, the quadratic scaling providing the constant characteristic length from Eq. 5.3 was applied. The new beam geometry enabled to enlarge the number of the simulations for each correlation length of the random field due to the shorter time spent on each single simulation. In the new virtual experiment, 100 of unnotched and both notched beams were simulated for each value of l_c. The correlation length varied between zero and infinity and was considered in ten following values: $l_c \in \{0,\ 6.25,\ 12.5,\ 18.75,\ 25,\ 50,\ 100,\ 150,\ 200,\ \infty\} \cdot 10^{-3}\,\mathrm{m}$.

5.3.2 The correlation length study

Obtained dependency of the mean maximum load on the correlation length is plotted in Figs. 5.5, 5.6 and 5.7 for each notch type. The blue error-bars show the probabilistic models differing in l_c whereas the red line and the shaded areas show the mean ± one standard deviation calculated from the peak loads of 100 deterministic simulations. In the graphs, we can observe some common phenomena.

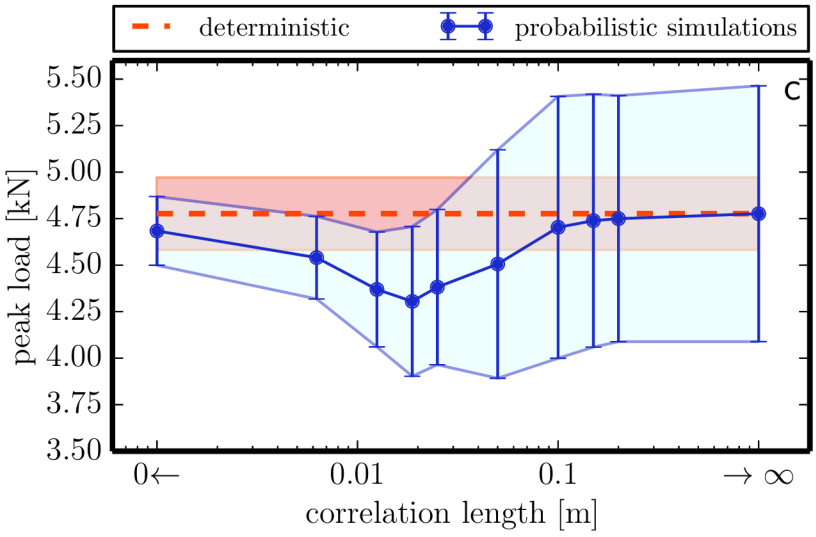

Fig. 5.5: Dependency of the maximum load on the correlation length l_c of the random field for unnotched beams (type C).

Let us focus on the right-hand part of the diagrams first: In the case of infinite correlation length, $l_c = \infty$, the dependence on a spatial coordinate $\boldsymbol{x}$ vanishes and the random field is defined by a single random variable, $H(\boldsymbol{x}) = h$. Therefore, the samples of the random field are random constants over the specimen domain. This case corresponds to the deterministic simulations with variable multiples of fracture parameters $f_t = \overline{f_t}h$ and $G_t = \overline{G_t}h^2$. The source of disorder in each simulation is then from the inner structure only.

Thanks to the quadratic scaling of G_t, the maximum load can be, for given inner structure, obtained as $F_{\max,p} = F_{\max,d}\, h$ where $F_{\max,d}$ is the peak load of the deterministic model. The inner structure disorder and the variability of the random parameter h are therefore separable.

For the unnotched beams (group c, Fig. 5.5), the mean value, standard deviation and coefficient of variation of the deterministic peak load are $\mu_d = \mathrm{E}[F_{\max,d}] = 4.78$ kN, $\sigma_d = \sqrt{\mathrm{D}[F_{\max,d}]} = 0.194$ and $\mathrm{CoV}_d = 0.041$, based on 100 simulations. The mean value and standard deviation of h are $\mu_h = 1$ and $\sigma_h = 0.14$. The inverse coefficients of variations can be noted as $\delta_d = 1/\mathrm{CoV}_d$ and $\delta_h = 1/\mathrm{CoV}_h$. Suppose now that both these variables are independent variables. To approximate the peak loads of probabilistic simulations with infinite correlation length, one can consider it to be a product of two random variables, $F_{\max,d}$ and h. Aroian (1947) [2] showed that such a product is asymptotically Gaussian if either δ_d or δ_h or both approach infinity. The mean value of such a product is $\mathrm{E}[F_{\max,p}] = \mu_d \cdot \mu_h = \mu_d \cdot 1 = \mu_d$. In other words, the mean value of probabilistic simulations matches the mean value of the deterministic simulations.

The variance of the product, however, reads

$$\mathrm{D}[F_{\max,p}] = \sigma_d^2\sigma_h^2 + \mu_d^2\sigma_h^2 + \mu_h^2\sigma_d^2 = \sigma_d^2\sigma_h^2(1 + \delta_d^2 + \delta_h^2) \tag{5.5}$$

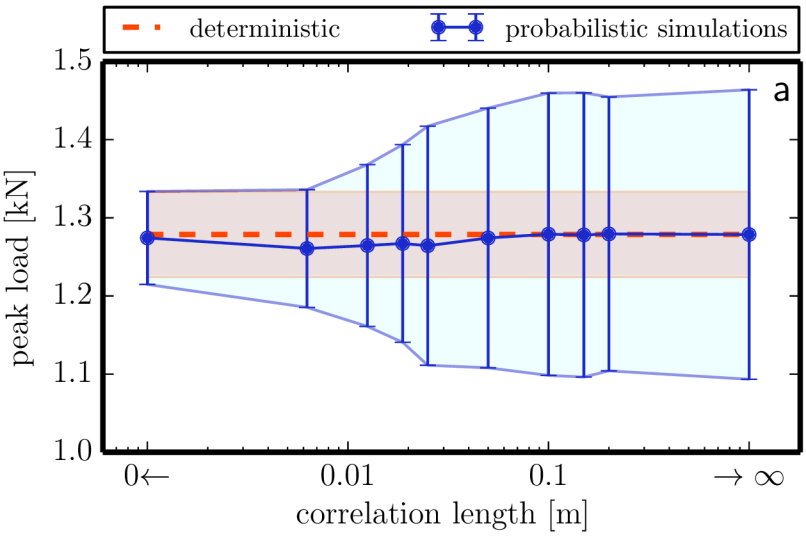

Fig. 5.6: Dependency of the maximum load on the correlation length l_c of the random field for deeply-notched beams (type a).

If both δ_d or δ_h are very small, the variance can be further simplified as

$$\mathrm{D}[F_{\max,p}] = \mu_d^2\sigma_h^2 + \mu_h^2\sigma_d^2 \tag{5.6}$$

The results of the probabilistic simulations on unnotched beams with $l_c = \infty$ yield $\mu_p = \mathrm{E}[F_{\max,p}] = 4.78$ kN and $\sigma_p = \sqrt{\mathrm{D}[F_{\max,p}]} = 0.687$ kN which gives

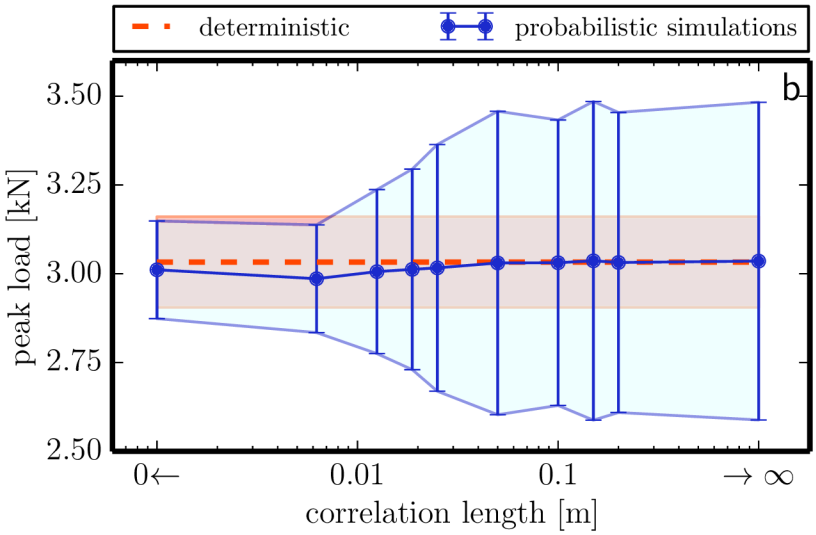

Fig. 5.7: Dependency of the maximum load on the correlation length l_c of the random field for fifth-notched beams (type b).

$\mathrm{CoV}_p = 0.144$. The deterministic and the probabilistic means are equal $\mu_d = \mu_p$, which is caused by the fact that the probabilistic simulation with $l_c = \infty$ corresponds to a deterministic simulation with a constant random field scaled by some factor. Looking at the standard deviations, the variance predicted by the Eqs. 5.5 and 5.6 are both equal $\sigma_{p,\mathrm{pred}} = \sqrt{\mathrm{D}[F_{\mathrm{max},p}]} = 0.696$ with corresponding coefficient of variation equal to $\mathrm{CoV}_{p,\mathrm{pred}} = 0.146$.

For the deeply-notched beams (group a, Fig. 5.6), the results of the deterministic simulations provided $\mu_d = \mathrm{E}[F_{\mathrm{max},d}] = 1.28$ kN, $\sigma_d = \sqrt{\mathrm{D}[F_{\mathrm{max},d}]} = 0.054$ and $\mathrm{CoV}_d = 0.042$ based on 100 simulations. The probabilistic simulations of the deeply-notched beams with $l_c = \infty$ yield $\mathrm{CoV}_p = 0.145$, with $\mu_p = 1.28$ kN and $\sigma_p = 0.185$. The variance predicted by Eq. 5.6 yields $\sigma_{p,\mathrm{pred}} = \sqrt{\mathrm{D}[F_{\mathrm{max},p}]} = 0.186$. Exploiting the fact that the mean values $\mu_p = \mu_d$, the prediction reads $\mathrm{CoV}_{p,\mathrm{pred}} = 0.146$.

The situation for shallowly-notched beams (group b) is quite similar to the deeply-notched beams. The dependency of the mean strength on the correlation length is in Fig. 5.7. A hundred of deterministic simulations resulted in $\mu_d = \mathrm{E}[F_{\mathrm{max},d}] = 3.03$ kN, $\sigma_d = \sqrt{\mathrm{D}[F_{\mathrm{max},d}]} = 0.13$ and $\mathrm{CoV}_d = 0.042$, while a hundred of probabilistic simulation with $l_c = \infty$ provided $\mu_p = 3.04$ kN, $\sigma_p = 0.45$ and $\mathrm{CoV}_p = 0.147$. The predicted coefficient of variation (Eq. 5.6) is $\mathrm{CoV}_{p,\mathrm{pred}} = 0.153$.

All mentioned statistics of the results of deterministic and probabilistic simulations with $l_c = \infty$ are overviewed in Tab. 5.1 as well as the CoV predicted by Eq. 5.6. In all cases, for notched and unnotched geometry, the predicted coefficients of variation closely correspond to the values obtained by the probabilistic simulations with infinite correlation length.

In the other limit, $l_c = 0$, the random field is just a theoretical construct. This

Tab. 5.1: Results of a hundred of deterministic and probabilistic simulations for $l_c = \infty$ (mean, standard deviation and coefficient of variation) plus predicted CoV.

	deterministic			probabilistic ($l_c = \infty$)			prediction (Eq. 5.6)
beam type	μ_d [kN]	σ_d [kN]	CoV_d [%]	μ_p [kN]	σ_p [kN]	CoV_p [%]	$\mathrm{CoV}_{p,\mathrm{pred}}$ [%]
a deeply-notched	1.28	0.05	4.24	1.28	0.19	14.49	14.57
b shallowly-notched	3.03	0.13	4.20	3.04	0.45	14.73	15.31
c unnotched	4.78	0.19	4.05	4.78	0.69	14.39	14.58

case is modeled by assigning each contact (facet) in the discrete model a random value of h independently of the surrounding contacts. Nevertheless, the mean and standard deviation from probabilistic simulations approximately equal to the mean and standard deviation from deterministic simulations. This can be observed for all three beams geometries (notched and unnotched beams) – see results in Tab. 5.2. The reason for such results are discussed further in the text.

For the values of the correlation length lying in between zero and infinity, notched and unnotched beams behave in a different manner: the notched beams do not show a sensitivity to the value of the correlation length of the random field and their probabilistic mean strength follow the value of the deterministic simulations. For the unnotched beams, some reduction of the probabilistic mean strength can be observed.

Tab. 5.2: Results of a hundred of probabilistic simulations for $l_c = 0$ and 0.025 m (mean, standard deviation and coefficient of variation).

	probabilistic ($l_c = 0$ m)			probabilistic ($l_c = 0.025$ m)		
beam type	μ_p [kN]	σ_p [kN]	CoV_p [%]	μ_p [kN]	σ_p [kN]	CoV_p [%]
a deeply-notched	1.27	0.06	4.67	1.26	0.15	12.10
b shallowly-notched	3.01	0.14	4.56	3.02	0.35	11.51
c unnotched	4.68	0.18	3.94	4.38	0.42	9.52

The results of probabilistic and deterministic simulations are also presented in Fig. 5.8 for deeply-notched beams and in Fig. 5.9 for unnotched beams. The shallowly-notched beams (b) are not presented any more as there is not a significant difference in behavior between them and the deeply-notched beams a. Only four selected cases are shown: the deterministic simulations (the first row) and the

Tab. 5.3: Ratio between the probabilistic and the deterministic peak load for each correlation length l_c.

	probabilistic mean / deterministic mean [%]									
beam	l_c [cm]									
type	0	0.625	1.25	1.875	2.5	5	10	15	20	∞
a	99.7	98.6	98.9	99.1	98.9	99.6	100.0	100.0	100.1	100.0
b	99.3	98.5	99.1	99.3	99.5	99.9	99.9	100.1	100.0	100.1
c	98.1	95.1	91.5	90.1	91.7	94.3	98.5	99.2	99.4	100.0

probabilistic simulations with l_c equal to ∞, 0.025 m and 0 (from the second to the fourth row). The remaining seven cases of the studied correlation lengths are omitted in these figures. The schematic representation of the fluctuation of the random variable h used in the corresponding simulations are depicted in the left columns of the figures. The middle column shows hundred $F - \mathrm{CMOD}$ (load – gauge opening) curves for each case. The error-bars in the right upper corner show the mean value and $\pm$ one standard deviation of the peak load for all four selected cases. For one curve from the plot, the response and the damage patterns at the maximum load and in the final step are shown in the right column.

By comparing the deterministic and the probabilistic simulations, it can be observed that the incorporation of the spatial variability in the parameters leads, for the beams with a notch, to an increase in variance of the peak load while the mean values remain unchanged. The reason for such a behavior is presence of the stress concentrator at the tip of the notch. The crack is forced to start from the notch and therefore the maximum load is dictated by the small volume of the material above the notch tip only. The amount of this critical volume is determined by the material internal length and it can be assumed approximately constant for any randomness applied (see the next chapter, Chap. 6). The shorter the correlation length, the more spatial fluctuations of material properties are present inside this volume. However, the crack initiating there has to (at least partially) damage most of the bonds inside that critical volume and the strength is dictated by almost all the values of h there. Some kind of averaging of these fluctuations is therefore present. The averaging inside the critical volume leads to the decrease in standard deviation of the peak load as the correlation length decreases. In the limit case of $l_c = 0$, the averaging is so strong that the standard deviation is about the same as in the deterministic simulations, i.e. the randomness due to spatial fluctuation completely diminishes; the variability in parameters due to random h is eclipsed by the effect of random orientation and size of the facets. The largest standard deviation is obtained for $l_c = \infty$, where the crack path is dictated by the mesostructure only and no ave-

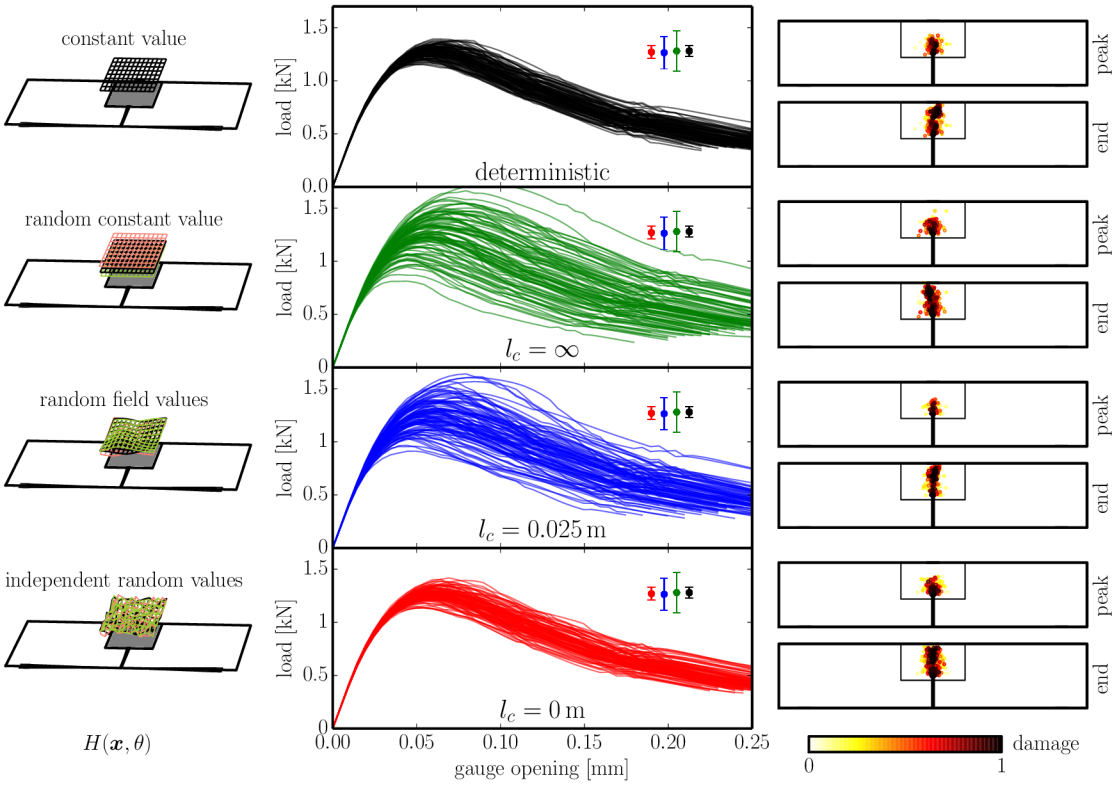

Fig. 5.8: Notched beams. Left: Schematic representation of spatial variability of $H(\boldsymbol{x})$. Middle: load – gauge opening curves for selected values of l_c. Right: Damage pattern at the peak load and at the end of one simulation.

riging takes place since no fluctuation of h exists. The strengths of the facets are all multiplied by a single value of h. The mean value is not changed because the average of h parameter in the critical volume for all the simulations together must have a mean value of 1 (since all of the contributing bonds have mean equal to 1) and the linear transformation between h and the model strength (alternative II in Fig. 5.3) ensures that the strengths are in mean value equal to the deterministic model.

For the unnotched beams, the situation is quite different. The absence of stress concentrator allows the cracks to choose where to initiate from and where the critical cluster of damage occurs. Therefore, such a critical volume can be selected anywhere along the bottom surface. It will naturally choose the worst combination of stress and strength. The strength is again given by averaging the fluctuations within the critical volume (and of course by the grain arrangement there). As the correlation length decreases, the rate of fluctuations increases and the probability that some weak area occurs and allows the crack to initiate increases as well. Therefore, the mean strength decreases with decreasing l_c. However, there is a limit dictated by the size of the critical volume. When the random field H starts to fluctuate inside the critical volume too much, the averaging effect leads to an increase in the strength of

the critical volume. The more fluctuations within the critical volume, the stronger the averaging. In a limit case of extremely small $l_c \to 0$, the randomness has no effect and the mean of the peak load should be equal to the mean peak load from the deterministic simulations. The standard deviation of the response has the same behavior as in the case of the notched beams; it decreases with the correlation length increase because of the increasing averaging effect. For the extreme of zero correlation length, the standard deviation is about the same as the one obtained with the deterministic model.

The interesting value of correlation length would be the one where the mean of the peak load reaches its minimum. In that case, the correlation length should be about the size of the critical volume. From our limited data, this value is around 0.025 mm.

5.4 Summary

In this chapter, a study of an influence of the correlation length dictating the rate of spatial fluctuation of the random field of f_t and G_t has been performed. The experimental data as well as a new numerical test series have been exploited to describe the dependency of the mean strength and its standard deviation. Some analytical relations were found as well. Apart from this, theoretical size of the critical volume of the area active around the crack tip has been derived.

Now, a closer look at the spatial distribution of the energy dissipation inside this active zone can be taken. The following chapter will deal with several attitudes how to evaluate and describe the active zone and its energy release.

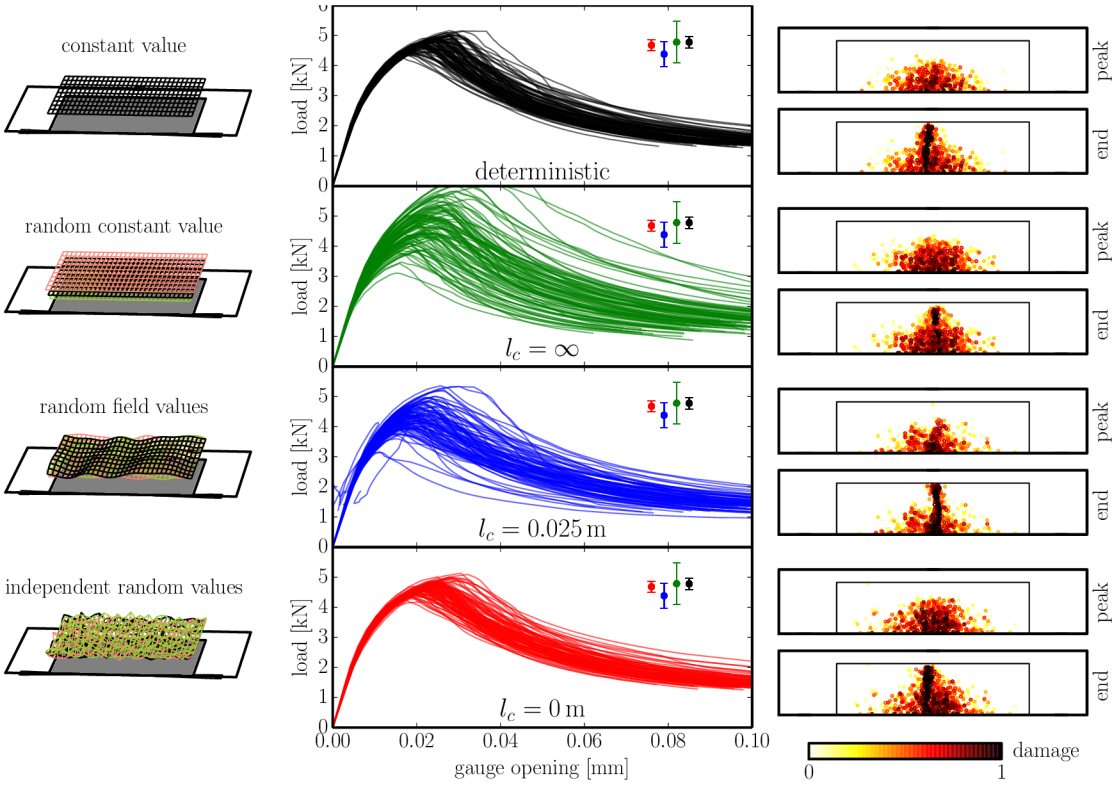

Fig. 5.9: Unnotched beams. Left: Schematic representation of spatial variability of $H(\boldsymbol{x})$. Middle: load – gauge opening curves for selected values of l_c. Right: Damage pattern at the peak load and at the end of one simulation.

6 SPATIAL DISTRIBUTION OF ENERGY DISSIPATION

This chapter is focused on the region created during the fracture process in the discrete model where the most of the damage and the energy release takes place. Such zone of the material is usually referred to as a fracture process zone (FPZ). The FPZ can be described as a zone where the damage localizes and the cracks start to interconnect, distribute and grow. Bažant [3] defines the FPZ as follows: *"The fracture process zone is a nonlinear zone characterized by progressive softening, for which the stress decreases at increasing deformation. This zone is surrounded by a nonsoftening nonlinear zone characterized by the hardening plasticity of perfect plasticity, for which the stress increases at increasing deformation or remains constant. Together these two zones form a nonlinear zone."*

The ability to provide information about the FPZ is limited to detailed meso-level models [24]. The meso-level discrete model used in this work enables tracing the process of formation and growth of the FPZ and subsequently also describing its size and shape in different phases of the loading. The FPZ also changes if we employ the spatial variability (the random field of strength and other parameters), as well as the test setup (notched and unnotched geometry) [20, 21].

The following text aims to describe the fracturing process via looking at difference in dissipated energy between subsequent solution steps. The zone that comprehends the energy dissipation difference will be called *the active zone*. The FPZ is usually understood as a cumulative zone with all fracture phenomena from the beginning of loading. The active zone shows fracturing activity in the specimen at a given time. Summation of the actives zone up to a given time is then the FPZ. The results of the analysis were presented at an international conference [17].

6.1 Data Processing

The data obtained during the virtual experiment on three-point bent beams was used to investigate the active zone. The same hundred simulations from previous chapter with the deterministic and probabilistic model (for every value of the correlation length of the random field) were used. The dissipated energy, $E_h^{(p)}$, released in an individual element

To process and evaluate the data from simulations, several strategies are used:

- applying a mesh grid and evaluating the information on each cell of the grid
- approximating the active zone shape with various geometrical shapes
- or using the outlier and novelty detection tool in Python

These procedures will be introduced now.

To represent the geometry with a stress concentrator, the deeply-notched geometry has been selected and the shallowly-notched beams are not presented any more as their performance did not show a significant difference from the deeply-notched beams. The geometry of the beams and the test setup can be found in Sec. 5.3.1.

6.1.1 Mesh Grid Procedure

To make an overall evaluation of the active zone over the set of simulations, it was necessary to put together the information from individual simulations. As the output data from simulations was defined for the particular facet (contact between particles) and each simulation has its own particles arrangement, the direct "summation" using coordinates is not possible. In the mesh grid method, the beam is divided into regular orthogonal grid with a defined cell size and each contact is assigned based on its coordinates to the appropriate grid cell. Then, the observed quantity is summed up inside each cell and the results can be presented. The mesh grid was considered as two-dimensional (each cell has the same thickness as the beam).

The results can be plotted for different phases of the loading (elastic regime, peak, postpeak). For the investigation of the active zone, we will focus now on the peak of the loading curve, when the beam is loaded by the maximum force. For this purpose, we are not interested in the total energy released from the beginning of the test till the peak load but only in the one time step when the peak load is reached. This allows us to investigate the rate of energy release at the peak load.

Therefore, the energy $\Delta E_h^{(i)}$ (Eq. 6.1) corresponding to solution step i was obtained by subtracting the dissipated energies at the end and at the beginning of ith step on each facet h – see Fig. 6.1. The solution step with the maximum force reached at its end will be referred to as the peak step and denoted p. The overall energy in the beam $\Delta E^{(p)} = \sum_h \Delta E_h^{(p)}$ released in this step is a sum of the energies released at all elements h in this step p.

$$\Delta E_h^{(p)} = E_h^{(p)} - E_h^{(p-1)} \tag{6.1}$$

To make statistical evaluation, we need to collect the information from individual simulations together. In the case of the notched beams, the situation is quite simple – the active zone develops above the notch tip which means the appropriate grid cells can be directly summed up together over the set of 100 simulations. In the case of the unnotched beams, the macro-crack can choose its location (due to the heterogeneous inner structure in the deterministic model plus additionally due to the random strength along the beam in the probabilistic model). Therefore, the

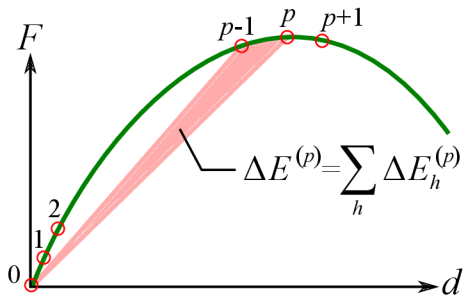

Fig. 6.1: Energy released in the solution step when the peak load is reached.

horizontal coordinates of the grid have to be shifted so that the individual macro-cracks overlap. The procedure of coordinate shifting was as follows: the final macro-crack has been found (from the final step) and its position (the x-coordinate of the centroid of total dissipation energy in a stripe of 50 mm depth above the bottom face) was set as the new x-coordinate origin. The horizontal location of the grid was updated with respect to the new origin.

As the length of the peak step differs for each simulation due to the adaptive step length solver, it was not suitable to combine directly the dissipated energies from individual simulations. To ensure equal contribution of each simulation, the relative energy, $\Delta \bar{E}^{(p)}$, is used – see Eqs. 6.2 and 6.3 (a ratio between the dissipated energy of the facet and the overall energy of the beam for an individual simulation).

$$\Delta \bar{E}_h^{(p)} = \frac{\Delta E_h^{(p)}}{\sum\limits_h \Delta E_h^{(p)}} \tag{6.2}$$

Then, the relative energy has been summed up over the volume of one cell b. Every grid cell b collects all the relative energy inside.

$$\Delta \bar{E}_b^{(p)} = \sum_{h \in b} \Delta \bar{E}_h^{(p)} \tag{6.3}$$

The relative energies divided into bins $\Delta \bar{E}_b^{(p)}$ have been summed up over the set of 100 simulations to get R_b – a summation of relative energy of corresponding cells over all simulations (Eq. 6.4) so that the general shape of the active zone can be seen.

$$R_b = \sum_{\text{sim}} \Delta \bar{E}_b^{(p)} \tag{6.4}$$

To compare the size of the active zone between the notched and the unnotched beams, the sum of relative energies R_b has been further normalized by its maximum – see Eq. 6.5. Then, the maximum value of the normalized relative energy $\bar{R}_b$ (in

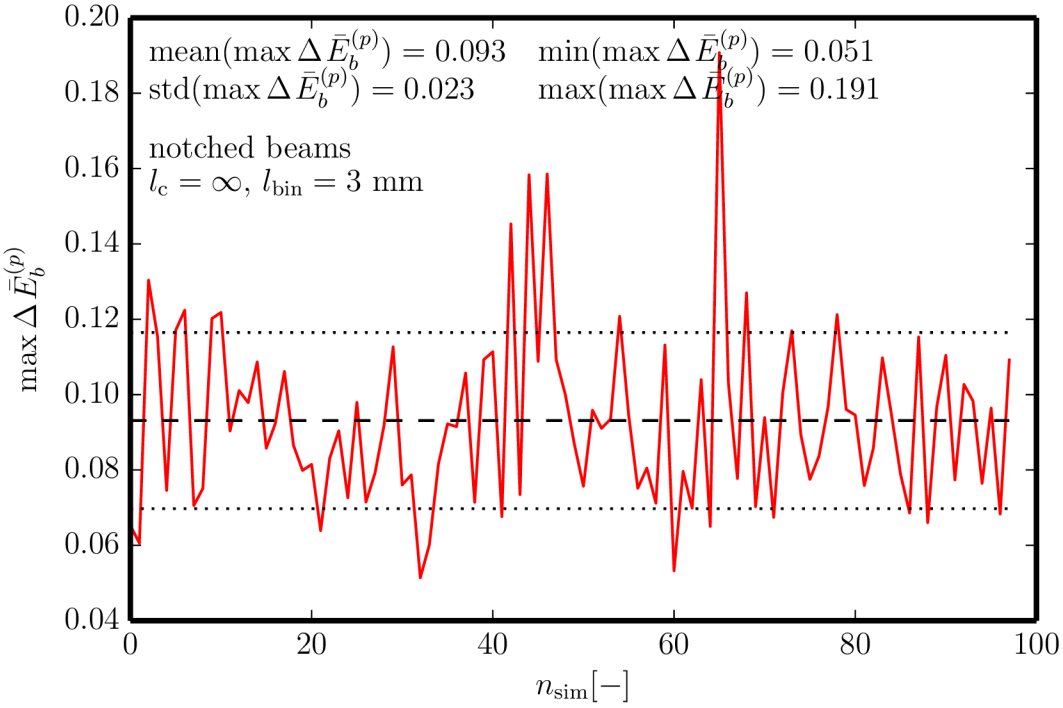

Fig. 6.2: Maximum of the dissipated relative energy on a mesh grid bin over the set of simulations.

the bin with the highest value) equals one, the values of the other bins are simply the ratio to the maximum value.

$$\bar{R}_b = \frac{R_b}{\max\limits_b (R_b)} \tag{6.5}$$

To check whether the dissipated energies of different simulations are not significantly different over the set of all simulations, the diagram from Fig. 6.2 is presented for the notched beams of correlation length $l_c = \infty$ and bin length $l_{bin} = 3$ mm. Regardless of the load, specimen size or boundary conditions, it is assumed that the material in the active zone dissipates approximately the same amount of relative energy. The maximum relative energy dissipated at the peak load in one bin, $\max \Delta \bar{E}_b^{(p)}$, is presented for all 100 simulations (Eq. 6.3 for the bin with the maximum dissipated energy). The observed values $\max \Delta \bar{E}_b^{(p)}$ of all 100 simulations are oscillating around the mean value with acceptable standard deviation although a few outlying values are present. The higher values of $\max \Delta \bar{E}_b^{(p)}$ of some simulations can be caused, e.g., by crack branching or locking. Both of these can cause that the energy released at the peak is higher for such simulation.

Results of the above mentioned approach are described further in Sec. 6.2.1.

6.1.2 Approximation of Active Zone by Geometrical Shapes

Another way how the shape of the active zone can be displayed is to find the geometrical shape which encloses as much of the specified quantity as possible (generally, it can be energy or damage but due to aforementioned reasons, relative energy difference, $\Delta \bar{E}_h^{(p)}$, was considered). In this procedure, a chosen geometrical shape of a small size was placed to the point of high stress concentration (the notch/crack tip) and then the energy dissipated inside the region was calculated. Different geometrical shapes were used: rectangle, half-ellipse and half-circle with different width-to-depth ratio (for unnotched beams) and ellipse and rectangle (for notched beams).

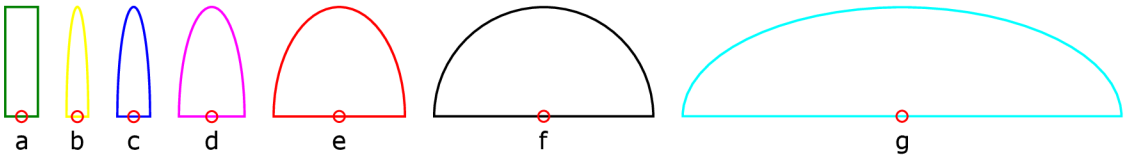

Fig. 6.3: Different geometrical shapes used for the approximation: scheme for unnotched beams.

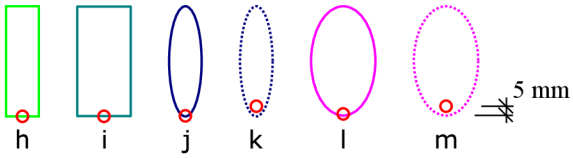

Fig. 6.4: Different geometrical shapes used for the approximation: scheme for notched beams.

The overview of the used geometrical shapes is in Fig. 6.3 for unnotched beams, in Fig. 6.4 for notched beams. Their geometry can be found in Tab. 6.1. Two types of ellipses were used to approximate the zone of the notched beams: bottom edge of the ellipse A is aligned with the notch tip while the ellipse B is shifted 5 mm downwards (it covers also a little area under the notch tip). The notch tip (in Fig. 6.4 for notched beams) resp. the macrocrack initiation point (in Fig. 6.3 for unnotched beams) is marked with a red circle.

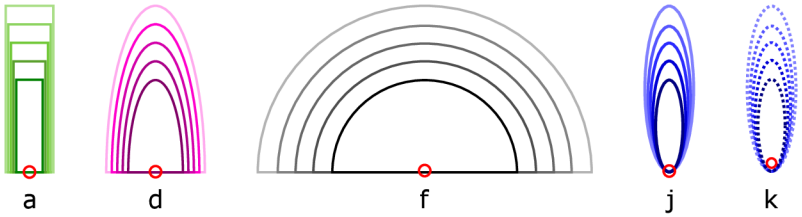

Fig. 6.5: Examples of scaling of the selected geometrical shapes.

Tab. 6.1: Different geometrical shapes used for the approximation.

unnotched beams			**notched beams**		
	shape	width : depth		shape	width : depth
a	rectangle	3 : 10	h	rectangle	3 : 10
b	half-ellipse	2 : 10	i	rectangle	5 : 10
c	half-ellipse	3 : 10	j	ellipse A	3 : 10
d	half-ellipse	6 : 10	k	ellipse B	3 : 10
e	half-ellipse	12 : 10	l	ellipse A	6 : 10
f	half-circle	20 : 10	m	ellipse B	6 : 10
g	half-ellipse	40 : 10			

Subsequently, the region was scaled (by a given constant) and the relative energy $\Delta \bar{E}_A^{(p)}$ inside the region A was summed up again, Eqs. 6.6. The sum of the overall relative energy is equal 1.

$$\Delta \bar{E}_A^{(p)} = \sum_{h \in A} \Delta \bar{E}_h^{(p)} \qquad \Delta \bar{E}^{(p)} = \sum_h \Delta \bar{E}_h^{(p)} = 1 \tag{6.6}$$

The scheme of scaling of the selected geometrical objects is in Fig. 6.5. Red circles mark the center of scaling of the object which was anchored to the notch tip/crack initiation position. The relation between the area of the object and the amount of the relative energy found inside the region was observed.

This approach shall reveal the geometrical shape which provides the best approximation of the active zone shape. The results of this type of approximation are presented in Sec. 6.2.2 for notched and unnotched beams.

6.1.3 Novelty Detection Tool

The third method used to find and describe the active zone at the top of the loading curve was the use of `scikit-learn` [50] (machine learning tool) in Python (built on NumPy, SciPy, and matplotlib). This package contains a simple and efficient tools for data mining and data analysis, it is open source, commercially usable (BSD license), and reusable in various contexts. We used the outlier and novelty detection procedure to find an area of the active zone where the most of the fracture energy releases during the peak step.

Description of the scikit-learn tool

"The `scikit-learn` *can be applied on various learning problems when there is, in general, a set of n samples of data and we try to predict properties of unknown data.*

If each sample is more than a single number and, for instance, a multi-dimensional entry, it is said to have several attributes or features. [51]

The function used in the process of observation of the active zone was the novelty and outlier detection routine which uses the unsupervised way of learning. *"Many applications require being able to decide whether a new observation belongs to the same distribution as existing observations (it is an inlier), or should be considered as different (it is an outlier). Often, this ability is used to clean real data sets. In the novelty detection method, the training data is not polluted by outliers, and we are interested in detecting anomalies in new observations, while in the outlier detection procedure the training data contains outliers, and we need to fit the central mode of the training data, ignoring the deviant observations. The used one-class SVM method (Support Vector Machines) is a novelty-detection method: its training set should not be contaminated by outliers as it may fit them.*

...In general, it is about to learn a rough, close frontier delimiting the contour of the initial observations distribution, plotted in embedding p-dimensional space. Then, if further observations lay within the frontier-delimited subspace, they are considered as coming from the same population than the initial observations. Otherwise, if they lay outside the frontier, we can say that they are abnormal with a given confidence in our assessment. The One-Class SVM has been introduced by Schölkopf et al. [53] *for that purpose and implemented in the Support Vector Machines module in the* `svm.OneClassSVM` *object. It requires the choice of a kernel and a scalar parameter to define a frontier. The RBF (radial basis function) kernel is usually chosen although there exists no exact formula or algorithm to set its bandwidth parameter. This is the default in the* `scikit-learn` *implementation. The ν parameter, also known as the margin of the One-Class SVM, corresponds to the probability of finding a new, but regular, observation outside the frontier."* [51]

Practically, we let the procedure find the best area with defined amount of the observed quantity (the relative dissipated energy).

If the ν parameter equals to 0.9, the procedure finds such an area for which a new observation occurs outside this area frontiers with 90 % probability. This implies that 10 % of all the relative dissipated energy is bordered by the area contour. The second free parameter γ is a coefficient for RBF, polynomial and sigmoid Kernel which influences the "coherence" of the found area. The lower the γ, the more compact the identified region. For unnotched beams the parameter was intuitively set to $\gamma = 0.01$ and for deeply-notched beams 0.005. The other parameters were left default, more about the function can be found online in [51].

The results of the novelty detection analysis of the active zone will be described in Sec. 6.2.3.

6.2 Evaluation of the Active Zone

The following section will introduce the main results of the three aforementioned methods of analyzing the active zone.

6.2.1 Mesh Grid Evaluation

This section presents the results of the analysis of the active zone by means of the mesh grid method. The beam was divided into bins using a regular orthogonal grid with size of 3 mm in x and y direction and the relative dissipated energy was summed up over these bins. To process the dissipated energy over the set of a hundred simulations and to be able to compare the active zones of notched and unnotched beams, the absolute dissipated energy was transformed into normalized relative dissipated energy. More about the mesh grid method and about the energy normalization is explained in Sec. 6.1.1.

Figure 6.6 shows the normalized dissipated energy $\bar{R}_b$ of the mesh grid bins on the three different probabilistic models of unnotched (left) and notched (right) beams. The exponential contour plot was applied in these figures. The relative dissipated energy R_b of each bin was normalized with respect to the bin with the highest value – the dark red color represents the bins with the highest relative dissipated energy while the dark blue corresponds the regions with energy below 1 % of the highest value. Three different correlation lengths were chosen for the figure: $l_c = 0$ (top), $l_c = 0.025$ m (middle) and $l_c = \infty$ (bottom plot).

Comparing the active zones of the notched and unnotched beams, it can be observed that, for unnotched beams, the region with a low energy dissipation ($\bar{R}_b \in \langle 1\%, 5\% \rangle$) is much larger than in case of the notched beams. The damage and energy release happen, in case of unnotched beams, in much larger portion of the beam. On the contrary, region of high energy dissipation is quite similar, both in size and shape. When comparing the active zone of different correlation lengths, it seems that there is no influence in notched case, but some in unnotched case.

The similar pattern of the dark red region of notched beams is probably caused by the fact that for each 100 simulations the same 100 inner arrangements of the particles have been used. Due to this, the peak of the active zone is shifted rightwards (the structure is statistically weaker on this site of the notch).

Such contour plots were calculated for each of the correlation length l_c. Three contours in elevation corresponding to approx. 20 % (solid line), 40 % (dash line) and 60 % (dotted line) of the maximum $\bar{R}_b$ are plotted in Fig. 6.7, both for unnotched beams (top) and notched beams (bottom). Top three diagrams always show the maximum width of the zone (left), its maximum depth (middle) and the square root

of the overall area (right) enclosed by the selected contour. The horizontal lines in these plots represent the results of corresponding deterministic model. From these diagrams, the dependence of the shape of the active zone on the correlation length of the random field can be clearly observed.

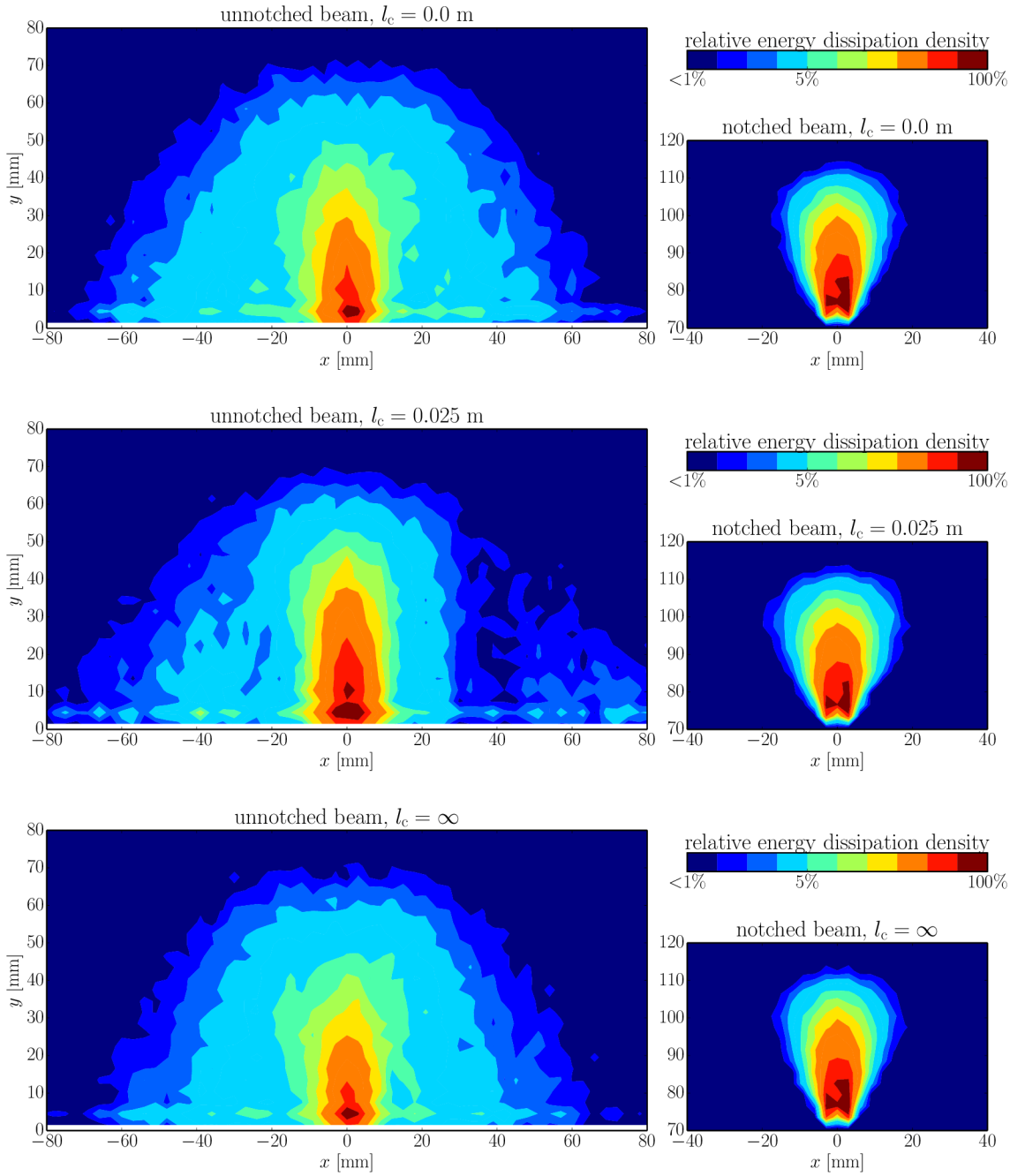

Fig. 6.6: Mesh grid evaluation of the active zone: contour plot of $\bar{R}_b$ (normalized relative dissipated energy) in bins for three different models.

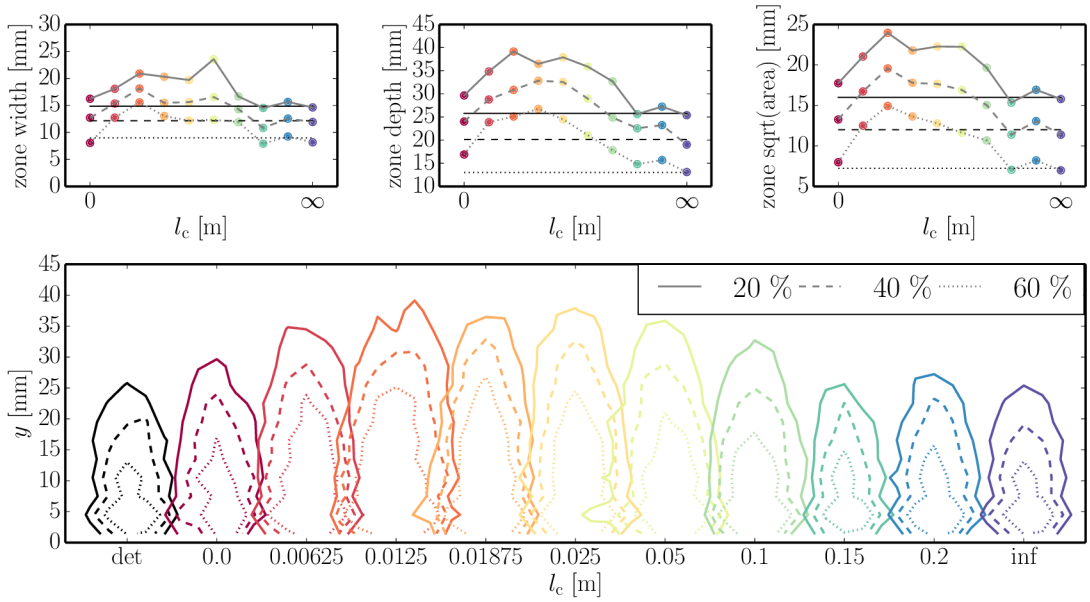

(a) Unnotched beams

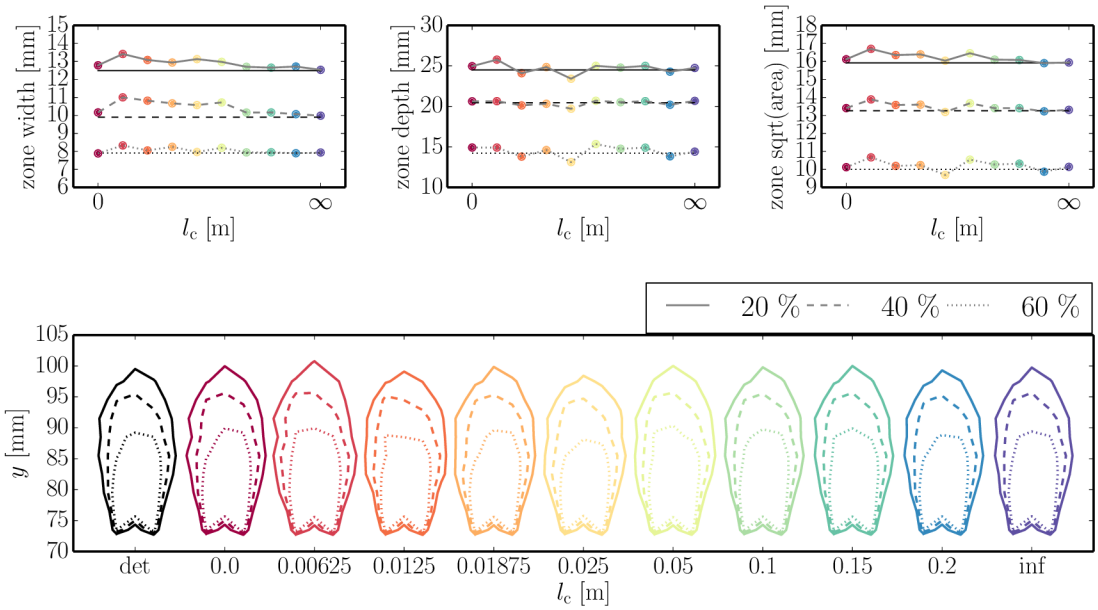

(b) Notched beams

Fig. 6.7: Mesh grid evaluation of the active zone: Three selected contours and their dependence on width, depth, area and shape on the correlation length.

Looking at the diagrams of the unnotched beams (Fig. 6.7a), a strong influence of the correlation length on the size of the active zone can be seen. For the value of $l_c = 0.0125$ m, the active zone reaches the largest area. With growing or reducing value of l_c, the zone gets smaller. In extremes ($l_c = \infty$ and $l_c = 0$), the zone has approximately the same size.

For the deeply-notched beams, the active zone seems to have no dependence on the random field and its correlation length. This is shown in all three top diagrams of Fig. 6.7b – the zone width, depth and area are constant over all the values of l_c.

The evolution of the active zone is illustrated in Fig. 6.8, again for both unnotched (left) and notched (right) beams simulated by the probabilistic model with $l_c = \infty$. The shape and size of the active zone is shown for different levels of the load – starting at 60 % of the maximum force going through the peak force (fifth row) to the postpeak at 60 % of the maximum force. The depicted states show the overall normalized relative dissipated energy, $\bar{R}_b$, released at the particular simulation step). The relative energy was summed up over the set of 100 simulations and again normalized by the bin with the maximum value.

The figure clearly demonstrates the difference of the evolution of the active zones in notched and unnotched beams. For the unnotched beams, the prepeak distribution of the released energy corresponds to the isolines of the main tensile stress in the beam. At the peak force, the zone localizes and further on, the energy is released mostly around the growing macrocrack. In the case of the notched beams, the zone is localized from the beginning above the stress concentrator (the notch) and grows during the loading (in the horizontal direction in the prepeak phase and in the vertical direction after the peak force is reached).

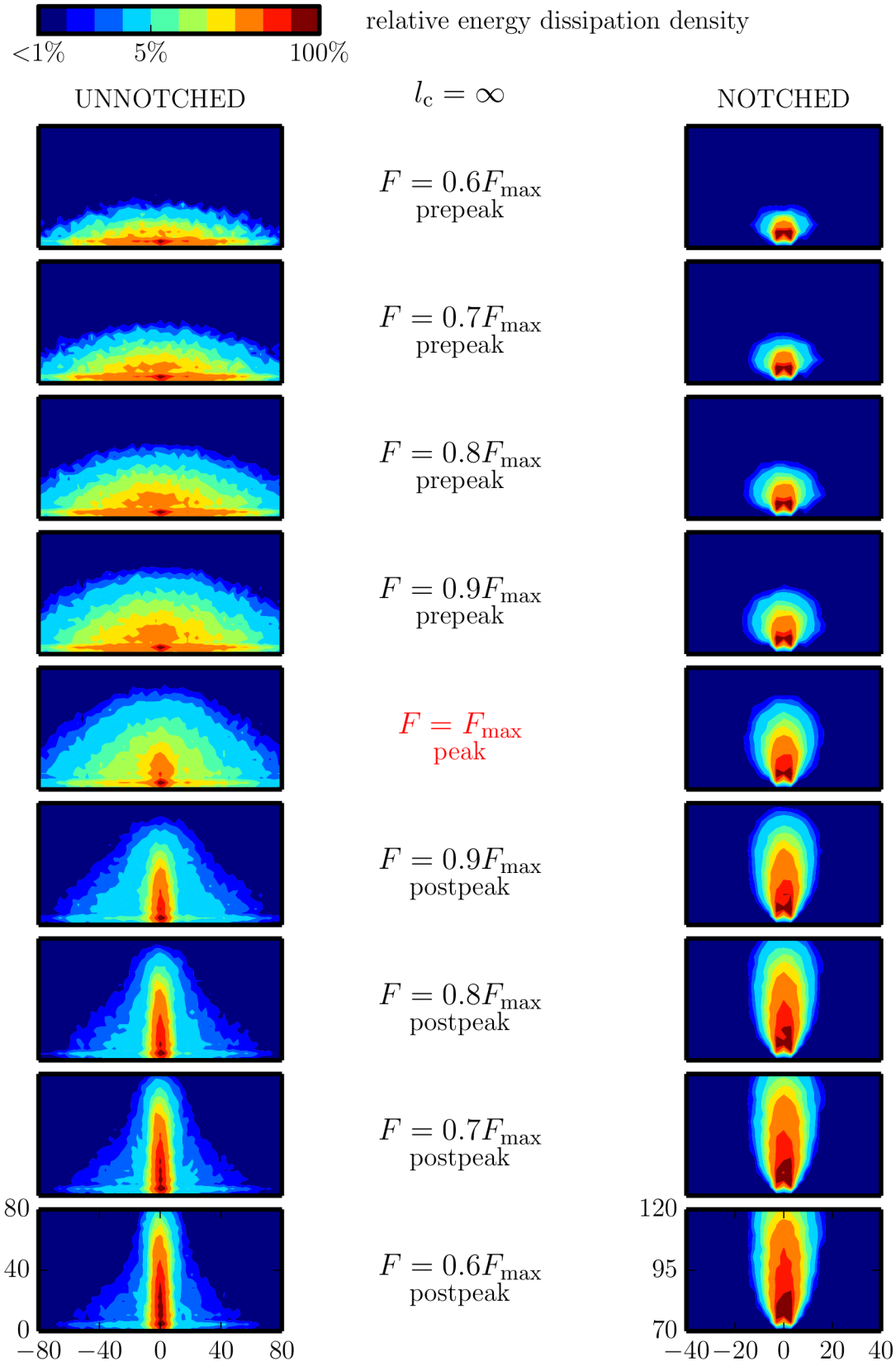

Fig. 6.8: An evolution of the active zone for notched and unnotched beams during the loading (results from 100 simulations, $l_c = \infty$).

6.2.2 Evaluation of the Geometrical Shapes Approximation

Results of the approximation method described in Sec. 6.1.2 will be presented now. In this approach, the active zone is approximated by chosen geometrical shape and the portion of the dissipated energy released at the peak step of the loading curve inside the region A, $\Delta\bar{E}_A^{(p)}$ (Eq. 6.6), is evaluated. The region is enlarged in steps, until a given threshold of the released energy portion is reached. The applied shapes are presented in Fig. 6.3 for unnotched beams and in Fig. 6.4 for notched beams.

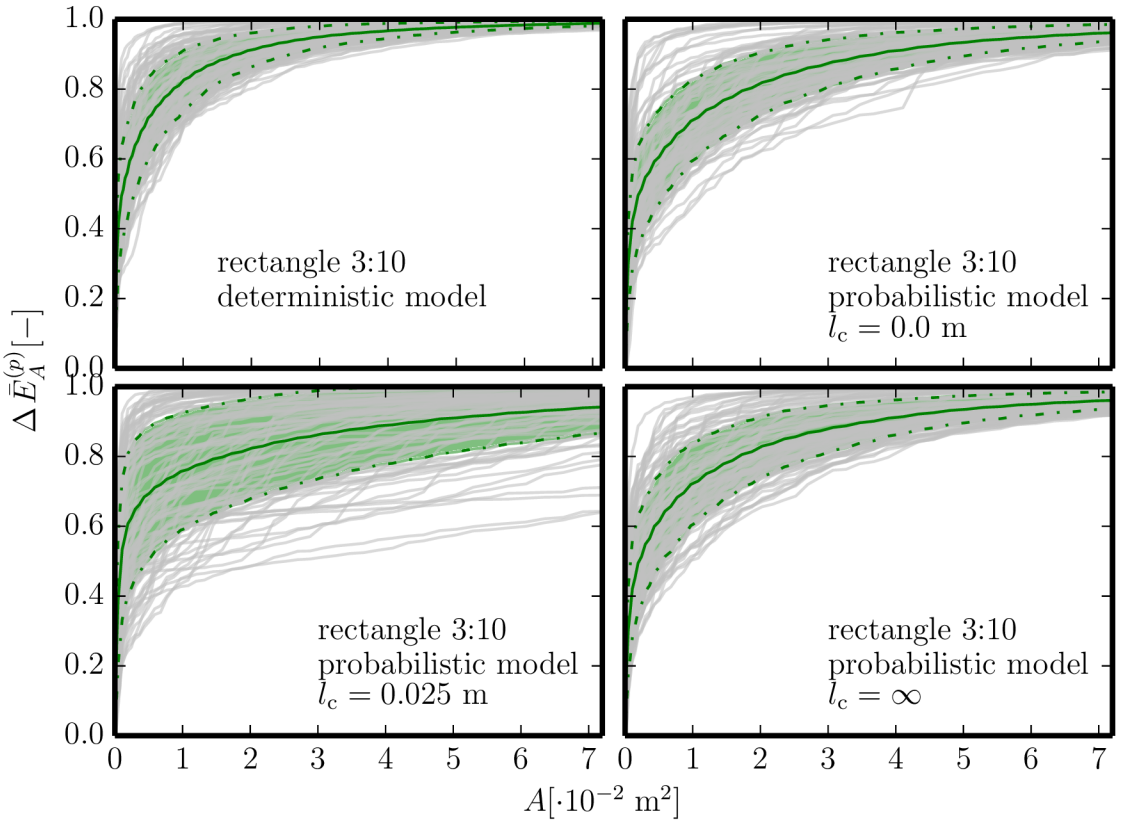

Fig. 6.9: Portion of relative the energy included in a rectangle region (shape a) vs. its area (unnotched beams).

In following graphs, the dependence of the portion of dissipated energy (the ratio between the energy inside the region defined by the geometrical shape $\Delta\bar{E}_A^{(p)}$ to the total released energy $\Delta\bar{E}^{(p)}$ over the whole beam) inside the region of area A is presented. Figure 6.9 provides an example of one of the used approximation shapes – the rectangle with a width-to-depth ratio of 3:10 (shape a). Four plots correspond to one deterministic model and three probabilistic models (with correlation lengths $l_c = \{0, 0.025, \infty\}$ m). Grey curves in the plot are the approximations from the individual simulations, green solid line marks the average curve plus/minus one standard deviation (dash-dot line and the green region in between).

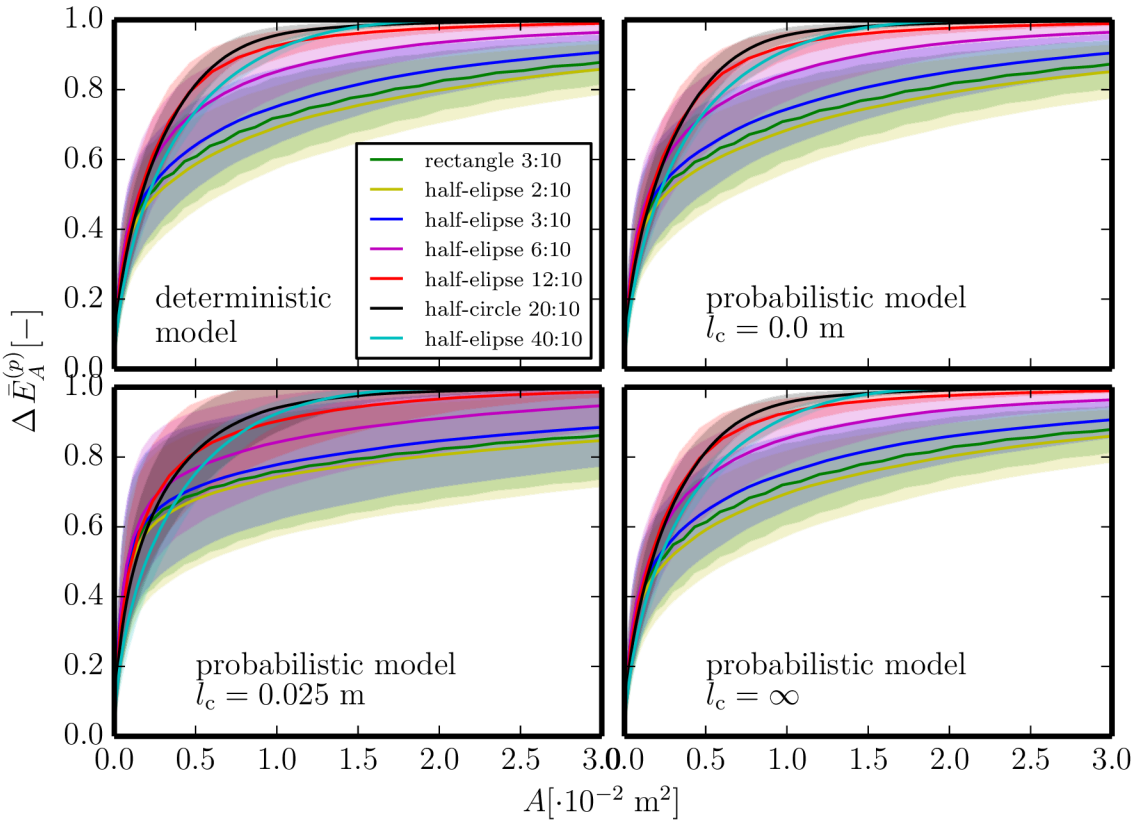

Fig. 6.10: Portion of the relative energy included in different geometrical shapes vs. their area (unnotched beams).

The average curve was found for each of the geometrical shape (see Tab. 6.1). These curves are presented in Fig. 6.10 for unnotched beams and in Fig. 6.11 for notched beams. Again, the results of the deterministic and three probabilistic models differing in their correlation lengths are plotted.

According to the assumption, the geometrical shape which reaches the certain level of $\Delta \bar{E}_A^{(p)}$ with the smallest area has the most optimal shape for the approximation of the active zone. If we look at the results, different shapes satisfy this assumption for different values of $\Delta \bar{E}_A^{(p)}$, nevertheless the results are similar for all four models.

Let us now focus on the results for the unnotched beams in Fig. 6.10. In the initial part of the diagrams, the purple curve corresponding to the half-elliptical shape (d) with width-to-depth ratio of 6:10 performs the best. It wins up to 50 % of the total energy (for the probabilistic model with $l_c = 0.025$ m it is even till about 70 %). At that point, the wider shape of the red half-ellipse 12:10 (e) starts to be more convenient till about 80 % of the overall released energy of all simulations $E_{\mathrm{tot}} = \sum_{\mathrm{sim}} \sum_h \Delta E_h^{(p)}$ (for the probabilistic model with $l_c = 0$ about 70 %). Above this level, the black curve of the half-circle (f) 20:10 becomes the top one till the

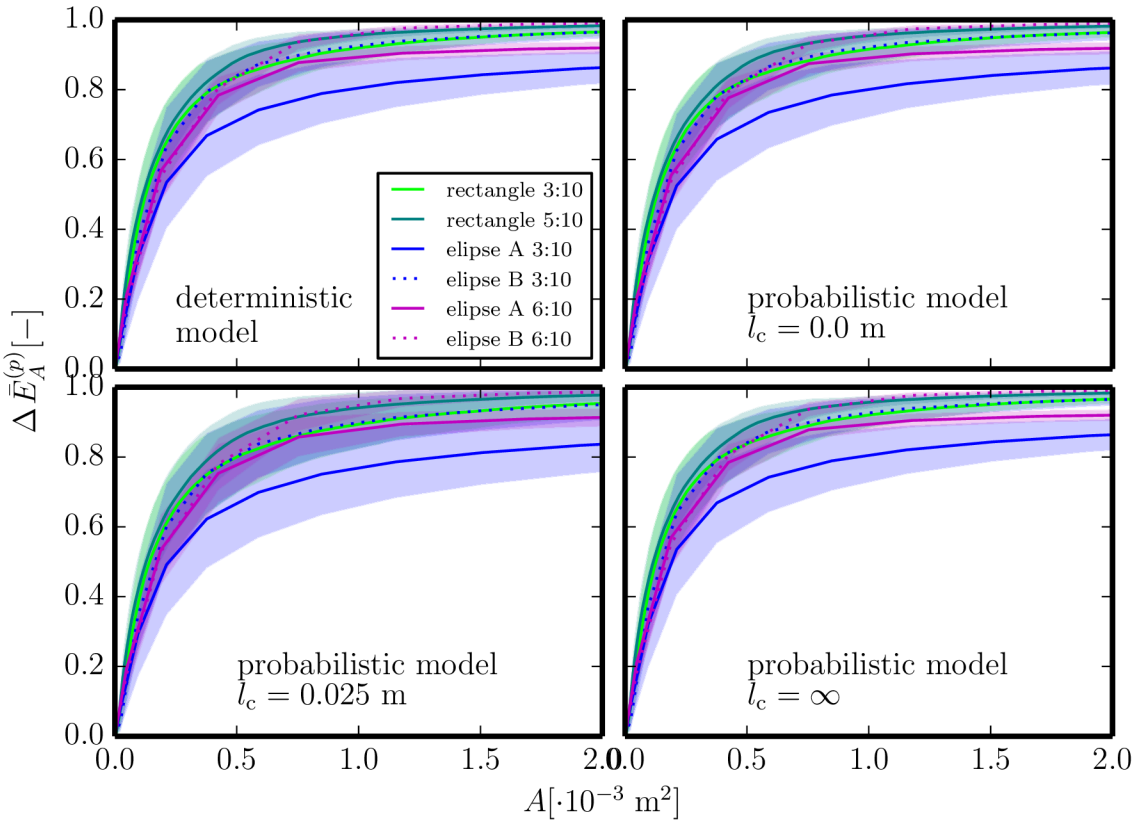

Fig. 6.11: Portion of included relative energy in different geometrical shapes vs. their area (notched beams).

very last part (about 98 %). The remaining 2 % of the total energy are again in some wider region, therefore the widest cyan half-ellipse (g) 40:10 works the best in the final stage around 100 % of the overall $\Delta \bar{E}^{(p)}$.

For the notched beams, the most convenient shape seems to be the rectangle (i) with width-to-depth ratio of 5:10 which is marked with the dark green color. For all four models, this shape is the best approximation till the threshold of about 95 % of the total energy. Above this limit, the wider ellipse B 6:10 (m) that was shifted 5 mm downwards from the notch tip seems to approximate the shape of the active zone the best.

Based on this study, it can be concluded that the shape of the active zone (seen as a function of the released energy in the region of the notch/crack) does not have the equidistant contour lines. The central part of the active zone is approximated the best by some more narrow shape (rectangle 5:10 for notched and half-ellipse 6:10 for unnotched beams) and it becomes wider as we go further from the tip (the most distant contour line is close to ellipse 6:10 for notched and to half-ellipse 40:10 for unnotched beams).

6.2.3 Novelty Detection Evaluation

Similarly to the previous two methods, one hundred simulations of the notched and unnotched beams were combined together again and the relative energy dissipated at the peak step was observed. The x-coordinates of the unnotched beams were shifted so that their active zones overlap. Then, the outlier/novelty detection tool was employed to find the region with the highest density of the dissipated energy. The procedure has been described in Sec. 6.1.3.

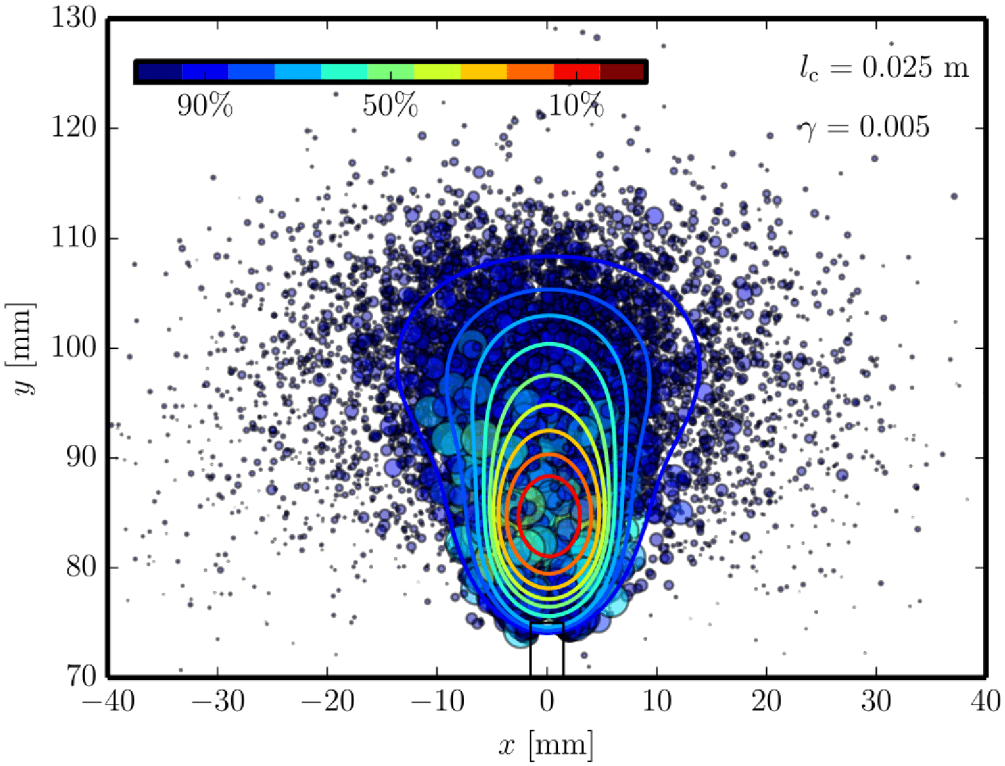

Fig. 6.12: Notched beams: Relative energy dissipated at individual contacts and border contours specifying the amount of the dissipated energy (outlier and novelty detection tool).

Figures 6.12 and 6.13 show two results of the analysis by the novelty detection tool in Python. Only one example of deeply-notched and unnotched beams is presented – simulations by probabilistic model with the correlation length of $l_c = 0.025$ m. The background of the figures is composed of color circles of different sizes which show the relative energy released at each facet of the model (for the sake of lucidity of the figure, only 30 simulations are plotted). The bigger the circle and the lighter the color, the more relative energy dissipated at the facet. The color contours are plotted over it. They correspond to the particular amount of overall dissipated energy inside the area bordered by the contour, e.g. the red line limits

the area where 10 % of the dissipated energy has been released. These plots are the result of the novelty detection analysis of all 100 simulations with each model.

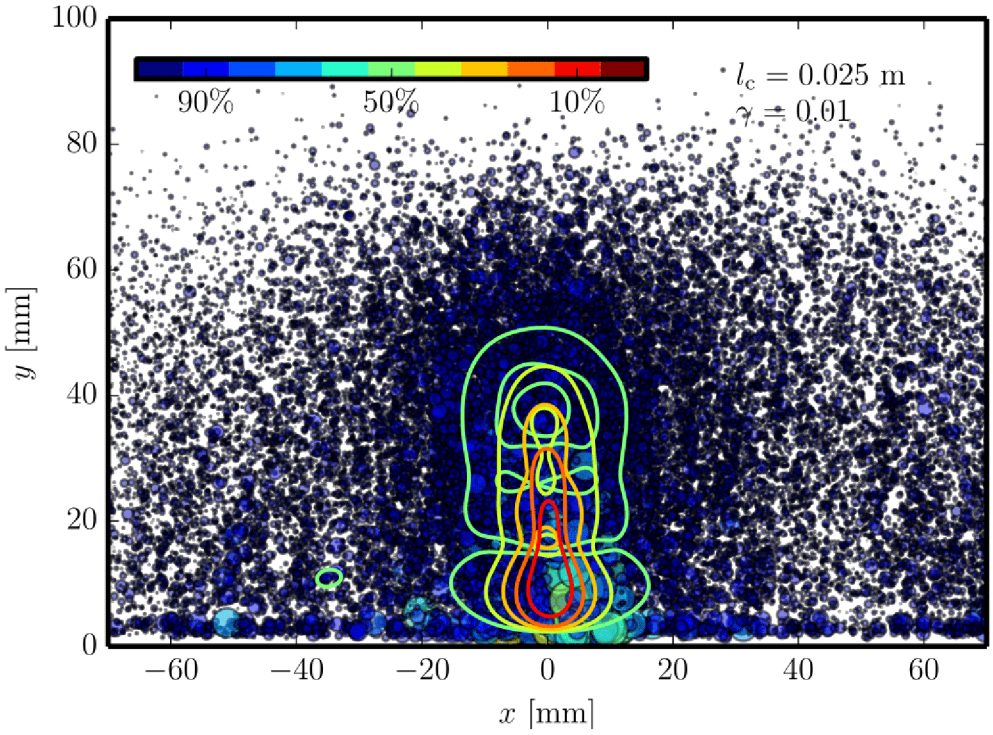

Fig. 6.13: Unnotched beams: Relative energy dissipated at individual contacts and border contours specifying the amount of the dissipated energy (outlier and novelty detection tool).

For the notched beams (Fig. 6.12), the active zone is concentrated within a relatively small area above the stress concentrator (the notch). Therefore, the Python tool was able to find all the contours from 10 % (red line) up to 90 % (dark blue line) and they are still close to the notch tip and have a simple shape. On the contrary for the unnotched beams (Fig. 6.13) only some contours were evaluated (from 10 to 50 %). The active zone here is spread into a larger area around the final crack position as visible from the blue circles in the figure background. However, the most of the energy is released in a small region around the macrocrack location and is bordered by the red line in the figure. The turquoise contour corresponding to the 50 % of the overall dissipated energy already defines an area which is not compact any more, even if the higher coefficient γ is used in the computation. For the higher contours (above fifty procent), the outlier and novelty detection tool is not able to find a region that would be compact but is divided into several regions. Due to this reason, the higher contours are not plotted in the figure.

If we focus now on the shape of the active zone defined by the calculated contours,

we can see that for the notched beams, it changes from an oval shape bordering the center of the active zone (red curve) to an upturned pear shape (the dark blue line) of the zone with almost all the dissipated energy. The region with the 50 % of the overall dissipated energy is about 10 mm wide and 22 mm deep (turquoise line). For the unnotched beams, the zone looks quite different: the red contour is pear shaped and the zone grows more in the vertical direction (the contours up to 40 % are elongated), the last plotted contour shows that the zone would have further on an oblong shape. The 50% contour has approx. 35 mm in width and 45 mm in depth.

6.3 Summary

This chapter was focused on the visualization and a description of the active zone (the region where the energy release takes place) which develops during the loading. Three different approaches were used to process the results of 100 simulations calculated with different models (one deterministic and ten probabilistic models differing it their value of the correlation length between zero and infinity): (i) applying a mesh grid and evaluating the information on each cell of the grid, (ii) approximating the active zone with different geometrical shapes or (iii) using the "outlier and novelty detection" tool in Python.

In the first procedure, the dissipated energy has been summed up inside each bin of a regular orthogonal mesh grid. As a result, the active zone could be visualized and investigated. The influence of the correlation length l_c of the random field on both the notched and the unnotched beams could be observed. For the unnotched beams, the active zone grows for the l_c increasing from zero to a certain value (about 12.5 mm). Behind this point, towards the infinite value of l_c, the active zone shrinks again. This phenomenon can be explained as follows: once the size of the region with a lower local strength (defined by the rate of fluctuation of the random field) matches certain volume of concrete that dictates strength of the whole structure, the active zone reaches its maximum size. On the other hand, the local strength does not play important role when investigating the notched beams, as the crack path is pre-defined by the deep notch. This caused the equal size of the active zones for any value of the correlation length.

The second method of investigation – the approximation of the active zone by different geometrical shapes tried to find a shape which approximates well the region of the active zone. Results showed that the shape of the active zone is different in different distances from the crack tip. Again, the results have to be commented separately for each of the beam geometry. For the unnotched beams, where there is no stress concentrator, the most of the relative dissipated energy (between 50 and

70 %) is released in a more narrow region – the best approximation shape was the half-ellipse 6:10 (width:depth ratio). The rest of the dissipated energy is distributed in a wider region, therefore, the half-elliptic shape 12:10 till about 80 %, resp. half-circle shape 20:10 further on till about 98 % of the overall released energy were the best approximation shapes. In case of the deeply-notched beams, the rectangle 5:10 embraced the released relative energy the best till about 95 %. Over this level, the elliptic shape 6:10 with 5 mm shift downwards won over the other shapes. Based on these, we can imagine that the most of the energy is released in a quite narrow region above the notch tip and the small complementary part of the overall energy is released further on sides.

The results from the third method are the most debatable, as the Python algorithm is not a clearly understandable procedure. The active zone plotted for the unnotched beams is with its size and shape comparable with the results from the mesh-grid analysis. Nevertheless, for the notched beams, the zone with the most intensive energy release is shifted upwards from the notch tip, which seems to be not correct. Also the value of the parameter γ influences the results of the analysis and its value was only roughly estimated.

7 CONCLUSION

The presented thesis aimed to validate an advanced numerical model of concrete and to investigate and describe, with the help of the validated model, the fracture process inside the concrete members subjected to mechanical loading.

The discrete model was adapted and extended with the spatial variability of parameters in form of random field. The model in its basic and extended form was validated based on the experimental results on beams of different size and configuration of the stress concentrator loaded in three-point bending test.

Two versions of the model were used: the basic (deterministic) one with the random arrangement of the particles representing the random inner structure of the material and the extended (probabilistic) one introducing an additional source of variability into the model – the random material parameters defined in form of the random field. Such an extension aims to improve the response of the model regarding its variability so that it better corresponds to the real data measured in the laboratory. For the deterministic model, the elementary static and kinematic relations are introduced as well as the procedure of generation of the topology of the model. For the probabilistic model, the process of generation of the random fields is briefly described.

The parameters of the introduced versions of the model are identified based on the laboratory experiments from literature. Three different test setups of bended beams were tested (deeply-notched, shallowly-notched and unnotched beams) in four different sizes. The data measured in such a wide experimental set were exploited both for the process of identification of the model parameters and for the subsequent validation of the model performance. In the first step of identification, the parameters of the deterministic model were found. The elastic modulus, Poisson's ratio, tensile strength and fracture energy in tension were identified directly based on the experiments. The other eight parameters were either calculated from recommended relations to the identified parameters or their value was adopted from literature. In the second step of identification, the probabilistic parameters were found (coefficient of variation based on the experiments and the other tree independent parameters according to literature). The correlation length was roughly estimated in this phase of the study. Four model parameters were considered to be randomly varying according to single random field: the tensile and shear strength and the fracture energy in tension and in shear. Both deterministic and probabilistic models were validated by simulating the experiments with a good agreement. The statistical size effect was observed on the measured data.

With the validated model, a wide series of numerical experiments was simulated. The influence of the correlation length on the peak load of the probabilistic model

was studied. A new series of simulations was designed with a focus on its convenience for the study of the mentioned dependence. Again, three different setups (deeply-notched, shallowly-notched and unnotched beams) were loaded in three-point bending test. The response was simulated in the same manner: with the deterministic model and also with the probabilistic one with ten different values of the correlation length (varying between zero and infinity). For each setup, a hundred different beams (differing in the arrangement of the inner structure) was virtually tested to obtain the results with a statistical significance.

The results of the new series revealed the following phenomenon: regarding unnotched beams, the strength evinces a drop around a certain value of the correlation length. For a given setup, the value was around 19 mm. In such case, the zone of the lower random local strength corresponds approximately to the size of the zone that has to be damaged so that the overall failure happens. If the correlation length is changed towards lower values (zero) or higher values (infinity), the mean probabilistic strength matches again the deterministic value. This can be explained by the fact the for the infinitely high value of correlation length, the random field has a constant value in all its points. This value is different for each simulation, however, their average corresponds to the value of the deterministic model. On the other hand, a random field with a zero correlation length has a different value in each of its point. To reach the failure, it is necessary that the material is damaged in a certain volume and the different local point values are again averaged in this region. Therefore, the deterministic average is reached again.

For the notched beam setup (deeply as well as shallowly), such trend is not observed. In this case, the path of the crack is more or less known in advance as it is dictated by the notch. Therefore, the local strength at the top of the notch tip does not play an important role and the average peak strength can be considered as equal for any correlation length of the random field (although, a slight drop can be observed for values around $l_c = 6$ mm.)

Finally, the thesis describes the energy release and the region in which it takes place. Three different approaches were suggested, evaluated and compared. In the first one, the beam was spatially divided into regular orthogonal grid and the released energy was summed up over the facets in each particular cell of the grid. The energy was normalized with respect to the different length of the peak step of each simulation so that the simulations can be statistically evaluated together. For the peak step, the region with the concentrated energy release was plotted for different values of correlation length. Again, differences between notched and unnotched beams were noticeable. The size of the active region in unnotched beam depended on the value of l_c. The largest region was reached for $l_c = 12.5$ mm. For this value of l_c, the 60 % of the overall energy at the peak was released in a region

of about 20×40 mm over the crack. In case of notched beam, the size of the region was about 13×25 mm and it was not sensitive to change of the correlation length. The evolution of the zone in which the energy is released during the whole bending test was also presented for both beam types.

In the second suggested method, the zone active during the testing was approximated with different geometrical shapes (rectangles, ellipses, half-ellipses, half-circles) so that the region can be described in terms of its shape. Each chosen shape was centered to cover the active zone, its size was increased in steps and the relative energy inside the region defined by given shape was summed up. It showed up that the active zone does not have a shape with equidistant contours but different shapes matches with the contours in different distances from the crack tip. Regarding the unnotched beams, the shape changes from half-ellipse 6:10 through half-ellipse 12:10 to half circle (the zone gets wider from its peak to its bottom). For the deeply-notched beams, the most convenient shape seemed to be a rectangle 5:10 changing in the end to wider shape of ellipse 6:10.

For the last method of describing the active zone with the highest energy release, the `scikit-learn` package (based on machine learning procedure) implemented in Python was employed. The Novelty detection tool looks for the region corresponding to the most intensive occurrence of target event (in our case the released fracture energy). This method also showed the difference between notched and unnotched beams: 90 % of the fracture energy of the notched beams released at the peak are concentrated within the zone which is about 20 mm wide and 35 mm deep. For the unnotched beams, the released energy is spread in a wider distance from the crack tip. The contour enclosing 50 % of the released energy was about 35 mm wide and 45 mm deep.

The above mentioned results gave more detailed insight into the shape and size of the region with the intensive energy release (active zone) as well as its development during the loading. The zone is not constant but its shape and size depend on the phase during the test and also they are influenced by other factors: the geometrical setup of the specimen (notched/unnotched configuration) or the rate of spatial fluctuation of the material parameters.

In the presented thesis, the performance of the enhanced numerical model was examined. It can be concluded that such approach of modeling of heterogeneous materials is a convenient way to gain a detail information about the creation and development of cracks inside the material. It is a well-established method of modeling with a high potential for the future. The thesis provided new knowledge about the zone active at the peak load which is the region that decides about the overall bearing capacity of the concrete member.

BIBLIOGRAPHY

[1] Alnaggar, M.; Cusatis, G.; Luzio, G. D.: Lattice Discrete Particle Modeling (LDPM) of Alkali Silica Reaction (ASR) deterioration of concrete structures. *Cement and Concrete Composites*, volume 41, 2013: pages 45 – 59, ISSN 0958-9465.

[2] Aroian, L. A.: The Probability Function of the Product of Two Normally Distributed Variables. *The Annals of Mathematical Statistics*, volume 18, nr. 2, 1947: pages 265–271.

[3] Bažant, Z.; Planas, J.: *Fracture and Size Effect in Concrete and Other Quasibrittle Materials*. New Directions in Civil Engineering, Taylor & Francis, 1997, ISBN 9780849382840.

[4] Bažant, Z.; Tabbara, M.; Kazemi, M.; et al.: Random Particle Model for Fracture of Aggregate or Fiber Composites. *Journal of the Engineering Mechanics Division ASCE*, volume 116, nr. 8, 1990: pages 1686–1705, ISSN 0733-9399.

[5] Bažant, Z. P.; Pang, S.-D.: Activation energy based extreme value statistics and size effect in brittle and quasibrittle fracture. *Journal of the Mechanics and Physics of Solids*, volume 55, nr. 1, 2007: pages 91–131, ISSN 0022-5096.

[6] Bažant, Z. P.; Planas, J.: *Fracture and Size Effect in Concrete and Other Quasibrittle Materials*. CRC Press, Boca Raton and London, 1998.

[7] Bažant, Z. P.; Jirásek, M.: Nonlocal Integral Formulations of Plasticity and Damage: Survey of Progress. *Journal of Engineering Mechanics*, volume 128, nr. 11, 2002: pages 1119–1149.

[8] Bažant, Z. P.; Oh, B. H.: Crack band theory for fracture of concrete. *Matériaux et Construction*, volume 16, nr. 3, 1983: pages 155–177, ISSN 1871-6873.

[9] Bažant, Z. P.; Vořechovský, M.; Novák, D.: Asymptotic Prediction of Energetic-Statistical Size Effect from Deterministic Finite-Element Solutions. *Journal of Engineering Mechanics (ASCE)*, volume 133, nr. 2, 2007: pages 153–162.

[10] Bolander, J.; Saito, S.: Fracture Analyses Using Spring Networks with Random Geometry. *Engineering Fracture Mechanics*, volume 61, nr. 5–6, 1998: pages 569–591, ISSN 0013-7944.

[11] Burt, N. J.; Dougill, J. W.: Progressive Failure in a Model Heterogeneous Medium. *Journal of Engineering Mechanics Division ASCE*, volume 103, nr. 3, 1977: pages 365–376, ISSN 0044-7951.

[12] Cusatis, G.; Bažant, Z. P.; Cedolin, L.: Confinement-Shear Lattice Model for Concrete Damage in Tension and Compression: I. Theory. *Journal of the Engineering Mechanics Division ASCE*, volume 129, nr. 12, 2003: pages 1439–1448, ISSN 0733-9399.

[13] Cusatis, G.; Bažant, Z. P.; Cedolin, L.: Confinement-shear lattice CSL model for fracture propagation in concrete. *Computer Methods in Applied Mechanics and Engineering*, volume 195, nr. 52, 2006: pages 7154–7171, ISSN 0045-7825.

[14] Cusatis, G.; Cedolin, L.: Two-scale study of concrete fracturing behavior. *Engineering Fracture Mechanics*, volume 74, nr. 1–2, 2007: pages 3–17, ISSN 0013-7944.

[15] Cusatis, G.; Pelessone, D.; Mencarelli, A.: Lattice Discrete Particle Model (LDPM) for failure behavior of concrete. I: Theory. *Cement and Concrete Composites*, volume 33, nr. 9, 2011: pages 881–890, ISSN 0958-9465.

[16] Delaunay, B.: Sur la sphère vide. *Bulletin de l'Académie des Sciences de l'URSS. Classe des sciences mathématiques et naturelles*, volume 6, 1934: pages 793–800.

[17] Eliáš, J.; Kaděrová, J.; Vořechovský, M.: Interplay of probabilistic and deterministic internal lengths in simulations of concrete fracture. In *9th International Conference on Fracture Mechanics of Concrete and Concrete Structures FraMCoS-9*, Berkley, USA, 2016, pages 1–10, abstract.

[18] Eliáš, J.: Adaptive technique for discrete models of fracture. *International Journal of Solids and Structures*, volume 100-101, nr. Supplement C, 2016: pages 376 – 387, ISSN 0020-7683.

[19] Eliáš, J.: Boundary Layer Effect on Behavior of Discrete Models. *Materials*, volume 10, 2017: pg. 157, ISSN 1996-1944.

[20] Eliáš, J.; Bažant, Z. P.: Fracturing in concrete via lattice-particle model. In *2nd international conference on particle-based methods - fundamentals and applications, proc. of PARTICLES 2011*, edited by E. Onate; D. Owen, Barcelona, Spain, 2011, ISBN 978-84-89925-69-4, pg. 12.

[21] Eliáš, J.; Vořechovský, M.; Skoček, J.; et al.: Stochastic discrete meso-scale simulations of concrete fracture: Comparison to experimental data. *Engineering Fracture Mechanics*, volume 135, 2015: pages 1–16, ISSN 0013-7944.

[22] Eliáš, J.; Vořechovský, M.; Bažant, Z. P.: Stochastic lattice simulations of flexural failure in concrete beams. In *8th International Conference on Fracture Mechanics of Concrete and Concrete Structures - FraMCoS-8*, edited by G. R. e. a. Van Mier, Toledo, Spain, 2013, pg. 12.

[23] Eliáš, J.; Vořechovský, M.; Le, J.-L.: Lattice Modeling of Concrete Fracture Including Material Spatial Randomness. *Engineering Mechanics*, volume 5, 2013: pages 413–426, ISSN 1802-1484.

[24] Frantík, P.; Veselý, V.; Keršner, Z.: Parallelization of lattice modelling for estimation of fracture process zone extent in cementitious composites. *Advances in Engineering Software*, volume 60-61, nr. Supplement C, 2013: pages 48 – 57, ISSN 0965-9978.

[25] Grassl, P.; Bažant, Z. P.: Random lattice-particle simulation of statistical size effect in quasi-brittle structures failing at crack initiation. *Journal of the Engineering Mechanics Division ASCE*, volume 135, 2009: pages 85–92, ISSN 0733-9399.

[26] Grassl, P.; Grégoire, D.; Solano, L. R.; et al.: Meso-scale modelling of the size effect on the fracture process zone of concrete. *International Journal of Solids and Structures*, volume 49, nr. 43, 2013: pages 1818–1827, ISSN 0020-7683.

[27] Grégoire, D.; Rojas-Solano, L.; Pijaudier-Cabot, G.: Failure and size effect for notched and unnotched concrete beams. *International Journal for Numerical and Analytical Methods in Geomechanics*, volume 37, nr. 10, 2013: pages 1434–1452, ISSN 1096-9853.

[28] Grégoire, D.; Verdon, L.; Lefort, V.; et al.: Mesoscale analysis of failure in quasi-brittle materials: comparison between lattice model and acoustic emission data. *International Journal for Numerical and Analytical Methods in Geomechanics*, volume 39, nr. 15, 2015: pages 1639–1664, ISSN 1096-9853, nag.2363.

[29] Herrmann, H.; Hansen, A.; Roux, S.: Fracture of disordered, elastic lattices in two dimensions. *Physical Review B*, volume 39, nr. 1, 1989: pages 637–648, ISSN 1098-0121.

[30] Hillerborg, A.; Modéer, M.; Petersson, P.-E.: Analysis of crack formation and crack growth in concrete by means of fracture mechanics and finite elements. *Cement and Concrete Research*, volume 6, nr. 6, 1976: pages 773 – 781, ISSN 0008-8846.

[31] Hoover, C. G.; Bažant, Z. P.: Comprehensive concrete fracture tests: Size effects of Types 1 & 2, crack length effect and postpeak. *Engineering Fracture Mechanics*, volume 110, 2013: pages 281 – 289, ISSN 0013-7944.

[32] Hoover, C. G.; Bažant, Z. P.; Vorel, J.; et al.: Comprehensive concrete fracture tests: Description and results. *Engineering Fracture Mechanics*, volume 114, 2013: pages 92 – 103, ISSN 0013-7944.

[33] Ince, R.; Arslan, A.; Karihaloo, B.: Lattice modelling of size effect in concrete strength. *Engineering Fracture Mechanics*, volume 70, nr. 16, 2003: pages 2307–2320, ISSN 0013-7944, size-scale effects.

[34] Irwin, G. R.: *Elasticity and Plasticity / Elastizität und Plastizität*, chapter Fracture. Berlin, Heidelberg: Springer Berlin Heidelberg, 1958, ISBN 978-3-642-45887-3, pages 551–590.

[35] Iturrioz, I.; Lacidogna, G.; Carpinteri, A.: Experimental analysis and truss-like discrete element model simulation of concrete specimens under uniaxial compression. *Engineering Fracture Mechanics*, volume 110, 2013: pages 81 – 98, ISSN 0013-7944.

[36] Jirásek, M.; Bažant, Z.: Macroscopic fracture characteristics of random particle systems. *International Journal of Fracture*, volume 69, nr. 3, 1995: pages 201–228, ISSN 0376-9429.

[37] Jirásek, M.; Bažant, Z. P.: Particle Model for Quasibrittle Fracture and Application to Sea Ice. *Journal of Engineering Mechanics*, volume 121, nr. 9, 1995: pages 1016–1025.

[38] Jivkov, A. P.; Engelberg, D. L.; Stein, R.; et al.: Pore space and brittle damage evolution in concrete. *Engineering Fracture Mechanics*, volume 110, nr. 0, 2013: pages 378–395, ISSN 0013-7944.

[39] Kaděrová, J.; Eliáš, J.: Simulations of bending experiments of concrete beams by stochastic discrete model. In *Key Engineering Materials*, volume 627, edited by F. A. M. Alfaiate J., Trans Tech Publications, 2014, ISBN 978-3-03835-235-8, ISSN 10139826, pages 457–460.

[40] Kaděrová, J.; Eliáš, J.; Vořechovský, M.: Influence of Autocorrelation Length in Random Lattice–Particle Model. In *International Conference on Computational Modeling of Fracture and Failure (CFRAC 2015)*, Sciencesconf.org, 2015, pages 159–160, abstract.

[41] Kaděrová, J.; Eliáš, J.; Vořechovský, M.: The Influence of Correlation Length on the Strength of Stochastic Discrete Models. In *Proceedings of the Fifteenth International Conference on Civil, Structural and Environmental Engineering Computing*, number 108 in Civil-Comp Proceedings, Civil–Comp Press, 2015, ISBN 978-1-905088-63-8, ISSN 1759-3433, pages 1–13.

[42] Kang, J.; Kim, K.; Lim, Y. M.; et al.: Modeling of fiber-reinforced cement composites: Discrete representation of fiber pullout. *International Journal of Solids and Structures*, volume 51, nr. 10, 2014: pages 1970 – 1979, ISSN 0020-7683.

[43] Kunieda, M.; Ogura, H.; Ueda, N.; et al.: Tensile fracture process of Strain Hardening Cementitious Composites by means of three-dimensional meso-scale analysis. *Cement and Concrete Composites*, volume 33, nr. 9, 2011: pages 956 – 965, ISSN 0958-9465.

[44] Le, J.-L.; Bažant, Z. P.: Unified nano-mechanics based probabilistic theory of quasibrittle and brittle structures: II. Fatigue crack growth, lifetime and scaling. *Journal of the Mechanics and Physics of Solids*, volume 59, 2011: pages 1322–1337, ISSN 0022-5096.

[45] Le, J.-L.; Bažant, Z. P.; Bazant, M. Z.: Unified nano-mechanics based probabilistic theory of quasibrittle and brittle structures: I. Strength, static crack growth, lifetime and scaling. *Journal of the Mechanics and Physics of Solids*, volume 59, nr. 7, 2011: pages 1291–1321, ISSN 0022-5096.

[46] Li, C.; Der Kiureghian, A.: Optimal Discretization of Random Fields. *Journal of Engineering Mechanics Division ASCE*, volume 119, nr. 6, 1993: pages 1136–1154, ISSN 0733-9399.

[47] Li, H.; Lü, Z.; Yuan, X.: Nataf transformation based point estimate method. *Chinese Science Bulletin*, volume 53, nr. 17, 2008: pg. 2586, ISSN 1861-9541.

[48] Man, H.-K.; van Mier, J.: Influence of particle density on 3D size effects in the fracture of (numerical) concrete. *Mechanics of Materials*, volume 40, nr. 6, 2008: pages 470–486, ISSN 0167-6636.

[49] Mungule, M.; Raghuprasad, B.; Muralidhara, S.: Fracture studies on 3D geometrically similar beams. *Engineering Fracture Mechanics*, volume 98, 2013: pages 407–422, ISSN 0013-7944.

[50] Pedregosa, F.; Varoquaux, G.; Gramfort, A.; et al.: Scikit-learn: Machine Learning in Python. *Journal of Machine Learning Research*, volume 12, 2011: pages 2825–2830.

[51] Pedregosa, F.; Varoquaux, G.; Gramfort, A.; et al.: Scikit-learn: Machine Learning in Python. *Journal of Machine Learning Research*, volume 12, 2011: pages 2825–2830.

[52] Schlangen, E.; Garboczi, E.: Fracture simulations of concrete using lattice models: Computational aspects. *Engineering Fracture Mechanics*, volume 57, nr. 2-3, 1997: pages 319–332, ISSN 0013-7944.

[53] Schölkopf, B.; Platt, J. C.; Shawe-Taylor, J. C.; et al.: Estimating the Support of a High-Dimensional Distribution. *Neural Computation*, volume 13, nr. 7, July 2001: pages 1443–1471, ISSN 0899-7667.

[54] Syroka-Korol, E.; Tejchman, J.; Mróz, Z.: FE investigations of the effect of fluctuating local tensile strength on coupled energetic–statistical size effect in concrete beams. *Engineering Structures*, volume 103, 2015: pages 239 – 259, ISSN 0141-0296.

[55] van Mier, J.: *Fracture Processes of Concrete*. CRC Press, 1997, ISBN 0-8493-9123-7.

[56] van Mier, J.: *Concrete Fracture: A Multiscale Approach*. CRC Press, October 2013, ISBN 9781466554702.

[57] Vořechovský, M.: Interplay of size effects in concrete specimens under tension studied via computational stochastic fracture mechanics. *International Journal of Solids and Structures*, volume 44, nr. 9, 2007: pages 2715–2731, ISSN 0020-7683.

[58] Vořechovský, M.: Simulation of simply cross correlated random fields by series expansion methods. *Structural safety (Elsevier)*, volume 30, nr. 4, 2008: pages 337–363, ISSN 0167-4730.

[59] Vořechovský, M.; Novák, D.: Correlation control in small-sample Monte Carlo type simulations I: A simulated annealing approach. *Probabilistic Engineering Mechanics*, volume 24, nr. 3, 2009: pages 452 – 462, ISSN 0266-8920.

[60] Vořechovský, M.; Sadílek, V.: Computational modeling of size effects in concrete specimens under uniaxial tension. *International Journal of Fracture*, volume 154, nr. 1-2, 2008: pages 27–49, ISSN 0376-9429.

[61] Šavija, B.; Pacheco, J.; Schlangen, E.: Lattice modeling of chloride diffusion in sound and cracked concrete. *Cement and Concrete Composites*, volume 42, 2013: pages 30 – 40, ISSN 0958-9465.

[62] Zubelewicz, A.; Bažant, Z. P.: Interface Element Modeling of Fracture in Aggregate Composites. *Journal of Engineering Mechanics*, volume 113, nr. 11, 1987: pages 1619–1630.

LIST OF SYMBOLS, PHYSICAL CONSTANTS AND ABBREVIATIONS

CDF	cumulative density function
CoV	coefficient of variation
CMOD	crack-mouth opening displacement
DOF	degree of freedom
EOLE	expansion optimal linear estimation
FEM	finite element method
FPZ	fracture process zone
LDPM	lattice discrete particle model
LEFM	linear elastic fracture mechanics
LHS	Latin Hypercube Sampling
PDF	probability density function
std	standard deviation
$\boldsymbol{A}$	matrix of rigid body motion
A	area of contact facet, cross-section area
b	thickness
$\boldsymbol{C}$	covariance matrix
$\boldsymbol{c}$	centroid of contact facet
D	damage parameter; depth
$D[...]$	variance (dispersion)
E	elasticity modulus of contact
E_{a}	elastic modulus of grains
E_{c}	elastic modulus of matrix
$E^{(p)}$	fracture energy released in all beam till the step p
$E_h^{(p)}$	fracture energy released in an element h till the step p
$F, \boldsymbol{F}$	force, force vector
$F_X(x)$	cumulative density function of random variable X at point x
$F_{\max}$	maximal load
F_o	error function
f_{c}	compressive strength
f_{eq}	equivalent strength
f_{s}	shear strength
f_{t}	tensile strength
G_{s}	fracture energy in shear
G_{t}	fracture energy in tension
$\boldsymbol{H}^c(\boldsymbol{x})$	c-th realization of a random field at spatial coordinate $\boldsymbol{x}$
$\hat{\boldsymbol{H}}$	Gaussian random field

H_{FPZ}	width of the fracture process zone
h_{gr}	grafting point: point of Weibull-Gauss juncture
K	initial slope of elastic boundary; number of considered eigenmodes
K_{c}	parameter of initial slope of compressive hardening
K_{s}	parameter of initial slope in shear
K_{t}	parameter of initial slope in tension
L	length
l_{c}	correlation length
l_{char}	characteristic length
$\boldsymbol{M}$	bending moment
m	Weibull modulus (shape parameter)
$\boldsymbol{n}, \boldsymbol{m}, \boldsymbol{l}$	directional vectors (normal and two tangential)
n_{c}	parameter of compressive hardening
n_{sim}	number of simulations
p_{gr}	grafting probability
R_b	sum of relative fracture energies of one bin b over all simulations
$\bar{R}_b$	normalized sum of relative fracture energies of one bin b over all simulations
R_i	radius of generated sphere i
r_f	scaling parameter of probability distribution
S	bending span
s	scale parameter of Weibull distribution
$\boldsymbol{u}$	transitional degrees of freedom
W	cross-sectional modulus
$\boldsymbol{x}$	vector of coordinates
α	parameter determining the macroscopic Poisson ratio
β	parameter of compressive elastic envelope
$\boldsymbol{\Delta}_{ij}$	displacement discontinuity
$\Delta E^{(p)}$	fracture energy released in all beam in one step p
$\Delta \bar{E}^{(p)}$	relative fracture energy released in all beam in one step p
$\Delta \bar{E}_b^{(p)}$	relative fracture energy released in one bin b in one step p
$\Delta E_h^{(p)}$	fracture energy released in an element h in one step p
$\Delta \bar{E}_h^{(p)}$	relative fracture energy released in an element h in one step p
δ	inverse coefficient of variation
ε	strain
$\varepsilon_{\mathrm{eq}}$	equivalent strain
$\boldsymbol{\theta}$	rotational degrees of freedom
λ	confining strain; eigenvalue
λ_0	characteristic strain parameter (sensitivity of confining strain)

μ	slope of el. envelope hyperbola asymptote; mean value
ν	Poisson ratio
$\boldsymbol{\xi}$	standard Gaussian variables
ρ_{ij}	correlation coefficient between points i and j
σ	stress, standard deviation
σ_{eq}	equivalent stress
$\bar{\sigma}_N$	nominal strength
$\boldsymbol{\Phi}$	CDF of standard (Gaussian) distribution
χ	function of the loading history
$\boldsymbol{\psi}$	eigenvector
ω	straining direction
ω_0	straining direction of junction of two functions of equivalent strength f_{eq}